

ABSTRACT

Title of Dissertation: AN EXPERIMENTAL INVESTIGATION ON
THE AIR ENTRAINMENT BY PLUNGING JETS

Ramón Gómez Ledesma, Doctor of Philosophy, 2004

Dissertation directed by: Associate Professor Kenneth T. Kiger, Chairman/Advisor
Professor James H. Duncan , co-Advisor
Department of Mechanical Engineering

The air entrained by the impact of the jet ejected by a plunging breaker was studied both experimentally and theoretically by using laboratory plunging jets. One determining characteristic of these jets is the horizontal relative motion between the impacting jet and the free surface. As a first approximation to the problem and in order to investigate the influence of the horizontal translation on the air entrainment, a vertical, circular, laminar jet that plunges continuously onto a receiving water pool was utilized. It was found that the air entrainment was produced for the cases where the Fr number based on the jet diameter and translation speed was larger than 1.4. For fixed values of V_t/V_j , where V_t is the jet horizontal translation velocity and V_j , the jet impact velocity, the entrainment was observed to occur in different regimes attending to the value of Fr . For values of Fr slightly higher than 1.4, the entrainment was produced in the form of

small bubbles ('small bubble entrainment regime'). For the largest values of Fr , the jet was observed to produce larger bubbles in a continuous fashion ('continuous entrainment regime') while for moderate values of Fr , the entrainment was produced in the form of intermittent bursts of bubbles ('intermittent entrainment regime'). The boundaries between the mentioned regimes were plotted on a Fr vs V_t/V_j diagram showing that they converge for increasing values of V_t/V_j . The underwater flow produced by this jet was further investigated by marking the jet water with small particles and recorded with a high-speed camera. These experiments reveal the existence of vortical structures resulted from the shear between the incoming jet water and the pool water that play an important role in the air entrainment process.

As a second degree of approximation to the wave problem, a planar, translating water jet that suddenly impacts on the pool free surface was investigated. The inertia of the impacting jet was observed to create two open air craters at either side of the impact site. At the early stages of the crater formation, the open craters are driven into the pool water and remain attached to the underwater jet. For the parameter space studied herein, the underwater jet tip translates with a steady velocity that can be predicted with quasi-steady potential flow theory. It was found that the dynamics of the different regions of the crater walls are dominated by either inertial or gravitational effects depending on the local radius of curvature (R_o), the local inclination of the crater wall (β_o) and the velocity of the particles parallel to the wall given in a reference frame fixed with the jet tip (V_o). Inertial effects are dominant in the regions near the jet tip (large values of $Fr_o^2/\cos\beta_o$, where Fr_o is the Froude number based on R_o and V_o). In these regions, where gravity plays a secondary role, the craters remain

unchanged with time and their shapes can be calculated with quasi-steady potential flow theory. Far from the jet tip, the non-dimensional number $Fr_o^2 / \cos \beta_o$ is moderate or small in magnitude and the hydrostatic pressure forces the crater walls to move towards the jet with a deformation velocity that increases with the square root of depth. As time progresses, the crater walls touch the jet at a given depth (pinch-off depth, d_{po}) and at a given time (pinch-off time, t_{po}). The evolving shapes of the two underwater craters were observed to be largely affected by the horizontal translation of the jet, leading to values of (d_{po}) and (t_{po}) which decreased with the jet translation velocity. Simple scaling arguments based on an energy balance applied to the particles situated at the crater walls were used to estimate the shapes of the underwater crater contours and ultimately, d_{po} and t_{po} . Lastly, for small jet translation velocities, the underwater craters were observed to detach from the open crater soon after the pinch-off event leading to the formation of a large entrained air bubble. For one of the jet experimental conditions, the volume of air entrapped by this bubble was not observed to vary substantially with the translation speed.

AN EXPERIMENTAL INVESTIGATION ON
THE AIR ENTRAINMENT BY PLUNGING JETS

by

Ramón Gómez Ledesma

Dissertation submitted to the Faculty of the Graduate School of the
University of Maryland at College Park in partial fulfillment
of the requirements for the degree of
Doctor of Philosophy
2004

Advisory Committee:

Associate Professor Kenneth T. Kiger, Chairman/Advisor
Professor James H. Duncan , co-Advisor
Assistant Professor Elias Balaras
Professor Richard V. Calabrese
Professor James Wallace

© Copyright by
Ramón Gómez Ledesma
2004

DEDICATION

To the family Pereira.

ACKNOWLEDGEMENTS

I would like to express my sincere gratitude to the faculty and staff of the University of Maryland at College Park for hosting me during my Ph.D. education, and in particular to my advisors Ken Kiger and Jim Duncan for having given me the opportunity to come to Maryland to do my Ph.D. and for having patiently guided me through it. My deepest gratitude for devoting their time to my education and for everything I learnt from them. Thanks also to Dr. Kiger and his wife Sarah for hosting me in their house during the first two weeks of my stay at Maryland. I would also like to emphasize my gratitude to my other professors at Maryland and the other members of my Ph.D. committee: Elias Balaras, James Wallace and Richard Calabrese, as well as to Jose Luis Montañes for encouraging me to come to Maryland for my doctoral studies. The financial support by the National Science Foundation is also greatly acknowledged.

I would like to express my gratitude also to the people at the Physics Machine Shop, particularly to Dick Terlisner for his time and his wise advise during the design and construction of my experimental facility, and to Bob Anders for his guidance in the machine shop at the Engineering Building. To my labmates, Xinan Liu, Chunhui Pan, Paolo Ruffino, Mostafa Shakeri, Angel Rivero, Timo Steinback, Matt and Phil Knowles, thanks for your help and your friendship. Special thanks to my friend Dylan Chirichella who got me started in the lab and provided us with his invaluable help during my first year as a graduate

student. Thanks also to all my volunteers helping in the weekends with the steel frame of my experimental facility: Igor Alonso Portillo, Michelle Shannon, Isabel, Gustavo and Frederico Pereira. To my neighbours, Maria Ribera and Alice Lapuerta, thanks for your company and your kindness and to my family for your wise advise and your support in my idea of coming to Maryland. My deepest gratitude, as well, to Lucia Alcantara that made every effort to provide me with a nice social environment at Maryland. Thanks to her and to her family for their love. I would like also to mention here my roommates: Cesar Lapuerta, thanks for your friendship and your good attitude about everything, and Mohammed Reza, thanks for all those unforgettable evenings around our guitars. Also, thanks to all the people that made it all the way from Spain to come visit to the US: my sister Isabel and my friends Rosa, Ivan, Ruben, Rafa, Paco, Chimo y Juan.

Finally, I would like to express my deepest gratitude to Isabel, Gustavo, Frederico and Sandra Pereira. They became more than a family to me and without their support, this work would have not been possible.

TABLE OF CONTENTS

List of Tables	viii
List of Figures	ix
1 Motivation	1
1.1 The Greenhouse Effect	1
1.2 Unbroken Surface Ocean-Atmosphere Gas Exchange Models . . .	4
1.3 The Effect of Bubbles on the Ocean-Atmosphere Gas Exchange Models	6
1.4 Plunging Jets to Study Air Entrainment by Breaking Waves . . .	8
2 Literature Review and Overview	10
2.1 Continuously Running Jets	10
2.2 Impacting Jets	15
2.3 Lack of Results on Translating Jets	20
2.4 Overview of the Present Work	20
3 Steady Translating Circular Jet	22
3.1 Experimental Set-Up	22
3.1.1 Water Tank and Jet Nozzle	22

3.1.2	High-Speed Imaging	25
3.1.3	Still Pictures	26
3.1.4	Characterization of the Jet	26
3.2	General Description of the Flow and Measurements of the Bound- aries Between Entrainment Regimes	27
3.3	Dimensional Analysis - Fr Number vs. Velocity Ratio Diagram . .	36
3.4	Entrainment Mechanism	39
3.5	Conclusions for the Circular Jet	49
4	Facility Design and Construction for the Impacting Planar Jet	50
4.1	General Description and Dimensioning	50
4.2	Water Tank Steel Frame and Glass	52
4.3	Carriage and Bearing System	55
4.4	Water Re-circulation and Skimming Systems	61
4.5	Jet Nozzle Design and Construction	63
4.5.1	General Description and Dimensioning	63
4.5.2	Turbulence Reduction Systems	65
4.5.3	Nozzle Contraction Design	67
4.6	Jet Cutter and Free Surface Disturbances	75
4.7	Removal of Jet End Effects	78
5	Visualization Experiments for the Impacting Planar Jet	83
5.1	Experimental Set-Up	83
5.1.1	High Speed Imaging	83
5.1.2	Measurements of the Jet Impact Conditions and Nomen- clature	84

5.2	General Description of the Flow	89
5.3	Measurements of the Pinch-Off Depths and Pinch-Off Times	100
5.4	Dimensional Analysis	106
6	The Flow Field Near the Tip of the Underwater Planar Jet - PIV Experiments	108
6.1	Experimental Set-Up - PIV	109
6.2	Velocity Field Near the Jet Tip	114
7	Theoretical Model and Discussion	124
7.1	Underwater Jet Tip Velocity	125
7.2	Solution Without Gravity - Shape of the Free Streamlines	139
7.3	The Roles of Gravity and Inertia - Velocity of Collapse	145
7.4	Temporal Evolution of the Underwater Craters - Pinch-off Time and Depth	151
7.5	Underwater Crater Contours	166
7.6	Detachment of the Crater at Small Translation Velocities	176
8	Conclusions for the Impacting Planar Jet	182
8.1	Conclusions on the Physics of the Crater Formation of the Impacting Planar Jet	182
8.2	The Present Study in Relation with the Aeration of the Oceans as a Result of the Simulated Impact of Jets Ejected by Plunging Breakers	184
	Bibliography	189

LIST OF TABLES

3.1	Experimental conditions and entrainment boundaries.	34
3.2	Continuation of Experimental conditions and entrainment bound- aries.	35
5.1	Planar jet impact experimental conditions	85
5.2	T_b values measured from the above-water movies	88
5.3	Measurements of the pinch-off times (mean)	101
5.4	Measurements of the pinch-off times (standard deviation)	101
5.5	Measurements of the pinch-off depths (mean)	103
5.6	Measurements of the pinch-off depths (standard deviation)	103
5.7	t_c values for CI computation for a 95% probability level	104
5.8	Measurements of the pinch-off depths (CI for 95%)	105
5.9	Measurements of the pinch-off times (CI for 95%)	105
6.1	Measurements of the underwater jet tip velocity for jet condition III115	
6.2	Measurements of the underwater jet penetration angle with the vertical for jet condition III	115
7.1	Accommodation times (ms)	174

LIST OF FIGURES

1.1	Plunging Jet in a Plunging Breaker	9
2.1	Schematic of the above and under water geometry of a water mass falling on a water pool.	16
3.1	Schematic of chamber utilized for the circular jet experiment . . .	23
3.2	Lateral view of the water tank used for the circular jet experiment	24
3.3	Side view of the water tank	25
3.4	Above-water view of the jet impact site. $V_j = 303 \text{ cm/s}$, $D_j = 0.6$ cm , $V_t = 0.0 \text{ cm/s}$	28
3.5	Above-water view of the jet impact site for no air entrainment conditions. $V_j = 303 \text{ cm/s}$, $D_j = 0.6 \text{ cm}$, $V_t = 31.8 \text{ cm/s}$	30
3.6	Below-water view of the jet impact site for no air entrainment conditions. $V_j = 303 \text{ cm/s}$, $D_j = 0.6 \text{ cm}$, $V_t = 31.8 \text{ cm/s}$	30
3.7	Above-water view of the jet impact site for incipient entrainment conditions. $V_j = 303 \text{ cm/s}$, $D_j = 0.6 \text{ cm}$, $V_t = 38.51 \text{ cm/s}$	31
3.8	Below-water view of the jet impact site for incipient entrainment conditions. $V_j = 303 \text{ cm/s}$, $D_j = 0.6 \text{ cm}$, $V_t = 38.51 \text{ cm/s}$	31
3.9	Above-water view of the jet impact site for intermittent entrain- ment conditions. $V_j = 303 \text{ cm/s}$, $D_j = 0.6 \text{ cm}$, $V_t = 44.5 \text{ cm/s}$. . .	32

3.10	Below-water view of the jet impact site for intermittent entrainment conditions. $V_j = 303 \text{ cm/s}$, $D_j = 0.6 \text{ cm}$, $V_t = 44.5 \text{ cm/s}$. . .	32
3.11	Froude number vs velocity ratio the different entrainment regimes	37
3.12	Nomenclature for the entraining jet flow shown in the reference frame moving with the jet. The schematic on the top is a schematic of the underwater picture on the bottom.	40
3.13	Temporal evolution of the depth of the vortices, undulations on the leading edge of the cavity, and the cusp of the cavity for an incipient entrainment case. $D_j = 0.67 \text{ cm}$, $V_j = 172 \text{ cm/s}$. White triangles are vortex centers, circles are undulations on cavity leading edge and black triangles are cusp's position.	41
3.14	Temporal evolution of the depth of the vortices, a single entrained small bubble, and the cusp of the cavity for an incipient entrainment case. $D_j = 0.67 \text{ cm}$, $V_j = 172 \text{ cm/s}$. White triangles are vortex centers, circles represent the entrained bubble and black triangles are cusp's position.	42
3.15	Temporal evolution of the depth of the vortices, and the cusp of the cavity for an intermittent entrainment case. $D_j = 0.57 \text{ cm}$, $V_j = 237 \text{ cm/s}$. White triangles are vortex centers and black triangles represent the cusp.	43
3.16	Sequence of images of a bubble forming inside a jet vortex. The jet flow is seeded with small particles. The image sequence was taken with a high-speed digital camera. Time between frames = 1.2 ms . $D_j = 0.57 \text{ cm}$, $V_j = 237 \text{ cm/s}$ and $V_t = 38.1 \text{ cm/s}$	45
3.17	Sequence of images continuation of Figure 3.16	46

3.18	Below-water view of a surface piercing solid rod. The upper part of the image of the rod is a reflection from the water surface. The rod diameter and the towing speed are the same as the jet impact diameter and velocity in Figures 3.9 and 3.10, $D_j = 0.6$ cm, $V_j = 44.5$ cm/s	48
4.1	Tank structure during the alignment process.	52
4.2	Ansys predicted deformations of the steel structure induced by the hydrostatic water pressure	54
4.3	Aluminium mountings for the carriage rails	55
4.4	Aluminium L-beams mountings for the carriage rails during the construction process	56
4.5	Carriage ball bearing systems	57
4.6	Picture of the aluminium drums, shaft, universal joint and steel towing cable	59
4.7	Picture of the new instrument carriage. In the image are visible several of the described elements such as the supporting trays for the camera and computer on a side of the tank, the structure that holds the jet nozzle, the long aluminum structures that hold the carriage rails, the bearing systems and the compressed-air reservoir for the jet cutter device (described in later sections).	60
4.8	The figure shows a schematic of the piping system looking at the tank bottom from the top	61
4.9	Picture of the three water skimmers at one end of the new facility. The skimmers remove the contaminants from the water free surface and send them to a filter	62

4.10	The jet is created from tank water and is fed by a centrifugal pump	63
4.11	Cut of the planar jet nozzle. The nozzle is 18 inch wide (into the paper)	65
4.12	A planar jet nozzle with half a contraction (top) reaches lower jet free-fall distances that a jet nozzle with a symmetric contraction (bottom)	67
4.13	Streamlines of a 10 to 1 contraction in potential flow	68
4.14	Pressure distribution on the streamlines of a 10 to 1 contraction in potential flow	70
4.15	Pressure gradient distribution on the streamlines of a 10 to 1 contraction in potential flow	71
4.16	Selected streamline due to its favorable pressure gradient	72
4.17	Curvature distribution on the selected streamline	73
4.18	Final contraction design	74
4.19	Jet cutter system. Plate deflecting the jet	76
4.20	Jet cutter system right after the jet cut	76
4.21	Sections of the water jet as it falls	78
4.22	Front view of the jet ends cutter device	79
4.23	The jet edge deflector device removes the ends of the jet and provides two transparent vertical boundaries for the two-dimensional plunging jet problem	80
4.24	Lateral view of the jet edge deflector device. The jet has already plunged on the tank water free surface	81
4.25	Perspective of the jet deflector in its initial position before the jet has been cut	82

4.26	Perspective of the jet edge deflector and the jet cutter in its final position after the jet has been cut	82
5.1	Jet nomenclature	85
5.2	Buldge at jet leading edge	88
5.3	Jet condition VI, $V_t = 0.15 \text{ m/s}$, $t = 40 \text{ ms}$ after the jet impact. Note that the black strip at the top is the opaque steel cutting blade.	90
5.4	Jet condition VI, $V_t = 0.15 \text{ m/s}$, $t = 80 \text{ ms}$ after the jet impact .	91
5.5	Jet condition VI, $V_t = 0.15 \text{ m/s}$, $t = 121 \text{ ms}$ after the jet impact .	92
5.6	Jet condition VI, $V_t = 0.15 \text{ m/s}$, $t = 160 \text{ ms}$ after the jet impact .	93
5.7	Jet condition V, $V_t = 0.00 \text{ m/s}$, $t/t_{po} = 1/3$ ($t = 39 \text{ ms}$)	94
5.8	Jet condition V, $t/t_{po} = 1/3$: $t = 35 \text{ ms}$, $V_t = 0.15 \text{ m/s}$ (top left); $t = 32 \text{ ms}$, $V_t = 0.30 \text{ m/s}$, (top right); $t = 24 \text{ ms}$, $V_t = 0.45 \text{ m/s}$ (bottom left); $t = 19 \text{ ms}$, $V_t = 0.60 \text{ m/s}$ (bottom right)	95
5.9	Jet condition V, $V_t = 0.00 \text{ m/s}$, $t/t_{po} = 2/3$ ($t = 77 \text{ ms}$)	96
5.10	Jet condition V, $t/t_{po} = 2/3$. $V_t = 0.15 \text{ m/s}$, ($t = 71 \text{ ms}$) (top left); $V_t = 0.30 \text{ m/s}$, ($t = 63 \text{ ms}$) (top right); $V_t = 0.45 \text{ m/s}$, ($t = 47 \text{ ms}$) (bottom left); $V_t = 0.60 \text{ m/s}$, ($t = 38 \text{ ms}$) (bottom right)	97
5.11	Jet condition V, $V_t = 0.00 \text{ m/s}$, $t/t_{po} = 1$ ($t = 116 \text{ ms}$)	98
5.12	Jet condition V, $t/t_{po} = 1$. $V_t = 0.15 \text{ m/s}$, ($t = 106 \text{ ms}$) (top left); $V_t = 0.30 \text{ m/s}$, ($t = 95 \text{ ms}$) (top right); $V_t = 0.45 \text{ m/s}$, ($t = 71 \text{ ms}$) (bottom left); $V_t = 0.60 \text{ m/s}$, ($t = 57 \text{ ms}$) (bottom right) . .	99
6.1	Laser beam path and lenses	110
6.2	Lateral view of the PIV setup	110

6.3	Schematic of the PIV set-up and camera-laser synchronization. . .	111
6.4	PIV picture for conditon III. $V_t = 0.3 \text{ m/s}$. The picture shows the PIV particles and the two underwater air craters. The camera is translating with the jet from right to left. The rectangle ($17 \times 17 \text{ mm}$) is the region where the PIV processing was applied.	112
6.5	PIV vector field for jet condition III and $V_t = 0.0 \text{ m/s}$ in a reference frame moving with the jet carriage. Actual image size $17 \times 17 \text{ mm}$	116
6.6	PIV vector field for jet condition III and $V_t = 0.0 \text{ m/s}$ in a reference frame moving with the jet tip. Actual image size $17 \times 17 \text{ mm}$. .	117
6.7	PIV streamlines for jet condition III and $V_t = 0.0 \text{ m/s}$ in a reference frame moving with the jet tip. Actual image size $17 \times 17 \text{ mm}$	118
6.8	PIV vector field for jet condition III and $V_t = 0.15 \text{ m/s}$ in a reference frame moving with the jet carriage (top), moving with the jet tip (middle) and PIV streamlines (bottom). Actual image size $17 \times 17 \text{ mm}$	120
6.9	PIV vector field for jet condition III and $V_t = 0.30 \text{ m/s}$ in a reference frame moving with the jet carriage (top), moving with the jet tip (middle) and PIV streamlines (bottom). Actual image size $17 \times 17 \text{ mm}$	121
6.10	PIV vector field for jet condition III and $V_t = 0.45 \text{ m/s}$ in a reference frame moving with the jet carriage (top), moving with the jet tip (middle) and PIV streamlines (bottom). Actual image size $17 \times 17 \text{ mm}$	122

6.11	PIV vector field for jet condition III and $V_t = 0.60 \text{ m/s}$ in a reference frame moving with the jet carriage (top), moving with the jet tip (middle) and PIV streamlines (bottom). Actual image size $17 \times 17 \text{ mm}$	123
7.1	Schematic of the underwater jet and velocities in a reference frame fixed with respect to the water tank	125
7.2	Schematic of the underwater jet and velocities in a reference frame fixed with respect to the jet tip	127
7.3	Underwater jet tip velocity (V_p) as a function of V_t/V_j in a stationary reference frame. Jet condition I	133
7.4	Underwater jet tip trajectory angle with respect to the vertical (α_p) as a function of V_t/V_j in a stationary reference frame. Jet condition I	133
7.5	Underwater jet tip velocity (V_p) as a function of V_t/V_j in a stationary reference frame. Jet condition II	134
7.6	Underwater jet tip trajectory angle with respect to the vertical (α_p) as a function of V_t/V_j in a stationary reference frame. Jet condition II	134
7.7	Underwater jet tip velocity (V_p) as a function of V_t/V_j in a stationary reference frame. Jet condition III	135
7.8	Underwater jet tip trajectory angle with respect to the vertical (α_p) as a function of V_t/V_j in a stationary reference frame. Jet condition III	135
7.9	Underwater jet tip velocity (V_p) as a function of V_t/V_j in a stationary reference frame. Jet condition IV	136

7.10 Underwater jet tip trajectory angle with respect to the vertical (α_p) as a function of V_t/V_j in a stationary reference frame. Jet condition IV	136
7.11 Underwater jet tip velocity (V_p) as a function of V_t/V_j in a stationary reference frame. Jet condition V	137
7.12 Underwater jet tip trajectory angle with respect to the vertical (α_p) as a function of V_t/V_j in a stationary reference frame. Jet condition V	137
7.13 Underwater jet tip velocity (V_p) as a function of V_t/V_j in a stationary reference frame. Jet condition VI	138
7.14 Underwater jet tip trajectory angle with respect to the vertical (α_p) as a function of V_t/V_j in a stationary reference frame. Jet condition VI	138
7.15 Two jets of finite breath plunging into each other	140
7.16 Convergence of β and γ for increasing values of h_2/h_1 . $\theta_j = 29.5^\circ$, $V_t/V_j = 0.07$	143
7.17 Shape of the underwater craters computed using the formula of Schwarz without gravity. $\theta_j = 20^\circ$, $V_t/V_j = 0.0$ (top). $V_t/V_j = 0.1$ (bottom). Jet translating from right to left.	144
7.18 Free-body diagram of the accelerations acting on a particle situated at the air-water interface viewed from the steady reference frame fixed to the jet tip	145
7.19 Schematic of the gravitational and non-gravitational shapes of the underwater craters.	151
7.20 R as a function of λ around λ_{opt}	155

7.21	Pinch-off depths (top) and times (bottom) for jet condition I as a function of translating speed. The solid line is the theoretical prediction, and the dots are the experimental values	156
7.22	Pinch-off depths (top) and times (bottom) for jet condition III as a function of translating speed. The solid line is the theoretical prediction, and the dots are the experimental values	157
7.23	Pinch-off depths (top) and times (bottom) for jet condition IV as a function of translating speed. The solid line is the theoretical prediction, and the dots are the experimental values	158
7.24	Pinch-off depths (top) and times (bottom) for jet condition V as a function of translating speed. The solid line is the theoretical prediction, and the dots are the experimental values	159
7.25	Pinch-off depths (top) and times (bottom) for jet condition VI as a function of translating speed. The solid line is the theoretical prediction, and the dots are the experimental values	160
7.26	Jet condition II, $V_t = 0.30 \text{ m/s}$ and $t = \text{pinch-off}$	162
7.27	Pinch-off depths (top) and times (bottom) for jet condition II as a function of translating speed. The solid line is the theoretical prediction, and the dots are the experimental values. It is speculated that the model is not in good agreement with the experiments for this condition due to the free surface effects that appear for large jet inclination angles θ_j	163
7.28	Non-dimensional period associated to the splashes for condition II	165

- 7.29 Crater temporal evolution for jet condition I ($Fr_j = 13.6, \theta_j = 32.5^\circ$). Measured values on left column for jet translating from right to left at $V_t = 0.00 \text{ m/s}$ (top), $V_t = 0.30 \text{ m/s}$ (middle) and $V_t = 0.60 \text{ m/s}$ (bottom). The contours are given in a reference frame moving with the jet carriage, and correspond to four equally spaced times between the jet impact and t_{po} . The contours on the right column were computed with the theoretical model for the same jet conditions and times as the experimental data. 167
- 7.30 Crater temporal evolution for jet condition III ($Fr_j = 16.2, \theta_j = 17.4^\circ$). Measured values on left column for jet translating from right to left at $V_t = 0.00 \text{ m/s}$ (top), $V_t = 0.30 \text{ m/s}$ (middle) and $V_t = 0.60 \text{ m/s}$ (bottom). The contours are given in a reference frame moving with the jet carriage, and correspond to four equally spaced times between the jet impact and t_{po} . The contours on the right column were computed with the theoretical model for the same jet conditions and times as the experimental data. 168
- 7.31 Crater temporal evolution for jet condition IV ($Fr_j = 19.7, \theta_j = 7.1^\circ$). Measured values on left column for jet translating from right to left at $V_t = 0.00 \text{ m/s}$ (top), $V_t = 0.30 \text{ m/s}$ (middle) and $V_t = 0.60 \text{ m/s}$ (bottom). The contours are given in a reference frame moving with the jet carriage, and correspond to four equally spaced times between the jet impact and t_{po} . The contours on the right column were computed with the theoretical model for the same jet conditions and times as the experimental data. 169

7.32	Crater temporal evolution for jet condition V ($Fr_j = 11.4, \theta_j = 29.5^\circ$). Measured values on left column for jet translating from right to left at $V_t = 0.00 \text{ m/s}$ (top), $V_t = 0.30 \text{ m/s}$ (middle) and $V_t = 0.60 \text{ m/s}$ (bottom). The contours are given in a reference frame moving with the jet carriage, and correspond to four equally spaced times between the jet impact and t_{po} . The contours on the right column were computed with the theoretical model for the same jet conditions and times as the experimental data.	170
7.33	Crater temporal evolution for jet condition VI ($Fr_j = 10.0, \theta_j = 23.8^\circ$). Measured values on left column for jet translating from right to left at $V_t = 0.00 \text{ m/s}$ (top), $V_t = 0.30 \text{ m/s}$ (middle) and $V_t = 0.60 \text{ m/s}$ (bottom). The contours are given in a reference frame moving with the jet carriage, and correspond to four equally spaced times between the jet impact and t_{po} . The contours on the right column were computed with the theoretical model for the same jet conditions and times as the experimental data.	171
7.34	Distant traveled by leading edge from impact to $t = t_{po}/2$. Dots are averaged measurements, error bars are 95% confidence intervals, thick line is theoretical prediction using Equation 7.52, and thin line is theoretical prediction neglecting t_a	175
7.35	Jet condition V, $V_t = 0.15 \text{ m/s}$. Sequence of large bubble formation and detachment. Times are $t = t_{po}$ (top), $t = 1.10t_{po}$ (middle), $t = 1.21t_{po}$	177

7.36	Jet condition V. Underwater crater contours from the high-speed movies (left column) at the bubble detachment time. $V_t = 0.00\text{m/s}$, $t = 1.03t_{po}$ (top), $V_t = 0.15\text{m/s}$, $t = 1.10t_{po}$ (middle) and $V_t = 0.30\text{m/s}$, $t = 1.18t_{po}$ (bottom). On the right column, theoretically predicted contours for corresponding values of V_t at the instant when the two crater walls meet. Times are $t = 1.55t_{po}$ (top), $t = 2.01t_{po}$ (middle) and $t = 2.75t_{po}$ (bottom) (t_{po} is the measured pinch of time for each translation speed). The lack of resemblance suggests that the detachment mechanism is associated to effects not considered in the model.	179
7.37	Volume per unit length confined by the the large bubble that forms typically at slow jet translation speeds (Jet condition V). Dots are experimental measurements and solid line, theoretical prediction. .	181
8.1	Theoretically predicted pinch-off times as a function of V_t for various Fr_j (from 10 to 20) and constant $\theta_j = 20\text{ deg}$ (top); pinch-off times for various θ_j angles (from 7 to 35 deg) and constant $Fr = 10$ (bottom)	187
8.2	Theoretically predicted pinch-off depths as a function of V_t for various Fr_j (from 10 to 20) and constant $\theta_j = 20\text{ deg}$ (top); pinch-off depths for various θ_j angles (from 7 to 35 deg) and constant $Fr = 10$ (bottom)	188

Chapter 1

Motivation

Air entrainment by a plunging jet into a receiving pool of the same liquid is of particular interest within the geophysical, marine, chemical and energy sciences due to its importance in aeration of the ocean by plunging breaking waves, generation of bubbly wakes by bow waves on ships, its simplicity and efficiency as a gas/liquid reactor, its occurrence behind weirs in open channel flows, and its role in breaking down slugs of gas in two-phase pipe flows. As an example, the environmental implications of plunging jets in relation to the aeration of the ocean are explained in some detail in the following sections.

1.1 The Greenhouse Effect

The air entrainment and the production of bubbles by breaking waves greatly enhances the absorption of atmospheric gases by the oceans. Some of these atmospheric gases are responsible for a continuous increase of the mean temperature of the Earth due to the greenhouse effect. In this section, a brief overview

of the main concepts related to the greenhouse effect is given as well as some quantitative data on the contribution of the oceans to alleviate its effects.

The Sun radiates energy as a black body at 5800 K . The wavelength of the maximum radiated energy flux for a black body can be found using Wien's law:

$$\lambda_p = \frac{2.898 \cdot 10^{-3}}{T} \quad (1.1)$$

where λ_p is in meters and T is in K . Thus, λ_p for the Sun corresponds to approximately 0.5 μm , and most of the Sun's energy is radiated in the range of wavelengths from 0.4 to 4 μm . The Earth, located 150 million kilometers away, absorbs almost half of the radiation that reaches its location. To maintain equilibrium, the Earth must radiate an equivalent amount of energy. Given the cooler temperature of the Earth (black body temperature equal to 254 K), the energy is radiated in the infrared range with wavelengths ranging from 4 to 100 μm . The atmosphere is semitransparent to solar radiation, but almost opaque to the infrared radiation; therefore, atmospheric gases, clouds and particles absorb most of the infrared radiation produced by the Earth. It is predicted that this absorption increases the mean temperature of the Earth's surface an average of 33°C [1, p. 9] over what would exist for a non-absorbing atmosphere. This phenomenon is commonly known as the greenhouse effect. Water vapor, carbon dioxide, methane and ozone are the atmospheric gases that have the largest contribution to the greenhouse effect. The concentration of atmospheric CO_2 , for instance, has increased an estimated 25% since the onset of the industrial revolution mainly due to human-related activities ([1, p30]). The oceans absorb an important amount of the anthropogenic CO_2 emissions (18 to 40% [1, p. 241]).

Thus, in order to predict the amounts of carbon dioxide and other substances in the atmosphere, and therefore their effects on the climate, it is important to account for the ocean-atmosphere gas exchange. The amount of oxygen present in the oceans available for fish and invertebrates is also controlled by the same gas exchange mechanisms.

1.2 Unbroken Surface Ocean-Atmosphere Gas Exchange Models

Several models have been developed to understand the ocean-atmosphere gas exchange. The simplest is called the stagnant film model and assumes that the gas exchange occurs through a diffusive process within a very thin layer close to the interface. The gas flux from the ocean to the atmosphere is then represented by ([1, 2]):

$$F = k_L(C_\omega - k_h p_a) \quad (1.2)$$

where C_ω is the gas concentration in the fluid directly below the film, k_h is the solubility of the gas in seawater and p_a is the atmospheric pressure. The constant k_L is known as the transfer velocity or piston velocity and is defined as:

$$k_L = \frac{D}{z_d} \quad (1.3)$$

where D is the molecular diffusivity of the gas in seawater and z_d is the thickness of the thin layer close to the free surface where diffusion takes place. Various models relating k_L to properties of the air water-system can be found in the literature.

In 1962, Levich proposed an expression based on dimensional scaling arguments for z_d in terms of Q , a velocity scale, and L , a turbulence length scale,

$$k_L = \left(\frac{\kappa D Q}{L} \right)^{1/2} \quad (1.4)$$

where κ is the von Karman constant [3, p 451]. Fortescue and Pearson (1967) for instance, used the turbulence macro scales for Q and L [4]. If Q and L are substituted for the Kolmogorov and dissipation scales, we obtain the model proposed by Tennekes and Lumley in 1972 [5, p. 300],

$$k_L = (\kappa D)^{1/2} \left(\frac{\epsilon}{\nu} \right)^{1/4} \quad (1.5)$$

where ϵ is the turbulence dissipation rate and ν is the kinematic viscosity of the water. There are also gas exchange models that account for the effects of surfactants in the water. In 1972, Davies proposed the following model for contaminated water [6, p. 412].

$$k_L = 0.11 \cdot D^{2/3} \nu^{-1/3} Q \quad (1.6)$$

One difficulty with this model is that the turbulence levels at the free surface are difficult to estimate. However, it is well known that the wind stress plays an important role in generating surface turbulence. Therefore, some k_L models are formulated in terms of the wind speed and those are easier to use in practice. For instance, Wanninkhof published an expression that fitted available oceanic gas transfer data [7].

$$k_L = 2.8 \cdot 10^{-6} \left[0.31 \cdot U_{10}^2 \left(\frac{S_c}{660} \right)^{-1/2} \right] \quad (1.7)$$

where U_{10} is the wind speed at 10 m over the ocean free surface and S_c is the Schmidt number.

1.3 The Effect of Bubbles on the Ocean-Atmosphere Gas Exchange Models

Breaking waves are commonly found at the ocean-atmosphere interface. The formation of air bubbles by breaking waves introduce new gas exchange mechanisms in addition to the diffusive process described in section 1.2. The presence of bubbles, for instance, enhances the gas exchange rate by enlarging the effective contact surface between the two phases. Additionally, hydrostatic pressure and surface tension squeeze the underwater bubbles, facilitating the gas exchange. Studies performed by Wallace and Wirick (1992) [10] and Farmer et al. (1993) [11] (among others) show the relevance of the bubble production in the ocean-atmosphere gas exchange. Despite the new gas-exchange mechanisms introduced by the presence of bubbles, surprisingly, the gas flux has still been extensively modeled in the literature by an expression similar to (1). The effect of the bubbles is accounted for by modifying k_L and substituting the internal pressure of the bubble for p_a in [1]. Memery and Merlivat (1985) [8] showed that k_L depends on the volume of the bubbles. Their arguments were based on the fact that the bubble size determines the relative contributions of the surface tension and the buoyancy forces in the bubble dynamics. Surface tension is the dominant force for small bubbles, whereas buoyancy dominates for large bubbles. As a result, small bubbles are squeezed by the surface tension and tend to dissolve completely in the water. Large bubbles generally rise up to the free surface before they reach equilibrium with the surrounding water. Therefore, each bubble size involves a different behavior and contributes differently to the overall gas exchange. The bubbly plume produced by a breaking wave generally contains a fairly wide range

of bubble sizes. As it has been explained, each bubble size contributes differently to the gas exchange and therefore, it is necessary to know the bubble size distribution present in the plume to accurately model the gas exchange. In 1993, Merlivat et al. [9] proposed the following functional form for the transfer velocity due to the presence of bubbles:

$$k_B = b_1 \alpha^{-m} S_c^{-n'} + \frac{a_1}{\alpha} \quad (1.8)$$

where α is the Ostwald solubility coefficient equal to $k_h R T_\omega$, R is the universal gas constant and T_ω is the water temperature. The constants a_1 , b_1 , m and n' are determined by the concentration of bubbles as a function of size and depth and the path of the bubbles as they rise up to the free surface.

Other effects like the water sprays formed by breaking waves may also enhance the ocean-atmosphere gas exchange. While relevant to the problem of climate modeling and atmosphere/ocean mass transfer, these effects are beyond the focus of the current research.

1.4 Plunging Jets to Study Air Entrainment by Breaking Waves

It is generally accepted that there are four types of breaking waves: spilling, surging, collapsing and plunging. In a spilling breaker, the crest becomes unstable and flows down the front of the wave. In a surging breaker, the crest does not break but the base of the wave's front face advances rapidly with mild breaking while in the collapsing waves, the lower part of the front face steepens and falls creating a foamy surface. Plunging breakers are the most energetic of all types and are typically produced by strong winds in storms. In a plunging breaking wave, the water surface curls up to produce a sheet of water that ejects forward from the crest and impacts on the free surface (see Figure 1.1). Air entrainment and bubble production by plunging breaking waves mainly result from the impact of this water sheet. Therefore, as far as air entrainment is concerned, a breaking wave and a planar plunging water jet are similar problems. The planar jet associated with a breaking wave can be approximately reproduced in a laboratory by recreating the jet geometry, jet impact velocity and impact angle as well as the horizontal relative motion between the jet and free surface (see Figure 1.1). In the plunging jet problem, however, all the kinematic and geometrical parameters are uncoupled and can be varied independently. For this reason, plunging jets are used in this study to emulate the air entrainment processes related to breaking waves. It is the goal of this work to investigate the dynamics of the air entrainment in steady cylindrical jets and transient planar jet impacts; quantify regime boundaries and mechanisms and generate a simple predictive model to help understand the physics of this problem.

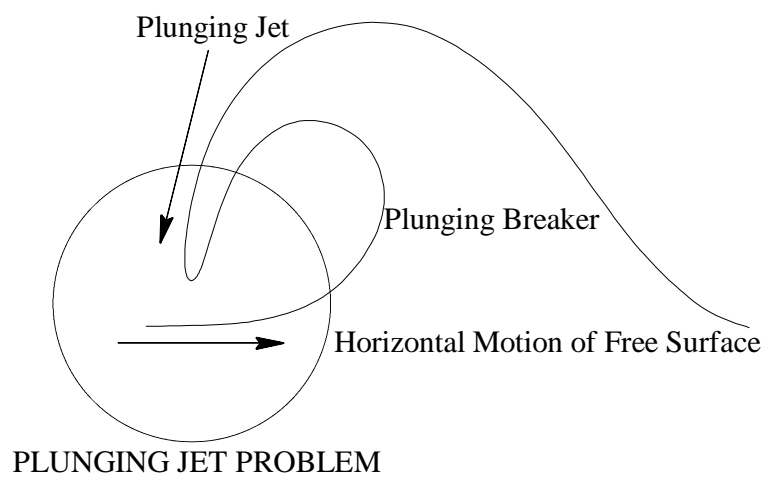


Figure 1.1: Plunging Jet in a Plunging Breaker

Chapter 2

Literature Review and Overview

The literature review on the air entrainment by liquid jets that plunge into a receiving pool is presented here in two parts. Section 2.1 reviews the literature on the air entrainment by continuously running jets and section 2.2, the air entrainment by jets that impact on the pool free surface.

2.1 Continuously Running Jets

In 1965 Lin and Donnelly [12] published the first rigorous study on liquid jets that entrain air into a liquid pool. Since then, air entrainment by plunging jets has been widely studied due to its importance in industrial applications, oceanography, and in the chemical and energy sciences. In the case of continuously running, vertical liquid jets, the nature of the problem changes dramatically depending upon the relative importance between viscosity and surface tension (Bin (1987) [13]). When viscous effects are dominant, the free surface of the pool

is drawn down beneath the pool at the jet impact site. Thus, a sheet of ambient air surrounds the jet under the mean free surface level. When the jet impact velocity overcomes a critical inception velocity, the gaseous sheet becomes unstable and pinches off periodically, producing the entrainment of air bubbles. In contrast to this, when surface tension is large compared to viscous forces, capillary effects produce a slight elevation of the free surface at the jet impact site (Sheridan (1966) [14]). This elevation or ‘meniscus’ is highly stabilizing, which causes inviscid jets to be less susceptible to air entrainment, even at high impact velocities. The entrainment mechanism for these jets usually results from externally produced perturbations in the incoming jet (jet turbulence, for instance), which drive the formation and pinch-off of air cavities below the free surface (Zhu, Oguz and Prosperetti (2000) [15]).

For both viscous and non-viscous jets, the literature has widely reported on the critical inception jet velocity beyond which air entrainment occurs. Lin and Donnelly (1965) [12] determined experimentally the critical inception velocity for laminar jets for a variety of fluids, jet diameters and jet velocities. Their data followed a power law correlation between the Reynolds and Weber numbers at the inception.

$$We = 10 \cdot Re^{0.74} \tag{2.1}$$

Cumming (1975) [16] derived an analytical expression similar to the previous $We - Re$ number relationship with an exponent of 0.5. He derived this expression by balancing the effects of the surface tension, the force due to the entrainment of pool liquid and the force on the pool surface due to the air boundary layer as-

sociated to the jet. He neglected the meniscus and assumed that the jet induced a pool surface velocity equal to the jet velocity in the proximity of the plunging point. Sheridan (1966) [14] analytically estimated the shape of the surface in the vicinity of the jet impact site for a laminar, vertical water jet. Sheridan theorized that entrainment starts to occur when the pressure due to the air entrained in the boundary layer around the jet forces the pool surface at the contact point to slope downward toward the jet axis. For jet diameters between 0.2 and 0.4 *cm*, the theory and Sheridan’s experiments with water agree with an inception velocity of approximately 2.3 *m/s*. At larger diameters (> 0.4 *cm*), the experimental values of the incipient velocity drop while the theoretical value remains unchanged. McKeogh and Elsayy (1980) [17] and Ervine, McKeogh and Elsayy (1980) [18] performed a series of experiments with water jets that showed that the incipient velocity was independent of the jet diameter and strongly dependent on the jet turbulence level (for jet diameters ranging from 2.75 to 14.5 *mm*). They obtained an average incipient entrainment velocity equal to 0.8 *m/s* for jets issuing with a turbulence level of 5% and an incipient entrainment velocity equal to 2.8 *m/s* for turbulence levels of 1%. Additionally, they identified visually three different air entrainment mechanisms that were named “Annular Oscillations”, “Intermittent Vortex” and “Turbulent Occlusion”. Each mechanism occurred within a specific range of jet turbulence level ($<1\%$, 1% and $>2\%$ respectively). Zhu, Oguz and Prosperetti (2000) [15] performed experiments with a non-viscous, vertical, axisymmetric, continuously running, disturbance-free jet where no air entrainment occurred, even for Reynolds and Froude numbers exceeding the thresholds reported by earlier investigators. They stated that their jet nozzle was specially designed to minimize jet turbulence, unlike some of the previous authors’. They

reiterate that artificial disturbances on the incoming jet need to be produced for the air to be entrained.

The jet impact angle has also been found to have a large influence on the critical inception velocity for plunging jets. For instance, Detsch and Sharma (1990) [19] conducted a series of experiments with fluids of different densities, viscosities and surface tensions. They published an empirical equation that gives the critical angle of incipient entrainment as a function of surface tension, viscosity, density and jet velocity. The equation holds “moderately” well (as they report) for Re numbers between 800 and 10000. No measurements or estimates of the jet turbulence levels are reported in their paper. The authors state that their equation holds for jets in the “Intermittent Vortex” entrainment regime defined earlier by McKeogh and Elsayy (1980) [17] and Ervine, McKeogh and Elsayy (1980) [18].

In addition to the critical inception velocity, the amount of air entrained has been traditionally examined in the literature. Van de Sande and Smith (1975) [20] derived an equation to predict the amount of air entrained for plunging water jets with velocities between 2 and 5 m/s . Their model was based on simple energy considerations. Van de Sande and Smith (1972) [21] developed another theory on the amount of air entrained by high impact velocity jets. They assumed that the accompanying air boundary layer was laminar ($Re > 5 \cdot 10^5$) and that the jet was submitted to air friction forces ($We > 10$). The constant We is defined as the ratio of air friction to surface tension forces. Both theories are in good agreement with the experiments. McKeogh and Ervine (1980) [22] published an empirical correlation that gives the amount of air entrained by water jets as a function of the flow rate and the turbulence level. In the same paper,

the authors presented a method to approximately predict the air concentration pattern in the underwater jet plume and the penetration depth of the aerated region. Sene (1988) [23] showed that the air entrainment rate strongly depends on the jet turbulence intensity. His theoretical and experimental arguments show that the air entrainment rate varies with the third power of the jet impact velocity for impact velocities up to a few meters per second. At high speeds, the air entrainment rate grows with the jet impact velocity raised to the $3/2$ power and unlike the low speed jets, the air entrainment rate appears to be independent of the surface tension of the liquid. These results are valid for both axisymmetric and planar jets.

2.2 Impacting Jets

The transient impact of a water jet on a pool is another problem of interest. In this case, the jet impact opens up a crater in the pool that results in a large entrained air bubble. The submerged bubble subsequently fractures into smaller bubbles. Oguz, Prosperetti and Kolani (1995) [24] studied the impact of a nearly cylindrical water jet on a water pool, both experimentally and theoretically. Their experimental range of velocities and length scales were associated with large Re and We numbers (negligible viscous and surface tension forces). This scaling allowed the authors to use powerful arguments based on potential flow and physical reasoning to obtain simple yet surprisingly accurate descriptions of the bubble formation process. The fundamental ideas of the previous work will be explained here in some detail due to their intimate relationship with this thesis. The jet and crater geometry is given in Figure 2.1. They developed a model based on the Rankine half-body flow that predicted a radius of the entrained crater (R_c) equal to $\sqrt{3} \cdot r$, where r is the jet radius. In the experiments, R_c/r remains approximately constant close to 2. The velocity of penetration of the water mass was found to be equal to one half of the jet impact velocity U . This result is in good agreement with steady-state potential theory. According to this result, the underwater jet and the crater reach a depth z in a time equal to $2z/U$. Any two points situated on opposite walls of the underwater crater will have a tendency to move towards each other due to the hydrostatic pressure from the surrounding body of fluid. Since the characteristic width of the crater is of the order of R_c , the characteristic time of the closure of the crater at z should be of the order of R_c/\sqrt{gz} .

Therefore, the total closure or “pinch-off” time of the crater, t_c , at a given

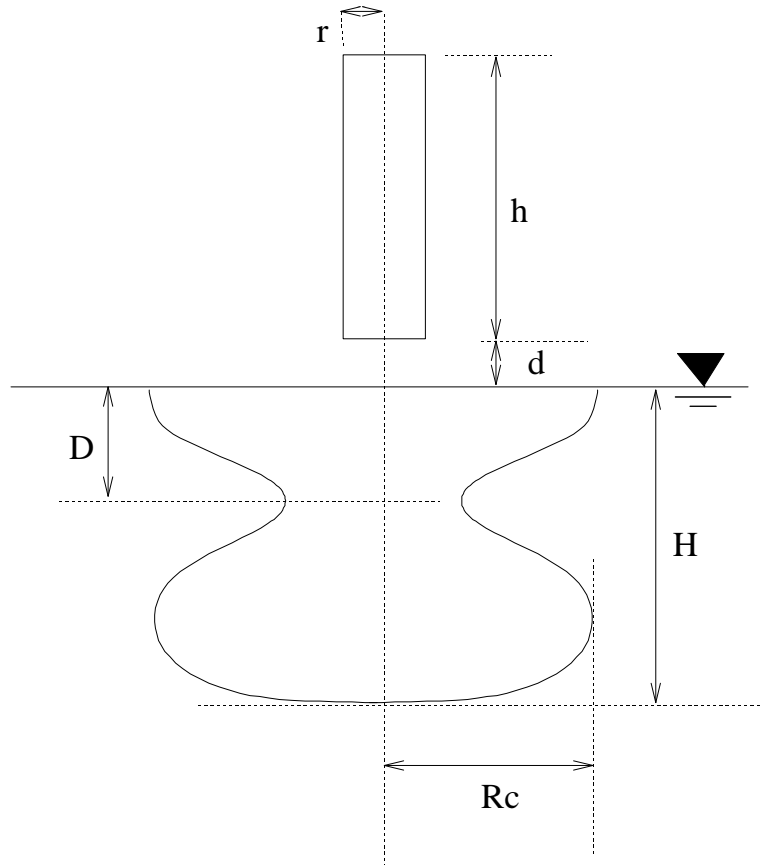


Figure 2.1: Schematic of the above and under water geometry of a water mass falling on a water pool.

depth z is given by the following.

$$t_c(z) = \frac{2z}{U} + \beta \frac{R_c}{\sqrt{gz}} \quad (2.2)$$

where β is a coefficient of order one. The authors estimated the depth (D) at which the crater first pinches off by calculating the local minimum of $t_c(z)$,

$$\frac{D}{r} = \left(\beta \cdot \frac{1}{4} \frac{R_c}{r} \right)^{2/3} Fr^{1/3} \quad (2.3)$$

The constant Fr is the Froude number defined in terms of r and U . The ‘‘pinch-off’’ time ($t_{c,D} = t_c(D)$) is given by

$$\left(\frac{g}{r} \right)^{1/2} t_{c,D} = \frac{3}{2} \left(2\beta \frac{R_c}{r} \right)^{2/3} Fr^{-1/6} \quad (2.4)$$

The depth of the crater at $t = t_{c,D}$ is given by

$$H_c = \frac{1}{2} \cdot U t_{c,D} \quad (2.5)$$

or

$$H_c = 3D \quad (2.6)$$

By assuming that the kinetic energy of the incoming jet is completely transformed into potential energy to form the crater, the depth of the crater is given by

$$H_p = \frac{r}{R_c} h \left(1 + \frac{2d}{h} \right)^{1/2} \quad (2.7)$$

where h is the height of the entraining water mass and d is the distance of the water mass from the free surface (see Figure 2.1)

$$\frac{H_c}{H_p} = 3 \cdot \frac{R_c}{r} \left(\frac{h}{r}\right)^{-1/2} F_r^{-1/6} \quad (2.8)$$

The ratio H_c/H_p is smaller than 1 for most of the cases investigated meaning that there is some residual energy present in the fluid at the moment at which the crater closes. By subtracting the remaining jet ‘tail’ volume

$$\pi r^2 \left(h - \frac{1}{2} \cdot Ut_c \right) \quad (2.9)$$

from

$$\pi R_c^2 (H_c - D) \quad (2.10)$$

we can get the volume of the entrained air:

$$\frac{V}{\gamma \pi r^3} = 11 \cdot F_r^{1/3} - \frac{h}{r} \quad (2.11)$$

where γ is a shape factor of order 1. This estimate is in very good agreement with the experiments for a value of $\gamma = 1/2$. The authors also performed a potential flow numerical simulation of the problem. They used a boundary-integral technique to calculate the evolution of the underwater crater. The results were

in good agreement with the experiments. Oguz and Prosperetti (1994) [25] and Prosperetti and Oguz (1997) [26] also studied the transient impact of a vertical planar water sheet of thickness W that plunges on a water pool at a velocity U . In their theoretical analysis, they modeled the jet impact by an overpressure on the free surface acting on a strip of width W over a period of time t . The value of the overpressure was equal to the dynamic pressure of the impinging jet $\Delta P = \frac{1}{2} \cdot U^2$. By simple dimensional analysis the authors estimate a scaling for the minimum time T required for the overpressure to produce air entrainment. For a given velocity U , this minimum time is equivalent to a minimum jet length. The scaling is given by

$$\frac{UT}{W} = \lambda \propto Fr^{3/4} \quad (2.12)$$

where λ is the water sheet aspect ratio and Fr is the Froude number based on the sheet impact velocity and sheet thickness. For large enough λ ($t \gg T$), the authors utilized similar dimensional arguments to estimate the volume of entrapped air V .

$$\frac{V}{W^2} \propto Fr \quad (2.13)$$

The authors applied a boundary-integral method to perform numerical simulations of the problem. The authors computed the temporal evolution of the underwater crater. They found that there is a Fr number that maximizes the volume of the entrained air for each finite value of λ . The functional dependence of λ and V/W^2 with the Fr number for large values of λ is in good agreement with the numerical results.

2.3 Lack of Results on Translating Jets

It is intended in this thesis to use plunging jets to investigate some of the aspects related to the air entrainment by breaking waves. In particular, this thesis is concerned about the air entrained by jets produced by breaking waves as they plunge onto the water free surface. The jets produced by plunging breakers are in horizontal relative motion with respect to the free surface and as it will be seen in this thesis, the horizontal jet translation influences dramatically the air entrainment process. No data has been found in the literature on air entrainment by translating jets of any kind.

2.4 Overview of the Present Work

In this thesis, two experiments are addressed: air entrainment due to a steady translating vertical axisymmetric jet and air entrainment due to the transient impact of a translating planar jet. The experiments with the steady axisymmetric jet are described in Chapter 3. The jet nozzle produces a laminar vertical jet and is mounted on a carriage that travels at constant speed over a large receiving pool. The results presented in this chapter reveal that for jets which do not entrain air when stationary, vigorous air entrainment may be achieved when the jet is translated at a velocity equal to only a small fraction of the jet impact velocity. The importance of the jet horizontal translation on the air entrainment becomes then apparent with this work.

In Chapters 4 to 7, the planar jet experiments and theory are discussed. The jet nozzle is mounted on a carriage that travels at constant speed over a large receiving pool and the nozzle is set to various angles relative to the horizontal

so that at impact the angle of inclination of the jet axis relative to the water surface in the pool is varied. Chapter 4 summarizes the construction and design of the facility utilized in these experiments and Chapters 5 and 6 describe the experimental results. The experiments show that upon impact two large open air craters (one at either side of the jet) are created and that these craters evolve in time during the first few milliseconds after the impact and finally collapse and break up into a cloud of bubbles. To achieve a good understanding of the air entrainment by this type of jet, the first step is to understand the dynamics of the craters. A theory describing the crater dynamics is presented in Chapter 7 and predictions of the model are compared to the experimental data. The conclusions for the work on the planar jets are given in Chapter 8.

Chapter 3

Steady Translating Circular Jet

The study on the air entrainment by horizontally translating plunging jets ejected by a plunging breaker was approached in two steps in this thesis. As a first approximation, Chapter 3 investigates the effects of the jet translation by looking at a continuously running, vertical, horizontally translating circular jet. In further chapters, a closer approximation to the actual wave problem is presented where the transient impact of a horizontally translating, inclined planar jet is researched.

3.1 Experimental Set-Up

3.1.1 Water Tank and Jet Nozzle

A quiescent liquid jet was created from a high contraction-ratio nozzle located at the bottom face of an acrylic chamber fed by a centrifugal pump. Water from the pump entered the chamber through four inlets that were located on the top face. To reduce turbulence, the water flowed towards the center of the chamber through

a 5-*cm*-thick annulus bounded by two metallic screens and filled with spherical glass beads (approximately 0.3 *cm* in diameter) (see Figure 3.1). The jet exited the chamber vertically downward to plunge onto the pool. Three interchangeable nozzles were used to vary the jet exit diameter. The chamber, the annulus and the nozzles were designed to achieve the lowest possible levels of jet turbulence.

The chamber was mounted on top of a carriage that ran along two tracks situated on top of a water tank that is 1480 *cm* long, 120 *cm* wide and 100 *cm* deep.

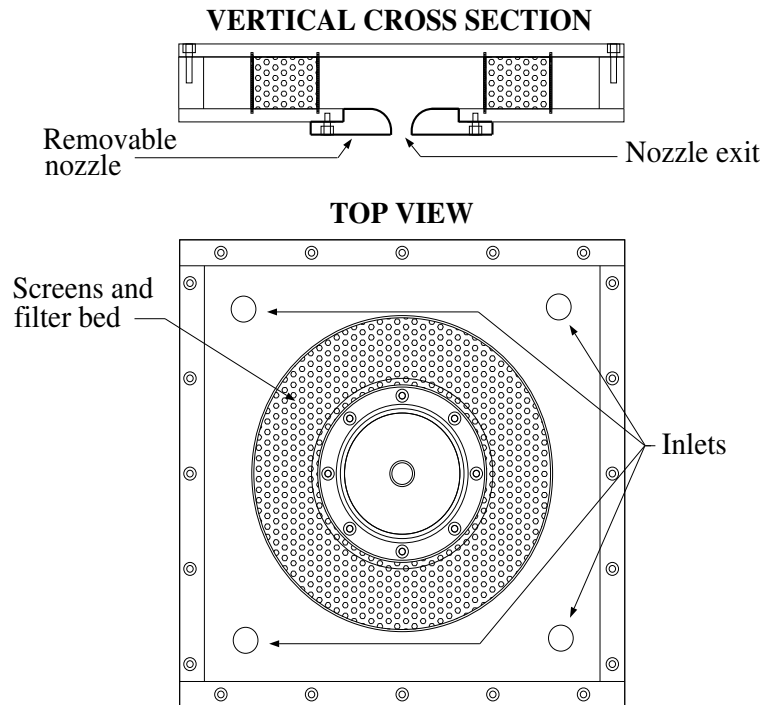


Figure 3.1: Schematic of chamber utilized for the circular jet experiment

The carriage was supported above the tracks via four hydrostatic oil bearings, thereby greatly reducing vibration and friction levels. The water jet translated

with the carriage at a velocity V_t . The centrifugal pump that fed the jet nozzle was mounted on the side of the carriage. To eliminate jet instabilities caused by pump-induced carriage vibrations, the pump and the nozzle chamber were mounted on dampers. The intake pipe for the pump extended vertically into the water from the top of the carriage and was located about 100 cm downstream of the jet chamber. A computer controlled the position and velocity of the carriage through two towing wires powered by a servomotor. The sidewalls of the tank were made of glass to allow for flow visualization and optical measurements. The quality of the water was ensured by a filtration and skimming system and the surface tension was monitored with a Wilhelmy plate in combination with a Langmuir trough as described in Duncan et al (1999) [27].

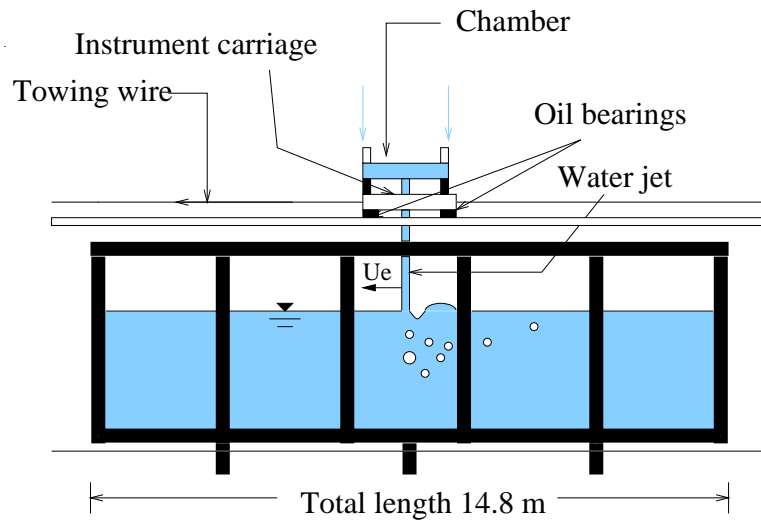


Figure 3.2: Lateral view of the water tank used for the circular jet experiment

3.1.2 High-Speed Imaging

Observations of the water jet impact point region were performed with a high-speed camera (Vision Research, Phantom V3.0) mounted on a support attached to the carriage. The camera translated horizontally with the carriage and recorded images through the glass sidewall from above and below the pool's free surface. Movies to determine the entrainment boundaries described in the following sections were recorded at 500 Hz whereas the visualizations of the entrainment process were performed at 1635 Hz . In the latter, the water jet was seeded with small particles so the jet became visible when viewed from below the free surface. The flow was backlit with a continuous source of light also attached to the carriage. A light diffuser was attached to the glass sidewall of the tank closest to the light source to produce a more uniform lighting. (see Figure 3.3).

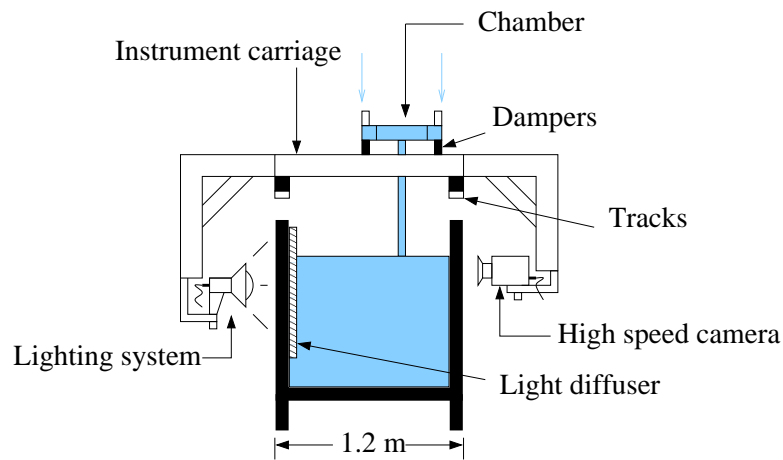


Figure 3.3: Side view of the water tank

3.1.3 Still Pictures

In order to record high-resolution illustrative pictures (as shown later in Figures 3.5 through 3.10) the high-speed camera and the continuous light source were replaced by a 35 *mm* camera (Nikon F3) with a 200 *mm* lens and a strobe with a duration of 3.3×10^{-5} *s*. The pictures were recorded on Kodak Tmax-100 film.

3.1.4 Characterization of the Jet

In order to characterize the jet, the centerline mean velocity (v) and root-mean-square velocity fluctuation (v') were measured using a single component laser-Doppler velocimeter (LDV). The ratio v'/v was smaller than 0.35% for all the experimental conditions.

3.2 General Description of the Flow and Measurements of the Boundaries Between Entrainment Regimes

The jet impact velocity, V_j , and the jet impact diameter, D_j , depend on the nozzle diameter, the height of the chamber with respect to the free surface, and the flow rate delivered by the pump. By varying these three parameters, 21 combinations of D_j and V_j were achieved. The jet impact diameter (D_j) ranged from 0.33 *cm* to 1.21 *cm* and the jet impact velocity (V_j) from 104 *cm/s* to 365 *cm/s*. No air entrainment was observed to occur for any of the 21 combinations when the jet was stationary (Figure 3.4). Figure 3.4 shows the characteristic meniscus of low-viscosity plunging jets described in section 2.1. Figures 3.5 through 3.10 show some of the main features of the above and under water flow fields induced by the jet when translated. In the pictures, the jet translates from right to left. The pictures on the top of the figure were taken from above the free surface of the pool. Each above-water picture is associated with a corresponding image captured from a submerged perspective, as shown in the pictures at the bottom of the figure. Each pair of pictures then represents a single condition.

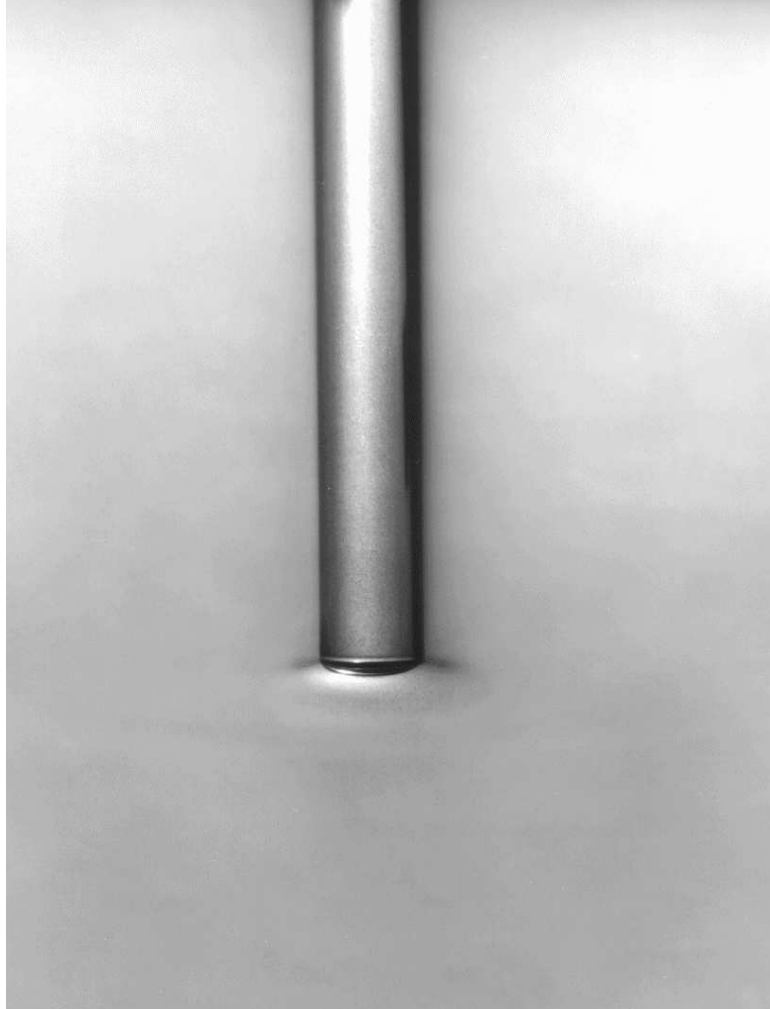


Figure 3.4: Above-water view of the jet impact site. $V_j = 303 \text{ cm/s}$, $D_j = 0.6 \text{ cm}$, $V_t = 0.0 \text{ cm/s}$

The six pictures were taken for jets with the same $D_j = 0.6 \text{ cm}$ and the same $V_j = 303 \text{ cm/sec}$. The only difference between the three pairs of pictures is the horizontal velocity V_t at which the jet was translated. The figures 3.5 and 3.6 were taken at a horizontal translating velocity V_t equal to 31.8 cm/sec . Capillary waves form upstream from the jet impact point and a small air cavity is found immediately behind it. There is no air entrainment in this case. Figures 3.7 and 3.8 correspond to a translating velocity of 38.1 cm/sec . As a consequence of this slightly larger translating velocity, the capillary waves have a shorter wavelength and the air cavity behind the jet is bigger. The air cavity has a sharp cusp at the bottom that occasionally pinches-off producing small air bubbles. This regime is called the ‘incipient entrainment regime’. If V_t is sufficiently increased, ($V_t > 44.5 \text{ cm/sec}$ in this case) the jet induces vigorous air entrainment. Bursts of bubbles are produced intermittently (Figure 3.9 and 3.10). This regime is called the ‘intermittent entrainment regime’. If the jet is translated even faster, air entrainment occurs in a continuous fashion. This regime is called the ‘continuous air entrainment regime’.



Figure 3.5: Above-water view of the jet impact site for no air entrainment conditions. $V_j = 303 \text{ cm/s}$, $D_j = 0.6 \text{ cm}$, $V_t = 31.8 \text{ cm/s}$



Figure 3.6: Below-water view of the jet impact site for no air entrainment conditions. $V_j = 303 \text{ cm/s}$, $D_j = 0.6 \text{ cm}$, $V_t = 31.8 \text{ cm/s}$



Figure 3.7: Above-water view of the jet impact site for incipient entrainment conditions. $V_j = 303 \text{ cm/s}$, $D_j = 0.6 \text{ cm}$, $V_t = 38.51 \text{ cm/s}$



Figure 3.8: Below-water view of the jet impact site for incipient entrainment conditions. $V_j = 303 \text{ cm/s}$, $D_j = 0.6 \text{ cm}$, $V_t = 38.51 \text{ cm/s}$

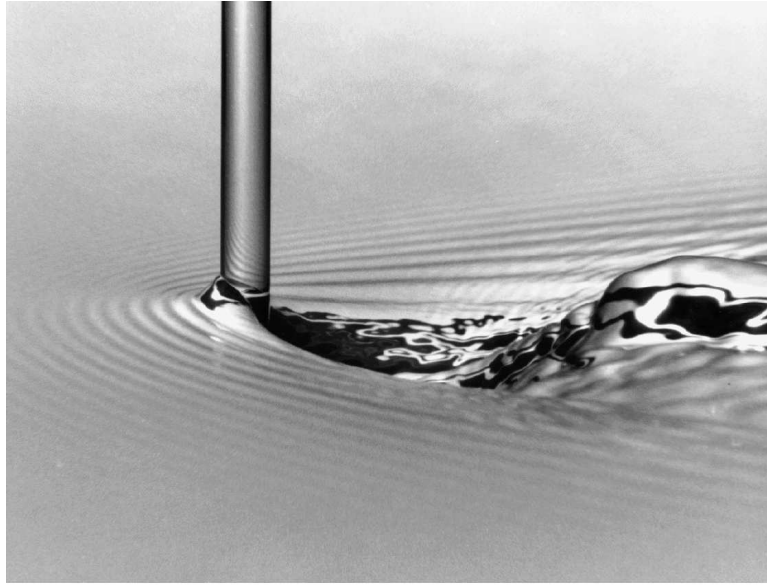


Figure 3.9: Above-water view of the jet impact site for intermittent entrainment conditions. $V_j = 303 \text{ cm/s}$, $D_j = 0.6 \text{ cm}$, $V_t = 44.5 \text{ cm/s}$



Figure 3.10: Below-water view of the jet impact site for intermittent entrainment conditions. $V_j = 303 \text{ cm/s}$, $D_j = 0.6 \text{ cm}$, $V_t = 44.5 \text{ cm/s}$

For each of the 21 D_j - V_j combinations, a set of underwater high-speed movies of the jet impact was taken for different values of V_t . The values of V_t were selected iteratively to locate the boundaries between the above-mentioned regimes. The results are summarized in Table 3.1 and Table 3.2.

Exp Cond	Nozzle Diam	Jet height	Jet Flowrate	Impact Diam	Impact Veloc	Trans Veloc Bound		
						Incip	Interm	Cont
	D_n (cm)	h (cm)	Q (cm ³ /s)	D_j (cm)	V_j (cm/s)	V_{ic} (cm/s)	V_{it} (cm/s)	V_c (cm/s)
1	0.72	18.8	32.1	0.45	204	30.5	34.3	38.1
2	0.72	18.8	60.1	0.57	237	33.7	38.1	41.9
3	0.72	18.8	98.2	0.65	298	35.6	43.2	47.0
4	1.27	18.8	60.7	0.63	192	35.6	38.1	40.6
5	1.27	18.8	107.4	0.83	201	40.0	41.9	43.2
6	1.27	18.8	81.6	0.71	207	36.8	39.4	41.3
7	0.41	19.7	31.6	0.36	315	27.3	45.7	50.8
8	0.41	34.0	31.6	0.33	365	25.4	45.7	52.1
9	0.72	33.4	32.1	0.39	272	25.4	40.6	44.5
10	0.72	33.4	60.2	0.52	283	28.6	41.9	45.7

Table 3.1: Experimental conditions and entrainment boundaries.

Exp Cond	Nozzle Diam	Jet height	Jet Flowrate	Impact Diam	Impact Veloc	Trans Veloc Bound		
						Incip	Interm	Cont
	D_n (cm)	h (cm)	Q (cm ³ /s)	D_j (cm)	V_j (cm/s)	V_{ic} (cm/s)	V_{it} (cm/s)	V_c (cm/s)
11	1.27	33.4	60.2	0.54	260	33.0	41.9	47.0
12	1.27	33.3	31.8	0.40	256	28.6	40.6	44.5
13	1.27	33.3	81.8	0.63	264	34.3	40.6	41.9
14	1.27	33.3	108.2	0.72	269	36.8	43.2	44.5
15	1.27	33.3	159.3	0.85	283	38.7	45.7	47.0
16	1.27	2.8	248.9	1.21	216	43.2	45.7	48.3
17	1.27	2.8	121.6	1.15	118	37.5	38.7	40.6
18	0.72	2.7	31.4	0.62	104	30.5	33.0	-
19	0.72	2.7	60.4	0.67	172	34.3	36.2	37.5
20	0.72	2.7	107.7	0.70	282	38.1	43.2	45.7
21	0.41	3.6	17.6	0.37	161	29.8	29.8	31.1

Table 3.2: Continuation of Experimental conditions and entrainment boundaries.

3.3 Dimensional Analysis - Fr Number vs. Velocity Ratio Diagram

In general, the entrainment conditions may depend on the liquid density, ρ_l , the gas density, ρ_g , the liquid viscosity, μ_l , the gas viscosity, μ_g , the surface tension, σ , the gravitational acceleration constant, g , the diameter of the jet, D_j , the impact velocity, V_j , and the translation velocity, V_t . These parameters can be reduced to six non-dimensional independent parameters through the use of dimensional analysis:

$$Fr = \frac{V_t}{\sqrt{gD_j}}; W_e = \frac{\rho_l D_j V_t^2}{\sigma}; Re = \frac{\rho_l D_j V_j}{\mu_l}; R = \frac{V_j}{V_t}; \gamma = \frac{\rho_g}{\rho_l}; \psi = \frac{\mu_g}{\mu_l} \quad (3.1)$$

Since both working fluids (air and water) were kept constant, both the density ratio and viscosity ratio were fixed. The functional relationships between the remaining dimensionless ratios were examined, along with numerous combinations of these terms. The best correlation by far was produced by plotting Fr vs R as shown in Figure 3.11.

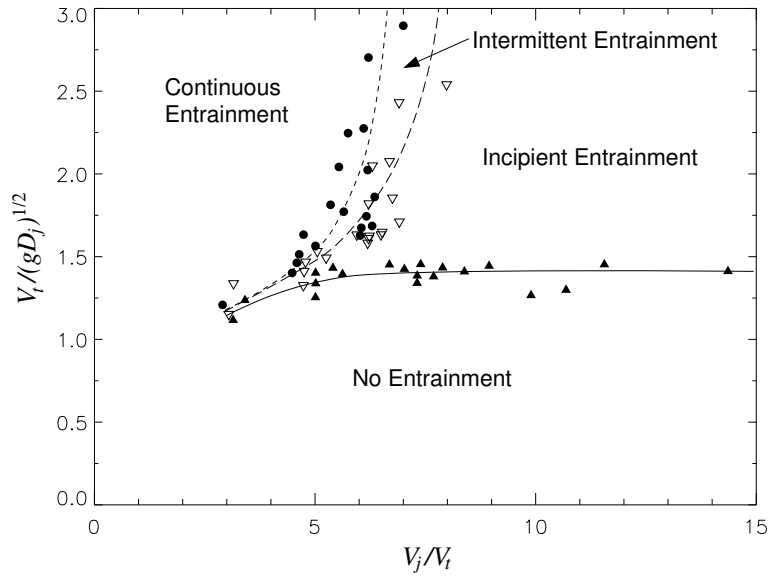


Figure 3.11: Froude number vs velocity ratio the different entrainment regimes

The correlation in Figure 3.11, implies that the inception process is dominated by inertial and gravitational effects and this idea is supported by the relatively large Weber numbers (varying from 91.9 to 932.5), Reynolds numbers (varying from 5370 to 21820), and Bond numbers ($B = W_e/F_r^2 = \rho_l g D_j^2 / \sigma$ varying from 1.46 to 19.67) in the data. It is presumed that if it were possible to do experiments with a different range of parameters including the use of several fluids with a wide range of surface tensions and viscosities, the dependence of the results on other dimensionless numbers would become apparent. As can be seen in Figure 3.11, at high velocity ratios, the boundary between no entrainment and incipient entrainment (solid line) is nearly horizontal. The average Froude number of this boundary is 1.4 with a standard deviation of 0.1. At low velocity ratios, all three boundaries nearly coincide. It is speculated that this coincidence of the entrain-

ment boundaries at low jet velocity ratios is associated with the tendency of the underwater trajectory of the jet to bend further downstream into the tip of the surface depression in those cases. This fact may result into a stronger interference between the depression and the underwater jet turbulence leading to continuous entrainment for a wider range of Fr numbers.

3.4 Entrainment Mechanism

To achieve a better understanding of the entrainment boundary data, a set of visualization experiments was performed using jet fluid that has been marked with particles. Four of the 21 above-mentioned D_j - V_j combinations were selected and for each combination, four movies were taken at conditions corresponding to pre-, incipient, intermittent, and continuous entrainment. A number of general observations were made from the movies. First, vortices forming on the shear layer surrounding the submerged jet can be seen on the upstream side of the jet just below the free surface under all conditions (Figure 3.12).

Second, small downward traveling undulations form on the leading edge of the surface depression behind the jet. Third, the depth of the cusp of the depression increases with increasing V_t and begins to oscillate vertically as the incipient entrainment boundary is approached. Several image sequences were processed to determine the temporal variations of the vertical positions of the vortex centers, the peaks in the undulations on the leading edge of the surface depression, and the cusp tip. These positions were determined by displaying each image on a computer screen and locating each position by eye with the cursor.

Plots of the axial position of these various features as a function of time have been constructed in the form of an x-t diagram to aid in the understanding of the flow dynamics (Figures 3.13, 3.14 and 3.15). The vertical position of the vortices and undulations follow straight lines with approximately the same slope in a vertical position versus time diagram. This indicates that they have approximately the same vertical velocity. The depth of the cusp tip oscillates slightly around a constant value; the period of this oscillation is the same as the period associated with the leading edge undulations and vortices passing a

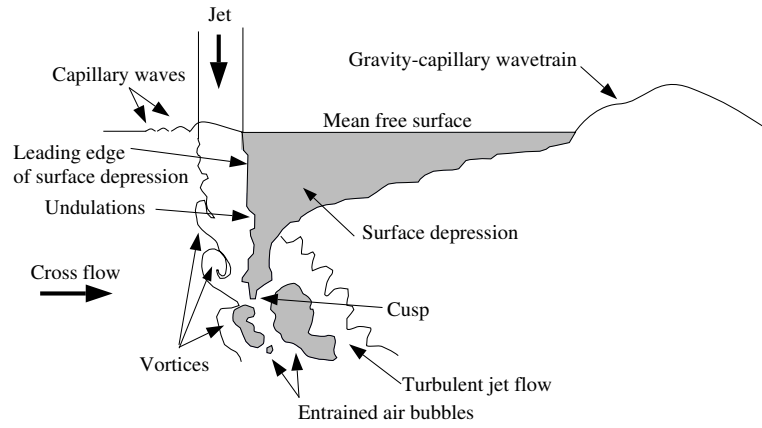


Figure 3.12: Nomenclature for the entraining jet flow shown in the reference frame moving with the jet. The schematic on the top is a schematic of the underwater picture on the bottom.

fixed point. A similar plot for a different time period and the same incipient entrainment condition is given in Figure 3.14.

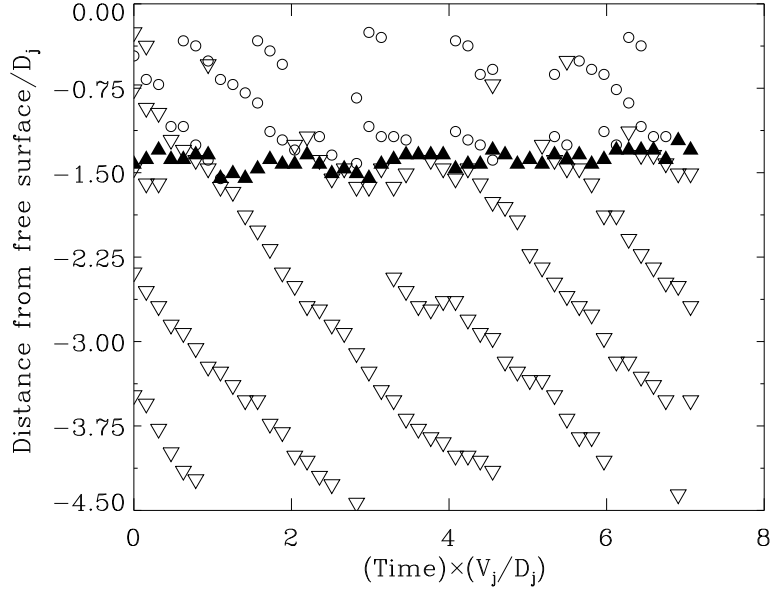


Figure 3.13: Temporal evolution of the depth of the vortices, undulations on the leading edge of the cavity, and the cusp of the cavity for an incipient entrainment case. $D_j = 0.67 \text{ cm}$, $V_j = 172 \text{ cm/s}$. White triangles are vortex centers, circles are undulations on cavity leading edge and black triangles are cusp's position.

In this second plot, a single bubble is entrained at a time of about $3D_j/V_j$ and its vertical position is tracked versus time. As can be seen in figure 11, the bubble is entrained during one of the downward excursions of the cusp. The trajectory of the bubble is nearly parallel to that of the vortex that passed over the cusp at the time of the bubble entrainment. In agreement with this data, the high-speed movie shows that the bubble is entrapped within a vortex. The above-mentioned

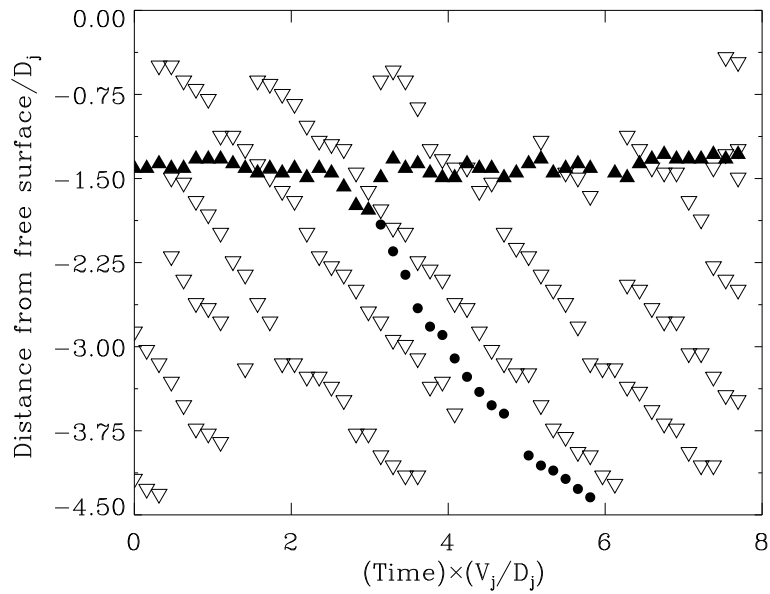


Figure 3.14: Temporal evolution of the depth of the vortices, a single entrained small bubble, and the cusp of the cavity for an incipient entrainment case. $D_j = 0.67 \text{ cm}$, $V_j = 172 \text{ cm/s}$. White triangles are vortex centers, circles represent the entrained bubble and black triangles are cusp's position.

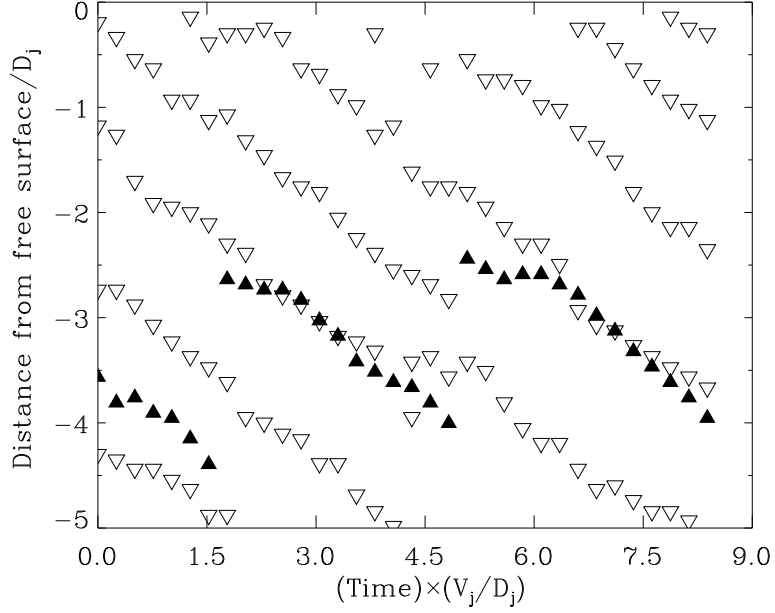


Figure 3.15: Temporal evolution of the depth of the vortices, and the cusp of the cavity for an intermittent entrainment case. $D_j = 0.57 \text{ cm}$, $V_j = 237 \text{ cm/s}$. White triangles are vortex centers and black triangles represent the cusp.

findings point to the important roles of the cusp depth and the jet vortices in the incipient entrainment process.

A plot of the depths of the cusp and the vortices versus time for an intermittent entrainment condition is shown in Figure 3.15. As can be seen, the cusp undergoes vertical excursions of about $1.5D_j$. The motion consists of a period of nearly constant downward speed followed by a sudden upward jump. The upward jump is the result of a pinching off of a large bubble rather than a large sudden vertical motion of the cusp. The vortex trajectories have the same velocity and phase as the cusp trajectories, indicating that the cusp motion is likely caused by the

vortices. A sequence of five frames from the corresponding high-speed underwater movie is shown in Figures 3.16 and 3.17. In the first frame of the sequence, a bubble is forming at the cusp. This bubble is at the same height as one of the vortices, which can be seen on the upstream side of the jet. In the next two frames, a finger of air forms on the upstream side of the bubble as it grows and moves down along with the vortex. In the last two frames, the bubble pinches off from the cusp and the finger pinches off from the main bubble and moves up into the upstream side of the vortex. Though the images show only a silhouette of a three-dimensional phenomenon, it appears that the finger is moving around the periphery of the jet in the center of the ring vortex.

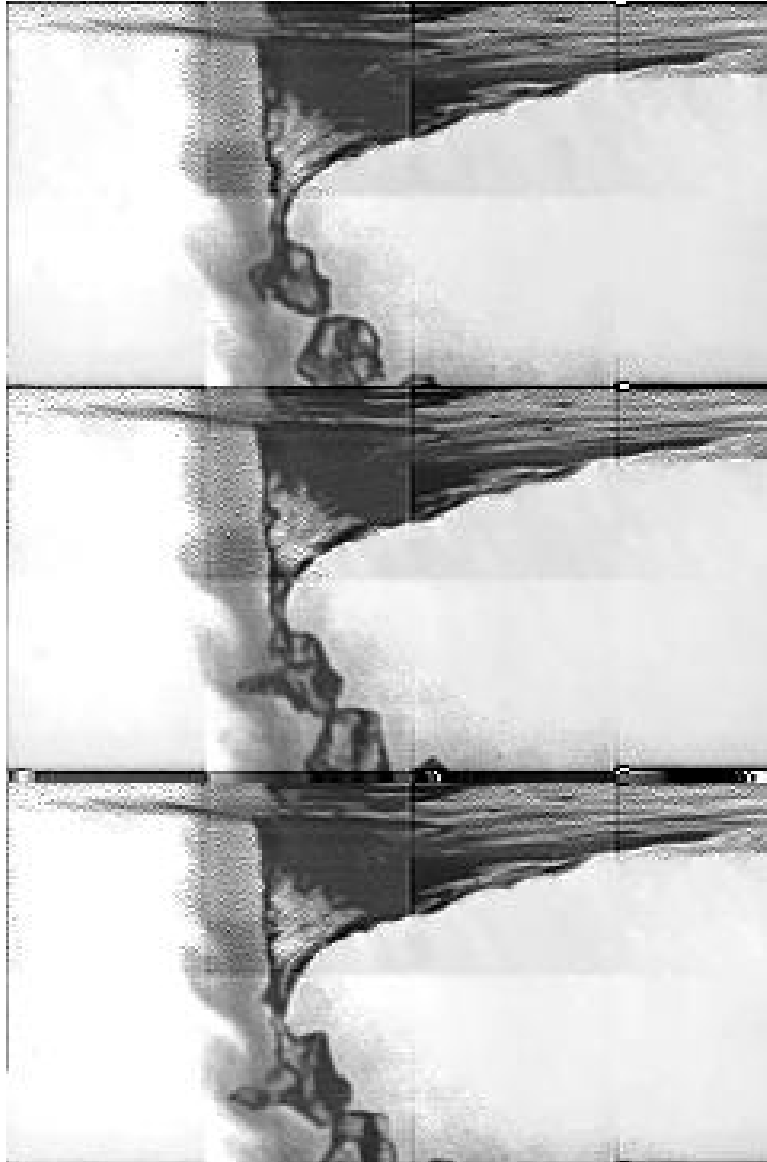


Figure 3.16: Sequence of images of a bubble forming inside a jet vortex. The jet flow is seeded with small particles. The image sequence was taken with a high-speed digital camera. Time between frames = 1.2 ms . $D_j = 0.57\text{ cm}$, $V_j = 237\text{ cm/s}$ and $V_t = 38.1\text{ cm/s}$

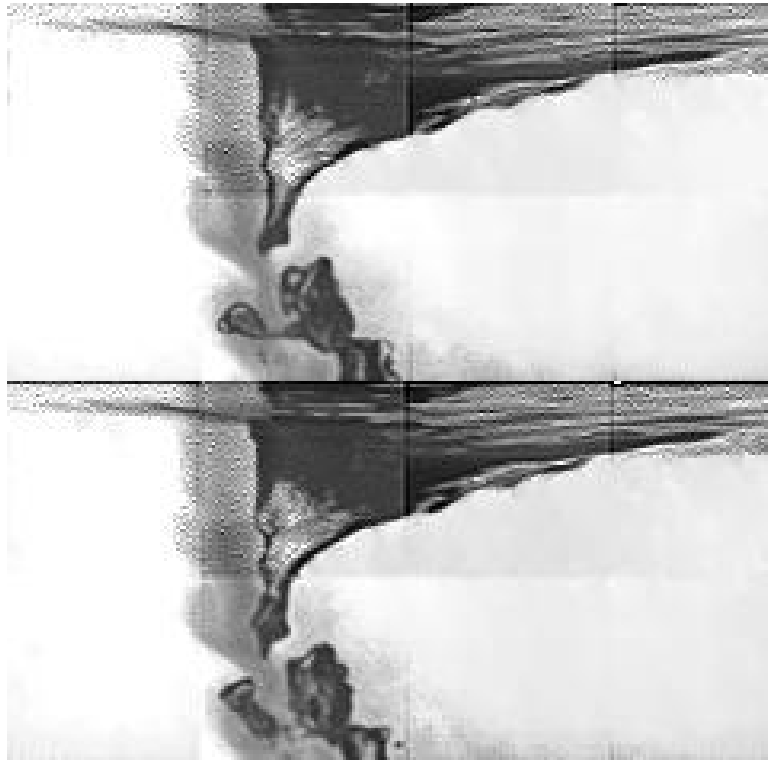


Figure 3.17: Sequence of images continuation of Figure 3.16

In order to further assess the influence of the downward motion of the jet and the jet vortices on the entrainment process, an underwater view of the free-surface interface produced by a solid, surface-piercing rod is shown in Figure 3.18. The towing speed and rod diameter are identical to the speed and impact diameter for the intermittent entrainment condition shown in Figure 3.15, $V_t = 44.5 \text{ cm/s}$ and $D_j = 0.6 \text{ cm}$. A comparison of the two photographs shows that in the case of the rod, the depth of the surface cavity is much smaller, no cusp is formed at the leading edge of the interface, and there is no air entrainment. This comparison indicates the important role played by the vertical momentum and large scale flow structures of the jet in dramatically modifying both the mean and fluctuating interface dynamics.

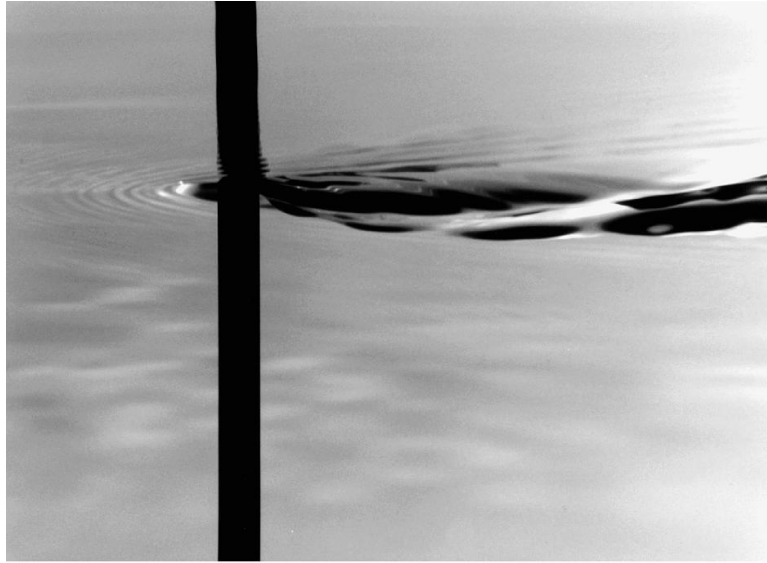


Figure 3.18: Below-water view of a surface piercing solid rod. The upper part of the image of the rod is a reflection from the water surface. The rod diameter and the towing speed are the same as the jet impact diameter and velocity in Figures 3.9 and 3.10, $D_j = 0.6 \text{ cm}$, $V_j = 44.5 \text{ cm/s}$

3.5 Conclusions for the Circular Jet

Air entrainment can be induced by increasing the horizontal speed to a small fraction of the jet impact velocity. When the translating speed is such that the Fr number is slightly larger than 1.4 (where $Fr = V_t/\sqrt{gD_j}$), air entrains in the form of small bubbles. For increasing values of the Fr number, larger air bubbles are observed to form first intermittently and then continuously. The boundaries between the previous entrainment regimes were presented in a Fr vs velocity ratio (V_j/V_t) plot. The vortical structure of the underwater jet seems to play an important role in the air entrainment process.

Chapter 4

Facility Design and Construction for the Impacting Planar Jet

The second part of this investigation focuses on the air entrainment by the jets associated with wave breaking by looking at the transient impact of a horizontally translating, inclined planar jet onto a quiescent water pool. Due to an increased demand for testing time within the water tank used for the circular jet experiments, it was determined that a new dedicated facility was needed for the planar jet experiments. Chapter 4 outlines the design and construction of the new experimental facility.

4.1 General Description and Dimensioning

The main components of the new facility are a water tank, a water skimming and re-circulation system, a carriage, a drive system, a jet nozzle, a jet cutter device to produce the transient impact of the jet on the tank free surface and a

side-plate and trough system to remove the three-dimensional effects associated with the lateral edges of the finite-width jets. All these systems are described in detail in further sections. The main structure of the new water tank consists of a steel beam frame that holds glass side-walls, glass end-walls and a glass bottom confining the water in a 24' long, 2.5' wide and 3' tall rectangular prism situated 2' above the floor level. The tank was designed to have a maximum water depth of 3' while keeping enough space between the glass bottom and the room floor for additional systems like carriage drive cables, laser optics, cameras or lighting.

The steel structure also holds a piping network to fill and drain the tank that connects to a set of water skimmers and to a diatomaceous earth filter. The piping of the water recirculation and skimming systems allows the facility to operate at different water depths, while still being able to filter the tank water to keep it clean.

The carriage, connected to a drive system, can translate along two tracks situated on top and at either side of the tank structure. Similar to the circular jet experiments, the jet nozzle is supported by the carriage and translates with it along with the necessary cameras and lighting.

4.2 Water Tank Steel Frame and Glass

The water tank used for the circular jet experiments had two separate steel structures, one to provide support for the tank walls, and an independent secondary structure to support the carriage. The reason for isolating the structures from



Figure 4.1: Tank structure during the alignment process.

one another was to prevent any vibrations produced by the carriage drive system from being transmitted to the water surface. The experience with the old facility

demonstrated that the carriage vibrations were negligible, and both structures could be integrated into a single frame in the new design to save money, space and effort. The steel structure of the new design was made out of galvanized Unistrut channel. One of the greatest advantages of using Unistrut products is that the different parts come prepared to be bolted together. The whole design was then assembled in an “Erector Set” fashion, where no welding was necessary and final alignment adjustments could be made if needed during the construction process. An image of the assembled Unistrut structure is shown in Figure 4.1. Simple hand calculations were used in order to ensure the structural integrity of the steel frame and a simple finite element model was developed in Ansys to estimate deformations. Note that deformations in the steel structure are an important issue since they influence the design of other parts of the facility and may have serious implications on its overall performance, particularly with respect to the carriage system. Figure 4.2 shows a schematic of the steel structure of the tank. The arrows represent the Ansys predicted deformations (in meters) of the structure under the loads induced by the water where it can be seen that the maximum deflections are found at the tip of the vertical columns. These deflections induce deformations on the carriage tracks that have determining implications on the performance of the carriage translation mechanism. Once the steel frame was built and leveled, it was anchored to the concrete floor. 20 rectangular flat plates of 1/2” thick tempered glass (safety glass) make the bottom, sidewalls and ends of the tank. Therefore, pictures of the jet can be taken at any angle through the tank walls. The lighting can also be set at different angles. The glass bottom shows two holes at either end of the tank that accommodate bulkhead fittings to connect the filtration system, as well as the pipe network required to drain and

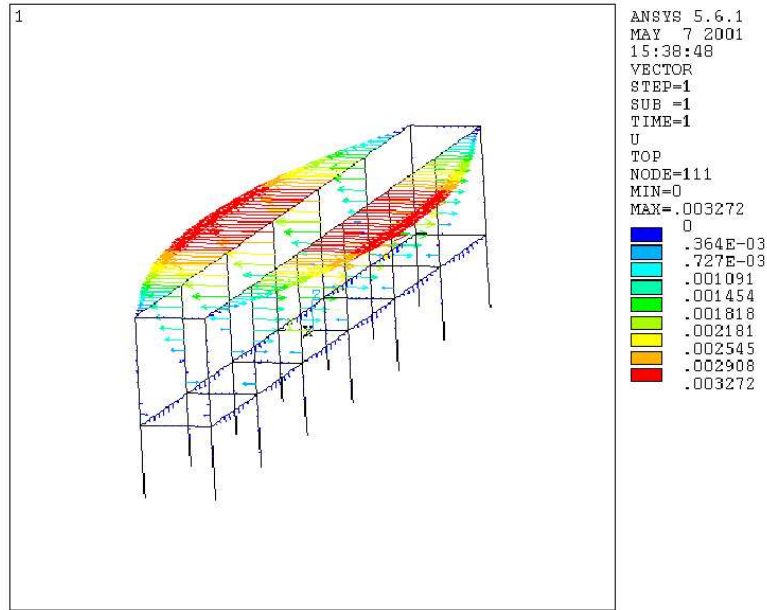


Figure 4.2: Ansys predicted deformations of the steel structure induced by the hydrostatic water pressure

fill up the tank. 1/8" neoprene rubber was placed in between the steel structure and the glass to prevent stress concentrations at contact points, allowing the glass to safely rest on the steel frame. The gaps in between plates are filled with Sikaflex 291 (special silicone for underwater applications), and the vertical glass plates are held to the steel by small aluminum pieces to prevent them from falling while the tank is empty. A finite element model of the glass bottom was made with Ansys for different load cases in order to ensure its structural integrity. The maximum stress on the glass was found to be 16.3 MPa in the worst case whereas the recommended stress design value for this type of glass is 19.31 MPa (18,5% higher). This last value already accounts for a standard safety factor.

4.3 Carriage and Bearing System

Several aluminum beams are attached to the main structure to provide a rigid mounting platform for the instrument carriage rails. A 25' long aluminum strip was mounted on top of the sidewall steel structures approximately one inch from the top of the vertical columns. Each strip was held to the columns by two 25' long L-beams (see Figure 4.3).

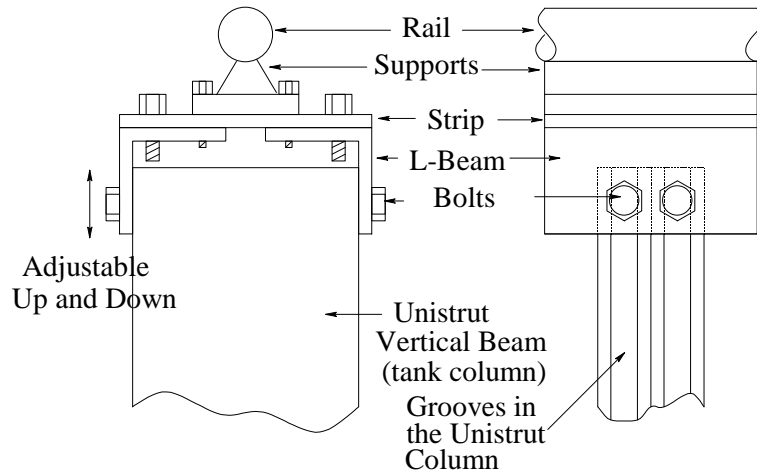


Figure 4.3: Aluminium mountings for the carriage rails

A perfect leveling of the aluminum strips is of major importance for the jet experiment, as the jet must maintain a constant free-fall distance above the free surface as the nozzle translates the length of the tank. The leveling was performed using a precision digital level, and kept to within 0.1° by unbolting and vertically sliding the L-beams with respect to the vertical Unistrut columns.



Figure 4.4: Aluminium L-beams mountings for the carriage rails during the construction process

Other aluminum accessories like pulley supports for the drive system were also mounted to the main structure. The rails that support the carriage are two parallel precision Thomson Industries 3/4" diameter steel shafts. Two self-aligning, open-type, recirculating ball-bearing pillow blocks provided by the same company are mounted onto each rail. A total of four bushings support the weight of the carriage (two on either side of the tank). The shafts are fully supported along the length of the tank and rest on the aluminum strips described before, one on either side of the tank. The jet experiment requires the tank to operate at different heights above the free surface. This will be accomplished by varying the fluid level within the tank, and for each water height, a different level of stress will be felt by the main structure due to differences in the hydrostatic pressure. These variations in applied stress will induce different deformations

on the structure and on the rails in particular. In summary, it will be difficult to keep the two rails perfectly parallel for all the conditions under which the tank will operate due to deformations in the structure (see Figure 4.2). In order to keep the carriage from binding on the rails under these variable conditions, a new degree of freedom needs to be incorporated into the design to allow for deformation of the rail support. This was accomplished using a secondary 8" long Thomson Industries linear system that was set in between the bushings of the main linear system and the bottom of the carriage, perpendicular to the orientation of the main rails (see Figure 4.5). The described deformation

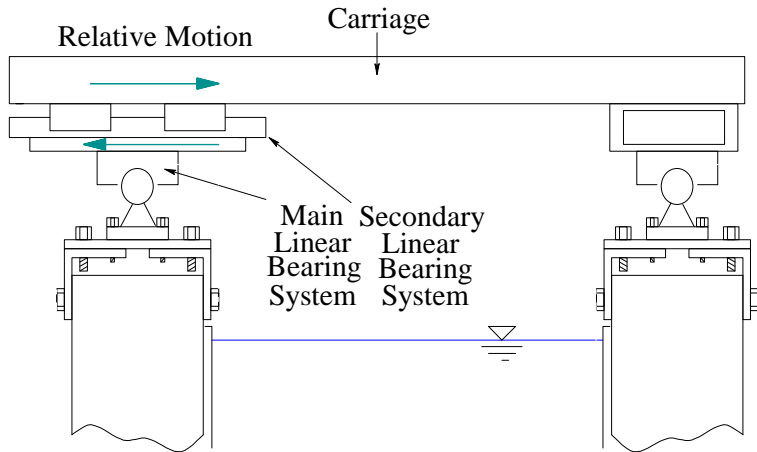


Figure 4.5: Carriage ball bearing systems

of the shafts will also induce slight misalignments between the shafts and the bushings as the carriage moves along the tank. The ball bearing’s self-aligning feature would tolerate a maximum shaft-bushing misalignment of 0.5° , which is well above the maximum misalignment predicted by the Ansys model (0.1°). The design of the linear system was based on maximum deformation requirements

and travel life considerations. In order to drive the carriage along the tank in a controlled manner, a CSM 1.8 HP servomotor equipped with a 5:1 reduction ratio planetary gearhead is utilized. The motor is securely mounted to the floor at one of the ends of the tank, and drives a steel shaft supported by ball bearings that are accommodated in pillow blocks (see Figure 4.6). Two aluminum drums are inserted onto the shaft, which allows positive traction for the steel towing cable. Steel cable is connected via a number of pulleys to the carriage that will be dragged by the cables when the shaft rotates. The angular velocity of the motor is controlled by a computer. The connection between the gearhead and the shaft is done by a universal joint to avoid undesired vibrations induced by slight misalignments of the gearhead shaft and the steel shaft. The carriage itself is a horizontal square frame made of four aluminum box beams bolted together. Four extruded aluminum beams (brand 80x20) are bolted to the frame and stick out horizontally, two at either side of the tank. These beams support two additional extruded aluminum beam structures that come down vertically from them and support cameras, lighting and a computer which translates horizontally along with the carriage during the experiments (see Figure 4.7). The tank is also equipped with an additional safety system to avoid personal injuries or damage of the equipment in case of mishandling of the carriage control system. The safety system consists of two switches situated one at either end of the carriage tracks that would automatically disconnect the power before the carriage could reach the ends of the tracks. Additionally, the safety system has two springs at either end of the tank rigidly mounted to the tank structure to stop the carriage if the carriage accidentally reaches the disconnect switches. The springs are dimensioned to stop a carriage of 100 *Kg* translating at 1 *m/s* with a maximum acceleration of minus



Figure 4.6: Picture of the aluminium drums, shaft, universal joint and steel towing cable



Figure 4.7: Picture of the new instrument carriage. In the image are visible several of the described elements such as the supporting trays for the camera and computer on a side of the tank, the structure that holds the jet nozzle, the long aluminum structures that hold the carriage rails, the bearing systems and the compressed-air reservoir for the jet cutter device (described in later sections).

1 g within a distance of 0.3 m . In normal operating conditions, the carriage should decelerate smoothly as programmed in the controlling PC without the action of the disconnect switches or the stopping springs.

4.4 Water Re-circulation and Skimming Systems

The glass bottom of the tank has two holes at either end to allow for the connection of PVC drain and fill pipes. At one of the ends of the tank, three skimmers are set to remove the contaminants that tend to accumulate at the free surface of the water and also control the water height. Part of the water collected by the skimmers can be sent to a drain while a centrifugal pump sends the rest of the water to a diatomaceous earth filter and back to the opposite end of the tank.

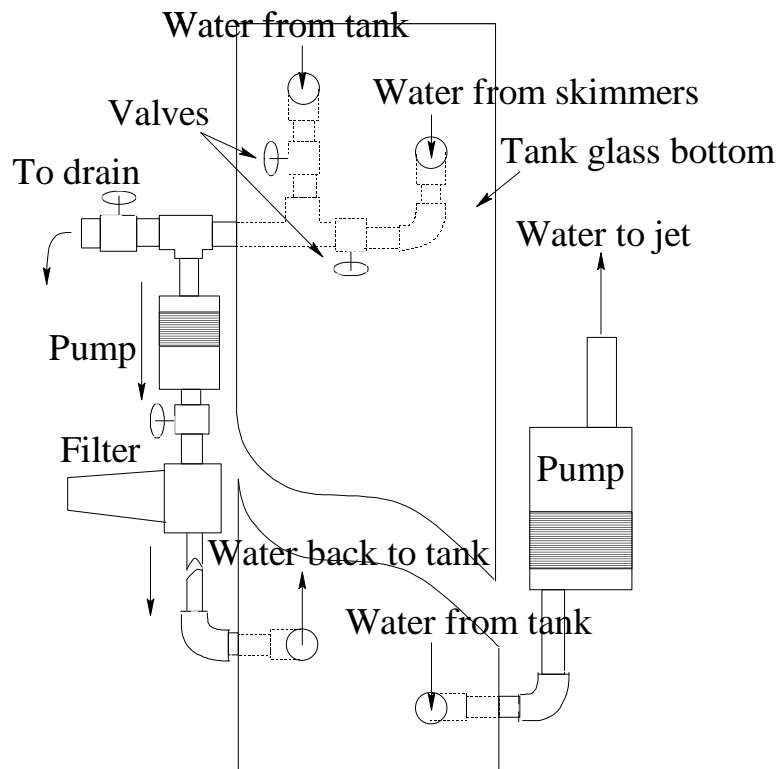


Figure 4.8: The figure shows a schematic of the piping system looking at the tank bottom from the top

A set of valves control the flowrate of the pump (and thus the skimming rate) and the amount of water sent to the drain. Simultaneously, the tank can also be filled with fresh water. The tank water was treated with 3 *p.p.m.* of chlorine to avoid the growth of bacteria.



Figure 4.9: Picture of the three water skimmers at one end of the new facility. The skimmers remove the contaminants from the water free surface and send them to a filter

4.5 Jet Nozzle Design and Construction

4.5.1 General Description and Dimensioning

The planar jet is created from a nozzle fed by a centrifugal pump. The jet nozzle is secured to the carriage by an aluminum structure, while the pump rests on the floor by the water tank. The pump removes water from the tank through a port located on the bottom of one end of the tank and sends it to the jet nozzle through two long flexible hoses. The pump removes water from the tank through a port located on the bottom of one end of the tank and sends it to the jet nozzle through two long flexible hoses.

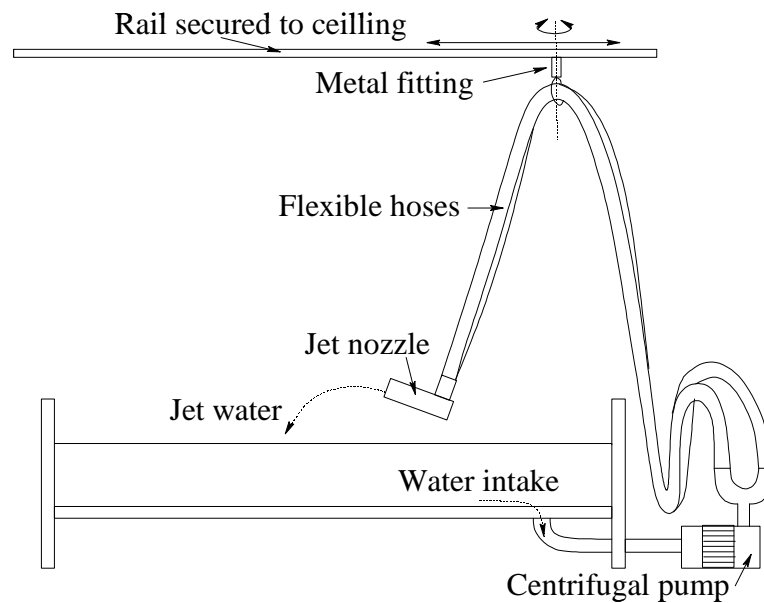


Figure 4.10: The jet is created from tank water and is fed by a centrifugal pump

A metal fitting that hangs from a rail secured to the ceiling supports the weight of the hoses. The fitting can rotate about a vertical axis and translate freely along the length of the rail that is placed parallel to the tank. This set-up allows the hose ends connected to the two nozzle inlets to follow the carriage without stressing the nozzle inlet connections. The jet nozzle itself is essentially a 14x4x18 inch PVC rectangular box. The water enters through the two water inlets and flows inside the nozzle through four turbulence-reduction elements: an open-cell foam sheet, two stainless steel screens and a plastic honeycomb specifically dimensioned to minimize the jet turbulence levels. Downstream from these elements, the water flows through a smoothly contoured contraction and finally exits the nozzle through a variable width, 18" long slot. The jet exit thickness can be varied from 0 to 0.5 inches. By changing the jet nozzle inclination, the jet nozzle height with respect to the free surface, the jet exit thickness and the pump flowrate, a variety of jet impact velocities (V_j), jet impact angles (α_j) and jet impact thicknesses (T_j) can be achieved.

4.5.2 Turbulence Reduction Systems

The turbulence reduction problem for the water flowing inside the nozzle is physically similar to the turbulence reduction problem for air inside a wind tunnel. In both cases, screens and honeycombs are used to break-up the turbulence and both problems take place at comparable Reynolds numbers. Thus, the design of the turbulence reduction elements of the jet nozzle was determined according to the broad experience on wind tunnel design gathered in the literature.

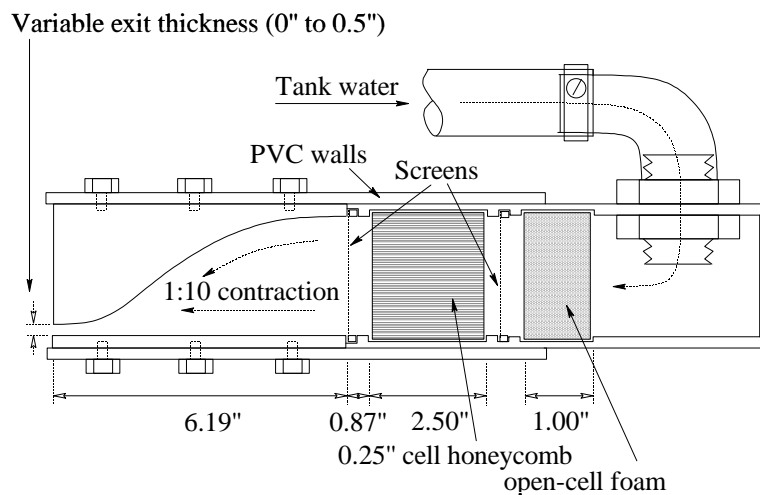


Figure 4.11: Cut of the planar jet nozzle. The nozzle is 18 inch wide (into the paper)

J. Scheiman [31] proved that the most efficient configuration for turbulence reduction was one honeycomb followed by one screen. According to this, 1/4 inch hexagon-cell plastic honeycomb was utilized for the design in combination with one screen. The length of the honeycomb in the streamwise direction was

2.5 inches according to Loehrke [29] that recommends a honeycomb length of 10 times the size of the cells.

The utilized screen was a 16x16 mesh stainless steel wire cloth (wire diameter of 0.009 inches) which had a 71% open area. The ratio of projected open area to total area of the screen should be larger than 57% to avoid instabilities downstream from the screen (Pope [32]). Another important parameter is the spacing between the screen and the honeycomb, which should be less than five times the honeycomb cell-size (Loehrke [29]). This parameter was set to 0.25 inches for this design. Additionally, far upstream from the turbulence reduction elements and in front of the water inlets, a 1 inch thick open-cell foam sheet and a second screen were placed to produce a pressure drop to uniformly distribute the flow across the plenum cross-section. The screens were spot-welded to rectangular stainless steel frames. The frames, the honeycomb and the foam sheet fit into grooves machined on the inner side of the nozzle walls.

4.5.3 Nozzle Contraction Design

A contoured hydrodynamic contraction was placed downstream from the turbulence reduction systems that were described in section 4.5.2. It was decided to design half of a contraction (Figure 4.12) as opposed to a symmetric contraction so that shallower jet impact angles could be achieved by taking the nozzle exit closer to the water free surface. The primary goal of the hydrodynamic con-

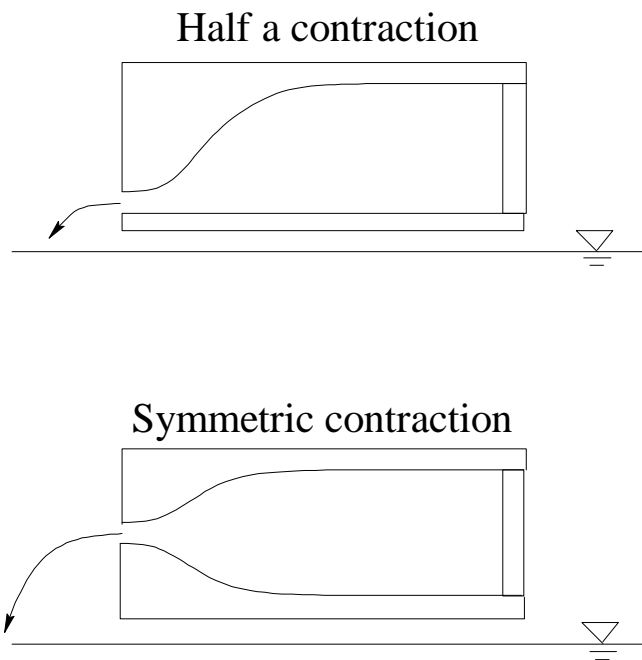


Figure 4.12: A planar jet nozzle with half a contraction (top) reaches lower jet free-fall distances that a jet nozzle with a symmetric contraction (bottom)

traction is to drive the flow to the nozzle exit slot while reducing the turbulence levels present in the water. In this type of nozzle, it is desirable to have large contraction ratios since those help stretch the existing vortical structures thus producing a faster dissipation of the turbulence. In this design, the contraction

ratio was limited to 10 in order to avoid an excessive weight of the final nozzle. Additionally, in order to have a uniform velocity profile of the jet at the nozzle exit, the design had to prevent an excessive growth of the boundary layer on the wall of the contraction and this was achieved by preventing the flow from generating negative pressure gradients and by minimizing the contour streamwise length. All these ideas were integrated in a methodology which was used to design the nozzle contraction contour and that is described in the following.

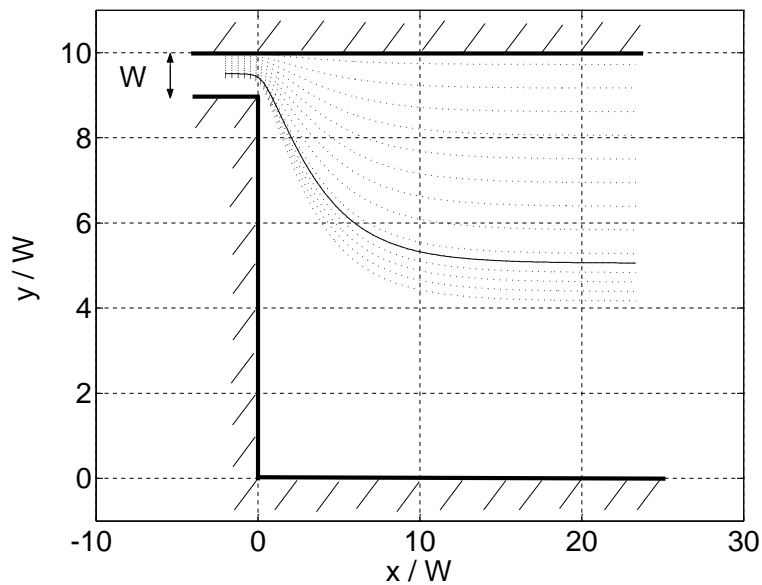


Figure 4.13: Streamlines of a 10 to 1 contraction in potential flow

Figure 4.13 shows a set of streamlines calculated with potential flow for a two-dimensional stream going through a 10 to 1 contraction (flow moving from right to left) where the flow is bounded by a flat wall at the top and a step-like wall at the bottom. The flow over the contraction was calculated using the Schwarz-Christoffel conformal transformation [35] given in equation 4.1. Through this

transformation, the physical space (plane ζ) is transferred into a much simpler problem of a sink placed at the boundary of a semi-infinite plane (plane z) which has a known solution. The mathematical expression of the transformation is:

$$z = \frac{h}{\pi} \left\{ I_{11}(s) - \frac{k}{h} I_{11} \left(\left[\frac{k}{h} \right] s \right) - \left(1 - \frac{k}{h} \right) I_{11}(0) \right\} \quad (4.1)$$

where

$$I_{11}(s) = \ln \left(\frac{1 + s^2}{1 - s^2} \right) \quad (4.2)$$

being

$$s = \left(\frac{\zeta - e}{\zeta - 1} \right)^{1/2} \quad (4.3)$$

and

$$e = \left(\frac{h}{k} \right)^2 \quad (4.4)$$

For a 10 to 1 contraction ratio, $h = 10$ and $k = 1$.

The pressure distribution over any arbitrary curve of this family of streamlines can be calculated with potential flow theory by using the former conformal transformation. The magnitude of the velocity of the particles (u_p) can be computed using [35]

$$\frac{u_p}{U_\infty} = s \quad (4.5)$$

where U_∞ is the velocity of the particles far upstream. The distribution of coefficient of pressure C_p along the streamlines shown in Figure 4.14 was calculated using

$$C_p = \frac{P_p - P_\infty}{\frac{1}{2}\rho U_\infty^2} = 1 - \left(\frac{u_p}{U_\infty}\right)^2 = 1 - s^2 \quad (4.6)$$

where P_∞ is the flow pressure far upstream.

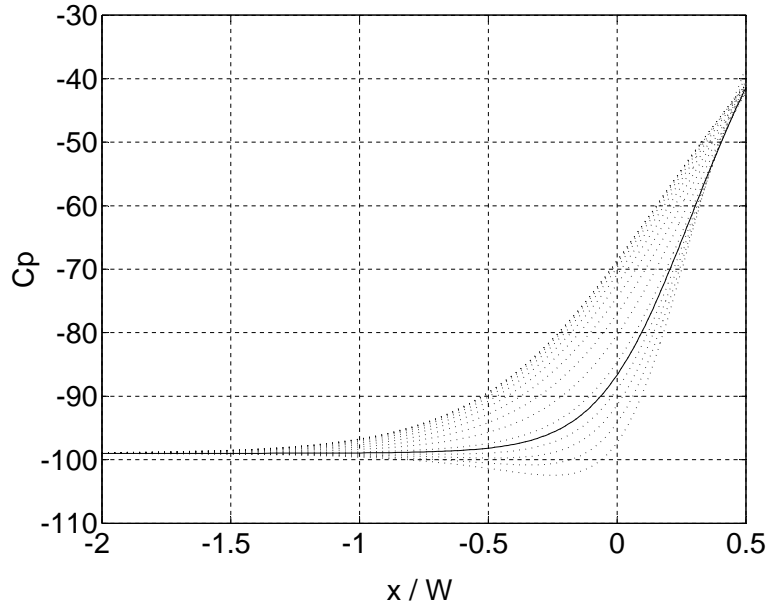


Figure 4.14: Pressure distribution on the streamlines of a 10 to 1 contraction in potential flow

By definition, the water flow cannot cross the streamlines and therefore, the flow bounded by the top wall and any of the streamlines sees a contraction ratio of 10 to 1. This property, together with the fact that this family of streamlines has a known pressure distribution, allows one to select a streamline for the nozzle contour shape.

For the same x location, the curves with the highest C_p correspond to the streamlines that are closer to the upper boundary in Figure 4.13. The particles

that follow the streamlines closer to the upper boundary always see a favourable pressure gradient as they move to the left, while the particles that follow the lower streamlines initially see an adverse pressure gradient (Figure 4.15). In principle, any of the streamlines with a favorable pressure gradient might be a good candidate to be the final shape of the contour design.

The streamline marked with a solid line in Figure 4.13 is of particular interest since it has a favorable pressure gradient and has the shortest streamwise length when properly scaled to the actual exit slot thickness. This is advantageous to minimize the boundary layer growth and this streamline was taken as the starting point for the contour design.

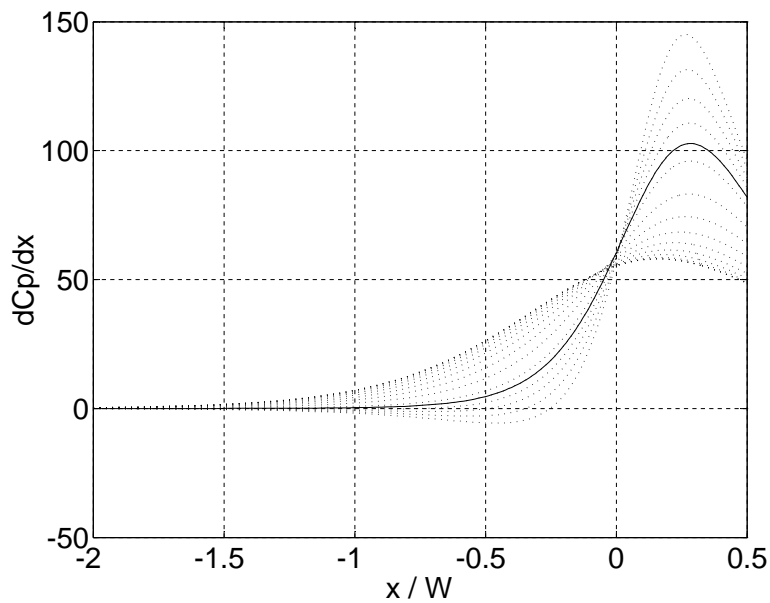


Figure 4.15: Pressure gradient distribution on the streamlines of a 10 to 1 contraction in potential flow

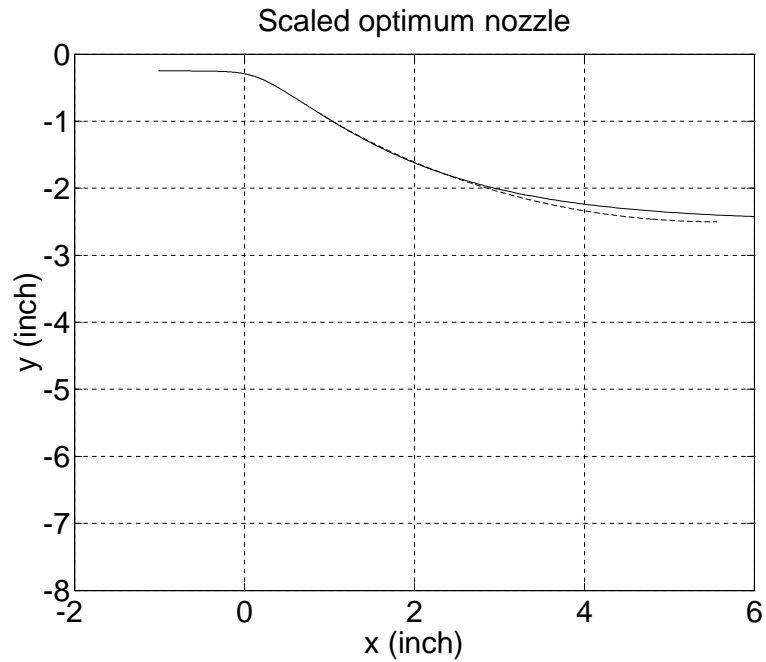


Figure 4.16: Selected streamline due to its favorable pressure gradient

The final contour design was generated using the selected streamline between $x/W = -2$ and $x/W = 4$ combined with a segment of a circle of the same curvature of the streamline at $x/W = 4$, placed tangent to the streamline at this location. The addition of the circular segment shortens the final streamwise length of the contour while keeping a constant curvature distribution. Figure 4.17 shows the distribution of curvatures for the family of streamlines, where it can be seen that at $x/W = 4$, the curvature of the selected streamline does not have a strong gradient.

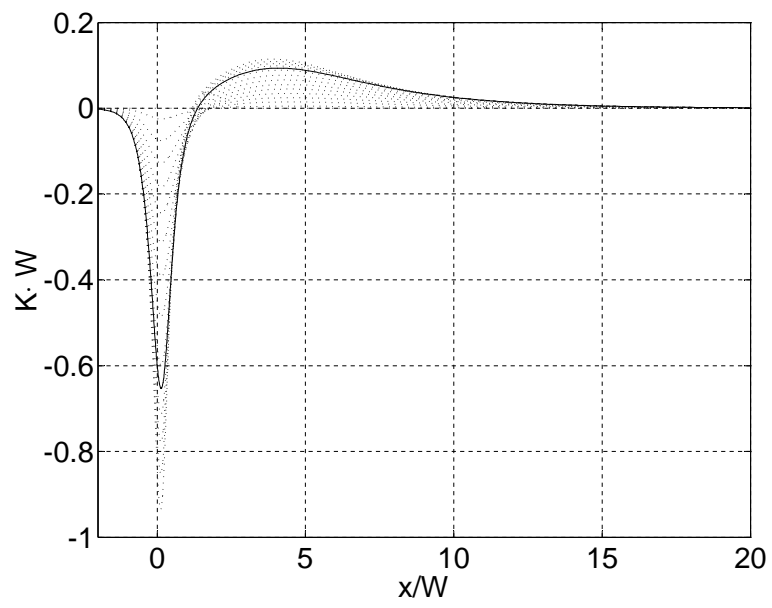


Figure 4.17: Curvature distribution on the selected streamline

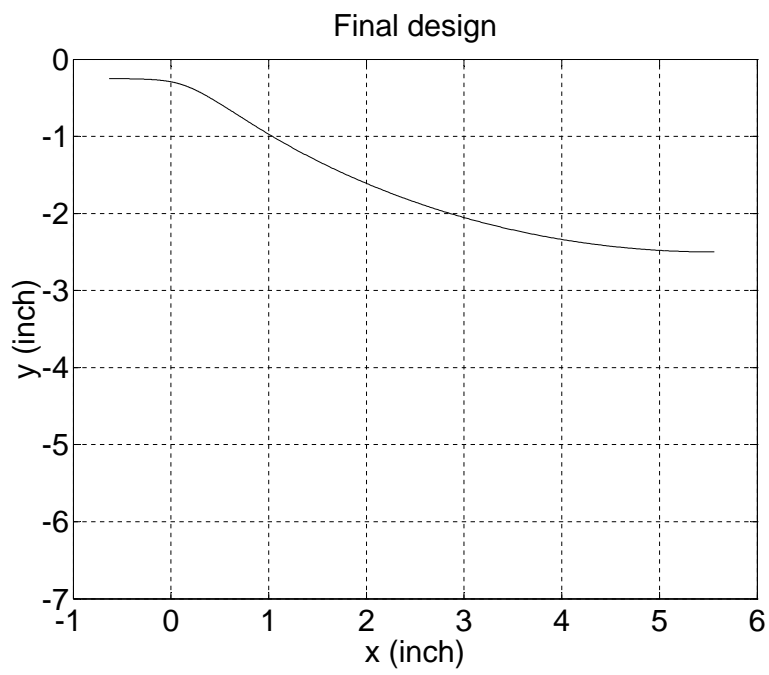


Figure 4.18: Final contraction design

4.6 Jet Cutter and Free Surface Disturbances

One of the biggest challenges found to set-up the planar jet experiment was to create a suddenly starting jet with a reasonably clean leading edge. It was not possible to create a controlled, impulsive, starting transient by just turning on the centrifugal pump due to two primary reasons: 1) the relatively large amount of fluid mass contained in the supply lines and nozzle plenum greatly increases the time constant for accelerating the flow, and 2) air trapped in the nozzle can only be flushed from the system when it is operating at full speed. It takes some time for the flow to achieve a steady controlled state and drag all the entrapped air out of the system.

Therefore, in order to create the transient impact of the jet, a steel plate was positioned in front of the running jet at a fixed distance with respect to it. The steel plate can rotate around a horizontal axis between two different positions. In the initial position, the plate is almost perpendicular to the jet and deflects the jet trajectory (see Figure 4.19).

In the final position, the plate is parallel to the jet and is located under the parabolic trajectory of the jet. Just prior to the moment of the desired impact, the plate rotates from the initial position to the final position driven by a pneumatic system. The fast rotation of the plate produces a clean cut of the jet and frees the path for the jet to continue a parabolic trajectory. The jet finally plunges on the water free surface (Figure 4.20).

The jet cutter system included a steel plate, pulleys, two pneumatic actuators, a solenoidal valve and a compressed air tank that could be refilled with an electric compressor to keep the actuation pressure approximately constant throughout all

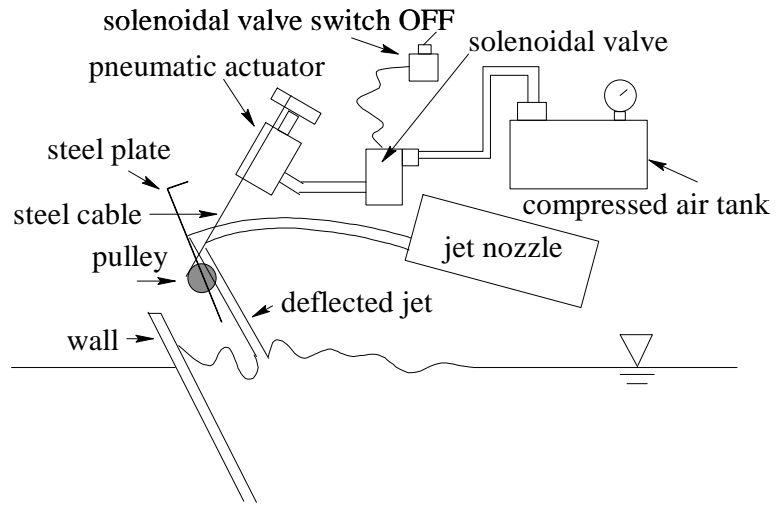


Figure 4.19: Jet cutter system. Plate deflecting the jet

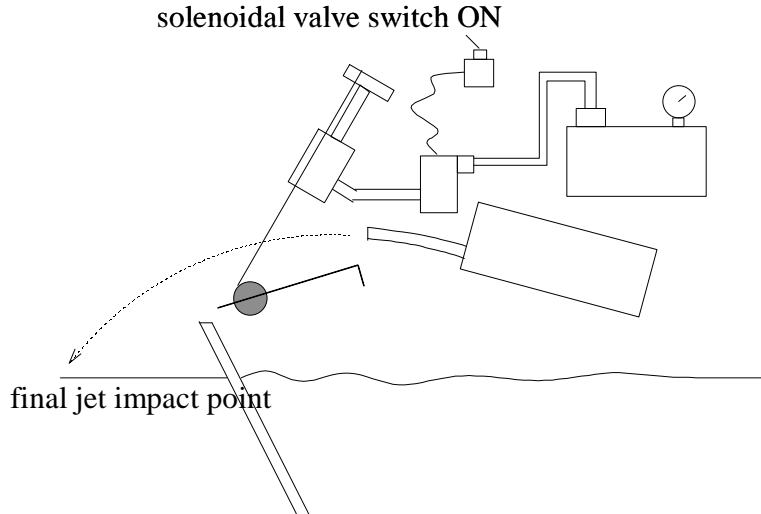


Figure 4.20: Jet cutter system right after the jet cut

the experiments. All the elements of the jet cutter system followed the jet nozzle during its horizontal translation and the jet cut was only produced once the carriage had achieved a steady horizontal translating velocity.

In order to keep an undisturbed free surface for the jet to impact, a PVC wall was placed inside the tank and fixed with respect to it to isolate the perturbations produced by the deflected jet on the water free surface (Figure 4.19).

Also, to isolate the jet nozzle from vibrations created by the jet cutter system, the latter was mounted onto a separate carriage connected to the nozzle carriage with strings. In addition, the jet nozzle was supported by four low stiffness elastomeric rubber mounts to help isolate the vibrations.

4.7 Removal of Jet End Effects

Due to the finite width of the falling water mass, a strong three dimensional behaviour could be observed near the ends of the plunging jet.

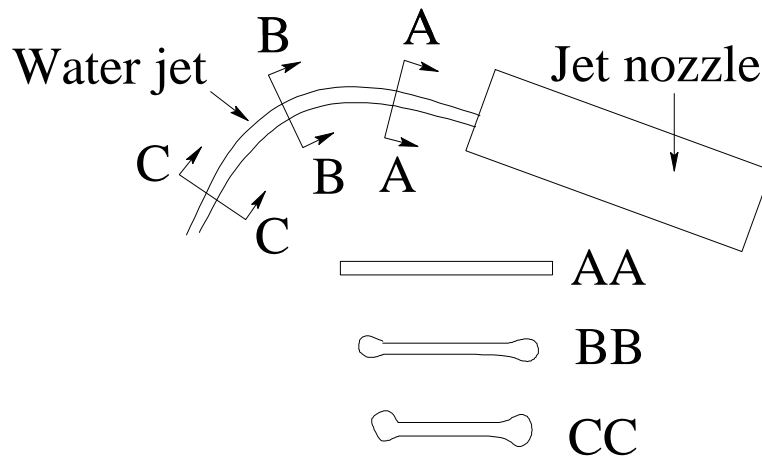


Figure 4.21: Sections of the water jet as it falls

These effects are enhanced by the fact that surface tension thickens the ends of the water sheet as the jet falls (see Figure 4.21). Since the goal of this study is to understand the two-dimensional plunging jet problem, it was therefore decided to introduce a new element in the experimental set-up to minimize the three-dimensional effects induced by the falling jet. The role of this new device is to remove the ends of the falling water mass while providing two vertical transparent boundaries to the jet experiment: two plexiglass vertical walls. The plexiglass walls are semi-immersed into the tank water so the experiment has a two-dimensional character all throughout the jet impact process.

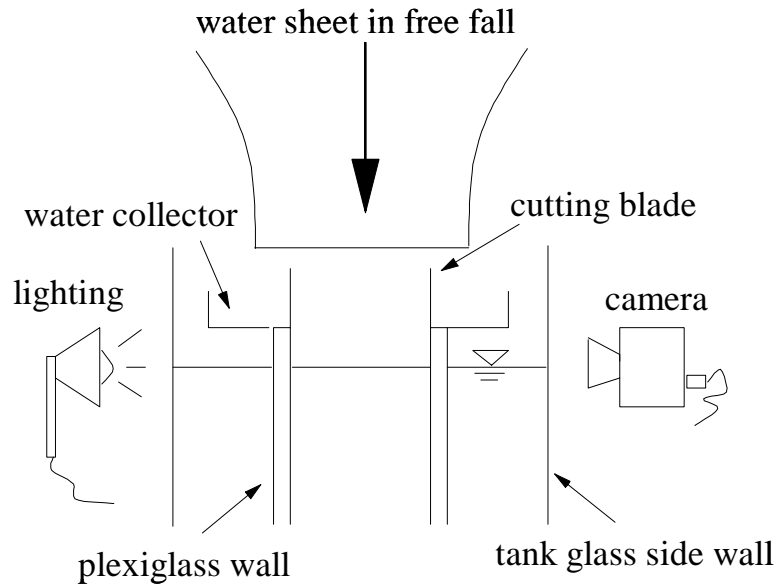


Figure 4.22: Front view of the jet ends cutter device

Figure 4.22 shows a front view of the tank and the jet edge deflector device. The device consists of two long cutting blades, two long water collectors and the above-mentioned acrylic walls that are supported by a structure resting on the tank bottom. Figure 4.23, shows how the jet edges are removed by the cutting blades and how the excess water is driven away from the experiment by the water collectors. The center section of the jet remains attached to the plexiglass walls as it travels downwards, before and after the jet impact with the tank water free surface. Figure 4.24 shows a lateral view of the set-up. Note that the viscous frictional effects near the plexiglass walls are negligible due to the large Reynolds numbers (Re) associated with the experiment. To compute this Reynolds number let the velocity scale be that of the jet, about 3 m/s. The appropriate length scale for the Reynolds number is the typical distance a water particle travels over

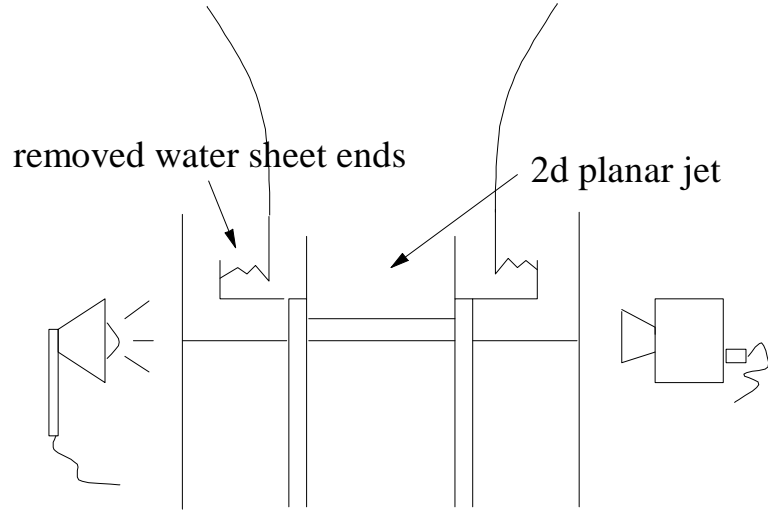


Figure 4.23: The jet edge deflector device removes the ends of the jet and provides two transparent vertical boundaries for the two-dimensional plunging jet problem

the plexiglas surface and involves the jet thickness, the distance to the bottom of the cavity at any time and the translational velocity of the carriage. Let us assume that this length (x) is about 10 cm. Then the Reynolds number is about 300,000 and we can assume that the boundary layer is laminar. The thickness of this laminar boundary layer (T_{bl}) will grow in proportion to x/\sqrt{Re} and given the above estimates of Re and x we find

$$\frac{T_{bl}}{T_j} \approx \frac{x}{T_j} \frac{1}{\sqrt{Re}} = 0.018 \quad (4.7)$$

where we have used $T_j \approx 1$ cm. To ensure the two-dimensionality of the experiment, the distance between plates (13 cm) was set to be much larger than T_{bl} and the jet thickness.

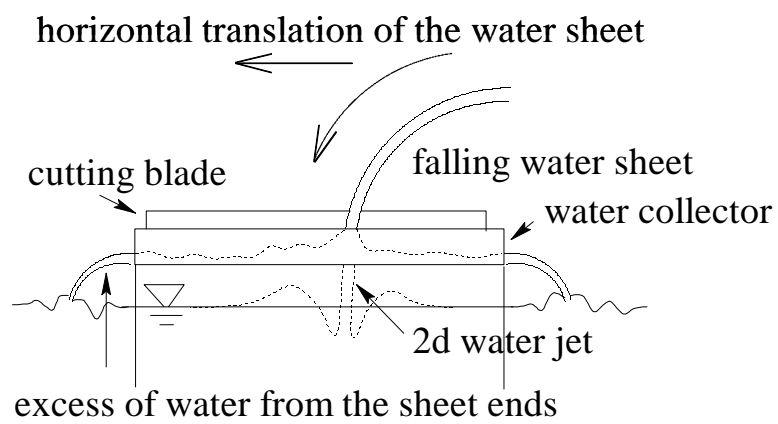


Figure 4.24: Lateral view of the jet edge deflector device. The jet has already plunged on the tank water free surface

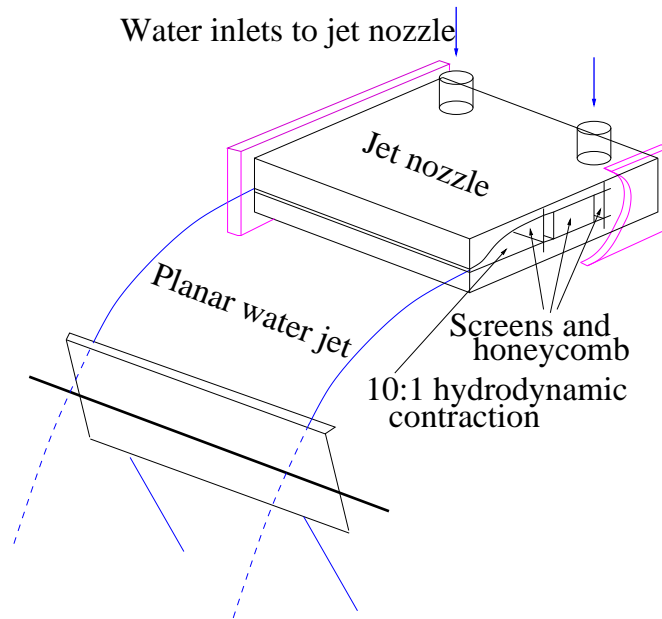


Figure 4.25: Perspective of the jet deflector in its initial position before the jet has been cut

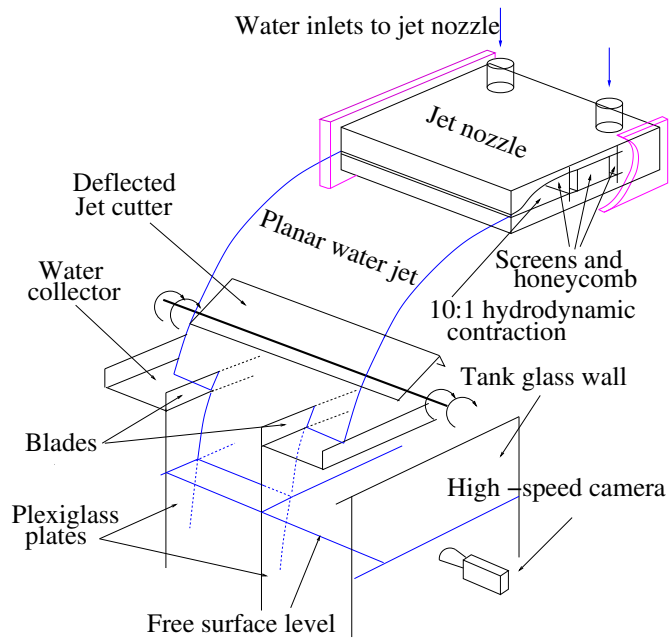


Figure 4.26: Perspective of the jet edge deflector and the jet cutter in its final position after the jet has been cut

Chapter 5

Visualization Experiments for the Impacting Planar Jet

In order to visualize the transient impact of an inclined, horizontally translating planar jet, a set of high-speed visualization experiments were performed for a variety of jet inclination angles, jet thicknesses, jet impact velocities and jet translating velocities. The goal of these visualization experiments was to identify the general features of the flow and observe how they are affected by the horizontal translation of the jet. Special attention was paid to the underwater jet behavior and the first stages of the air entrainment.

5.1 Experimental Set-Up

5.1.1 High Speed Imaging

A Vision Research, Phantom V4.0 high-speed digital CMOS camera was used to visualize the jet impact at 1000 fps with a resolution of 512x512 pixels. The

camera was set to look through the side tank walls, with the jet and the receiving pool back-lit by a continuous light source positioned on the opposite side of the tank, as shown in Figure 4.19. Both camera and lighting were fixed to the main carriage using aluminium beams as described in Section 4.3 to ensure they track the motion of the water jet during its horizontal translation. The camera was controlled by a laptop computer that was also attached to the carriage.

A thin translucent plastic sheet was fixed to the tank wall on the side of the light source, which acted as a diffuser to provide a more uniform lighting.

The camera had a simultaneous view both above and below the tank mean water line to allow for the determination of the jet properties prior to impact, in addition to tracking the evolution of the subsurface cavity shape. Finally, for each run, images of a calibrated ruler were taken to allow for physical scaling of the different jet features measured in the movies.

5.1.2 Measurements of the Jet Impact Conditions and Nomenclature

The results shown in the following sections are given as a function of the characteristics of the planar jet at the time of impact with the free surface. The defining characteristics of the jet are the jet impact velocity (V_j), the jet impact thickness (T_j), the jet impact angle with respect to the vertical (θ_j) and the jet horizontal translating velocity (V_t), as shown in Figure 5.1. The values for V_j , T_j and θ_j are given in a reference frame fixed to the jet carriage so they are independent of the jet translating velocity, and the three values define one jet condition. In the following sections, for each jet condition, results are shown for different jet translating velocities V_t .

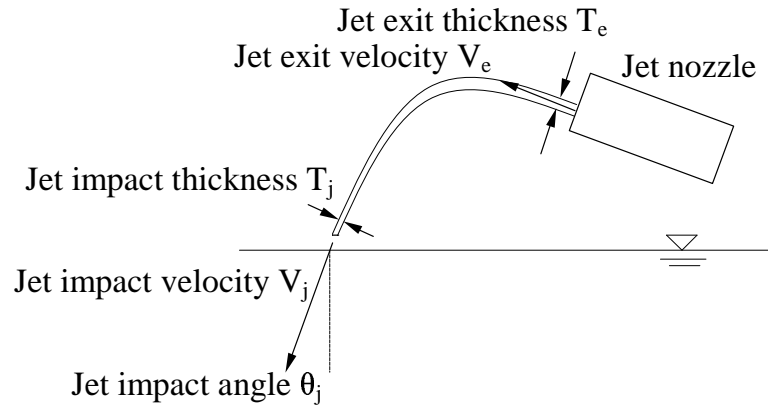


Figure 5.1: Jet nomenclature

Exp Cond	# Rep	Mean			St Dev			Fr_j	Re_j	We_j
		V_j (<i>m/s</i>)	T_j (<i>cm</i>)	θ_j (<i>deg</i>)	V_j (<i>m/s</i>)	T_j (<i>cm</i>)	θ_j (<i>deg</i>)			
I	3	2.59	0.38	32.5	0.05	0.02	1.9	13.6	8782	3.6
II	5	3.48	0.28	45.2	0.11	0.02	1.1	21.0	8562	4.6
III	3	3.04	0.36	17.4	0.01	0.01	1.6	16.2	9537	4.5
IV	2	3.32	0.29	7.1	0.07	0.02	0.2	19.7	8460	4.4
V	3	2.12	0.35	29.5	0.09	0.02	1.2	11.4	6520	2.1
VI	3	2.22	0.50	23.8	0.07	0.04	1.3	10.0	9754	3.4

Table 5.1: Planar jet impact experimental conditions

In order to determine the characteristics of the jet at the impact, a set of above-water high-speed movies were taken at 1000 fps for non-translating jets. The set-up for the camera and the lighting was similar to the set-up shown in Figure 4.19, where the lateral deflectors to remove the edges of the jet are removed to allow for unobstructed visualization prior to impact. For each movie, five consecutive frames of the above water jet spaced in 2 *ms* intervals were selected such that the last frame of each sequence was coincident with the jet impact on the free surface. Therefore, each sequence provided information on the temporal evolution of the jet leading edge position immediately prior to jet impact. Adobe Photoshop 7.0 was utilized to manipulate consecutive frames of the sequence by manually shifting the images relative to each other until the jet leading edges of the two frames were matched. The resulting relative displacement between frames gave a measurement of the horizontal and vertical displacements of the jet leading edge during the final 10 *ms* prior to impact (5 frames, 2 *ms* interval). The displacements in the two directions gave values of the magnitude of the jet velocity (V_j) and the direction (θ_j). The calibration images described in section 5.1.1 were used to scale the results from image coordinates (pixels) into physical magnitudes. The described process was repeated for each sequence and the results fitted by the least squares method giving values for V_j and θ_j for each test. Several repetitions of the whole process were performed for each jet condition to obtain statistical information on the mean and standard deviation for these two quantities.

The jet thickness, T_j , at the center section of the jet span was difficult to measure directly on the movies because this region was obscured by the thickened edge of the jet due to surface tension effects (as described in section 4.7). There-

fore, the jet thickness T_j was determined indirectly by measuring the flow-rate for each jet condition Q and applying conservation of mass.

$$T_j = \frac{Q}{V_j L_s} \quad (5.1)$$

where L_s is the span of the nozzle opening.

To get statistical information on the jet flowrate for each condition, ten measurements of the jet flowrate were performed on stationary jets. This was completed by collecting the water issuing from the jet in a calibrated bucket during a time interval that was measured with a stop-watch (typical duration of approximately 1.5 seconds). Propagation of errors was used to determine the uncertainty of the indirect measurements of T_j based on the uncertainties associated with Q and V_j

$$\Delta T_j = \frac{1}{L_s} \left\{ \frac{1}{V_j} \Delta Q + \frac{Q}{V_j^2} \Delta V_j \right\} \quad (5.2)$$

Experiments were performed for six different jet conditions and five different translation velocities with values of V_j ranging between 2.12 and 3.48 m/s , T_j between 0.29 and 0.50 cm , θ_j between 7.1 and 45.2 degrees and V_t between 0.0 and 0.6 m/s . See Table 5.1 for details.

Lastly, a final observation should be added to complete the characterization the jet impact conditions. The jet leading edge was observed to be rounded and thickened due to surface tension effects, taking a quasi-cylindrical shape. The approximate thickness of this cylinder T_b , as shown in Figure 5.2, was measured in the above water high-speed movies just before the jet impact. The measurements are summarized in Table 5.2.

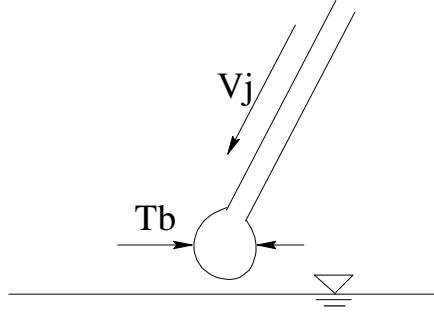


Figure 5.2: Buldge at jet leading edge

Exp. Cond.	T_b/T_j (Mean)	T_b/T_j (St Dev)
I	7.97	0.18
II	9.66	0.66
III	9.42	0.29
IV	6.42	0.47
V	7.54	1.11
VI	7.10	0.26

Table 5.2: T_b values measured from the above-water movies

5.2 General Description of the Flow

In all of the impacts observed for the current range of parametric space, several typical features and characteristic events are observed. In the following section, selected frames of the jet high-speed movies (Figures 5.3, 5.4, 5.5 and 5.6) are shown to illustrate this sequence of characteristic events.

The figures correspond to jet condition VI at $V_t = 0.15 \text{ m/s}$ for 40, 80, 121 and 160 *ms* respectively after the jet impact. In the figures, the jet is moving from right to left and the camera is translating with the jet.

In all the movies, the jet was observed to first approach the undisturbed water free surface followed by an impact that produced two splashes and two air cavities, one at either side of the jet impact site (Figure 5.3). During these tests, the acrylic sidewalls and edge cutting device were in place, allowing a clear view of the jet and cavities both above and below the undisturbed free surface.

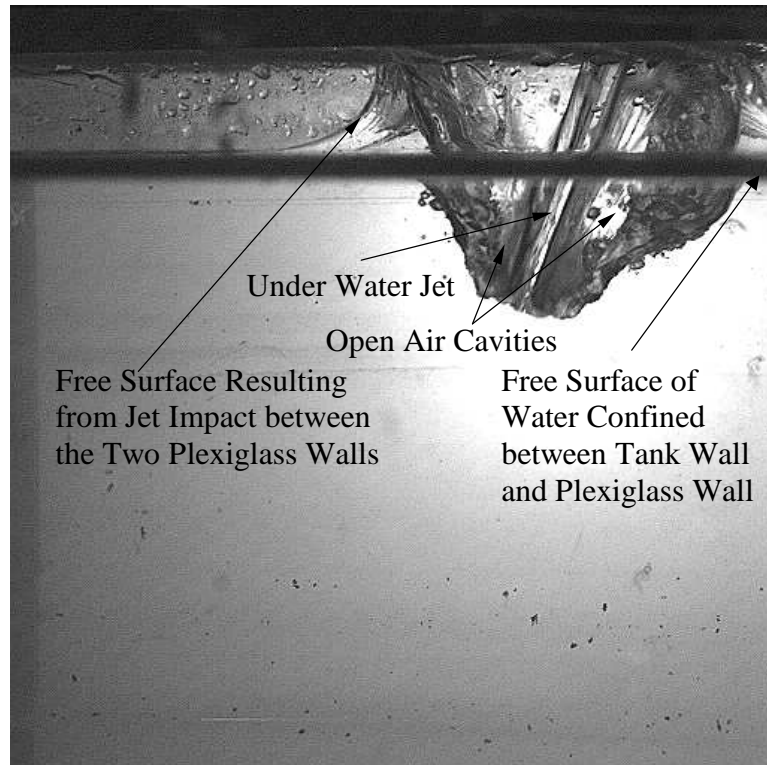


Figure 5.3: Jet condition VI, $V_t = 0.15 \text{ m/s}$, $t = 40 \text{ ms}$ after the jet impact. Note that the black strip at the top is the opaque steel cutting blade.

Following the initial impact, the jet penetrates the water at an angle qualitatively similar to the jet impact angle, dragging the air cavities into the water. More specific details of this characteristic will be discussed in Chapter 7.

During the early stage of development (as shown in Figure 5.4), the cavity interface is observed to gradually move away from the centerline of the jet and takes a characteristic inverted bell-like shape with two curvature sign changes at either side.

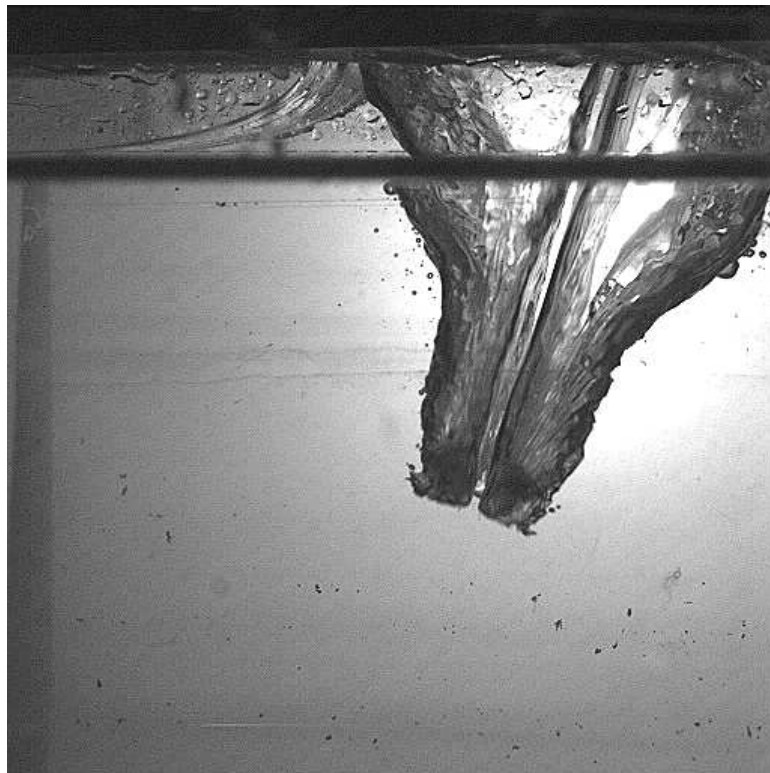


Figure 5.4: Jet condition VI, $V_t = 0.15 \text{ m/s}$, $t = 80 \text{ ms}$ after the jet impact

After a sufficient development time, the component of the velocity of the crater walls perpendicular to the jet stops, reverses and then starts moving towards the jet. Eventually, the crater walls touch the underwater jet in one point producing a pinch-off (Figure 5.5). Typically, the pinch-off occurs in the upstream side of the jet.

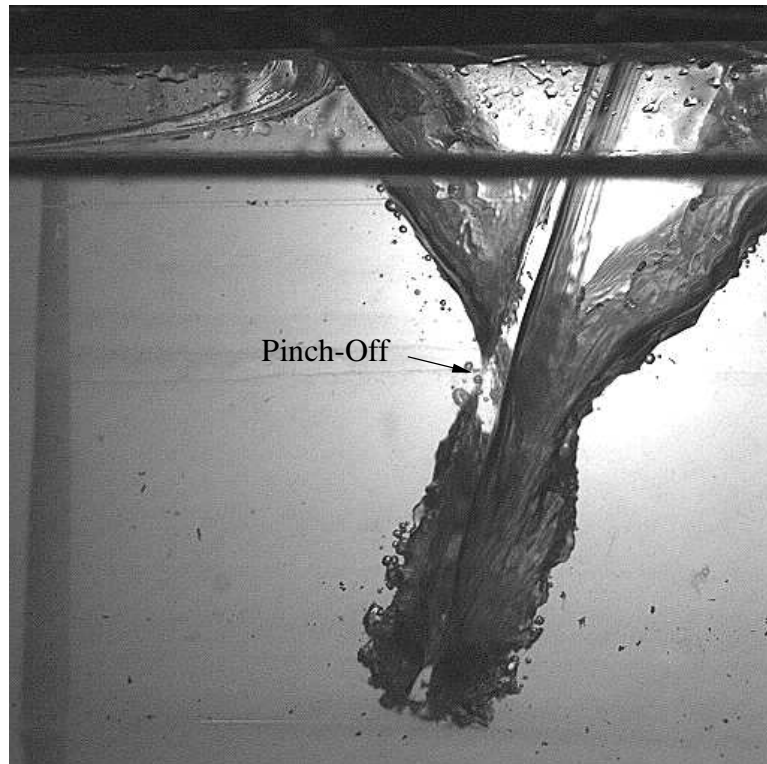


Figure 5.5: Jet condition VI, $V_t = 0.15 \text{ m/s}$, $t = 121 \text{ ms}$ after the jet impact

The subsequent collapse of the crater produces a cloud of bubbles that is entrained downstream in the form of a turbulent multiphase jet that eventually rises under the influence of buoyancy (Figure 5.6).

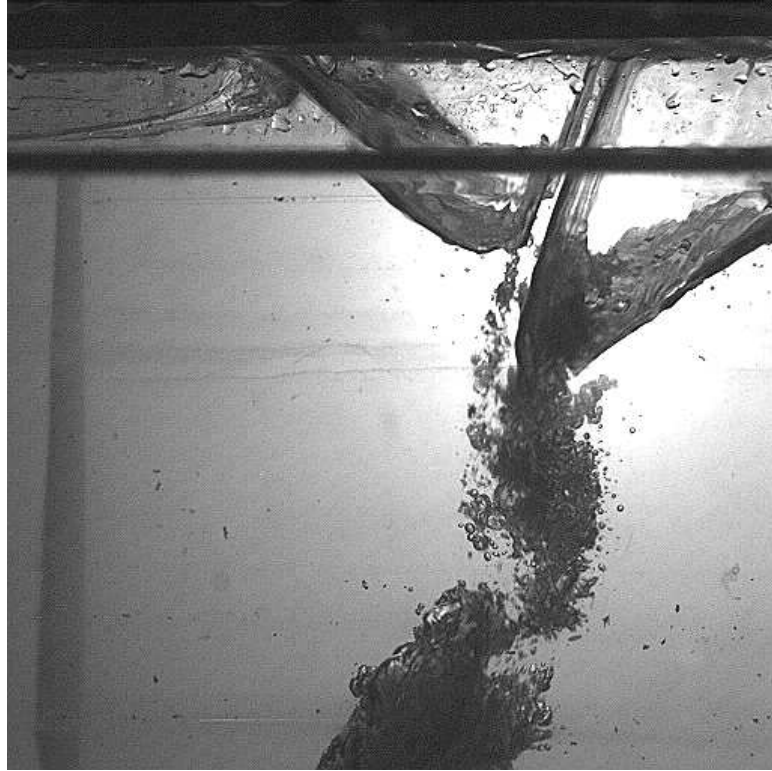


Figure 5.6: Jet condition VI, $V_t = 0.15 \text{ m/s}$, $t = 160 \text{ ms}$ after the jet impact

The horizontal translating velocity of the jet has a remarkable influence on the underwater flowfield. To illustrate this influence, a few selected frames of the high-speed movies for condition V at different translating velocities are shown.

The photographs of Figures 5.7 and 5.8 were taken for jets translating at 0.00, 0.15, 0.30, 0.45 and 0.60 m/s respectively, and show the underwater flowfield at one third of the pinch-off time (note that the time to pinch-off conditions (t_{po}) is not the same in each case). At these early stages of the crater formation, the influence of the jet horizontal translation velocity is not yet apparent.

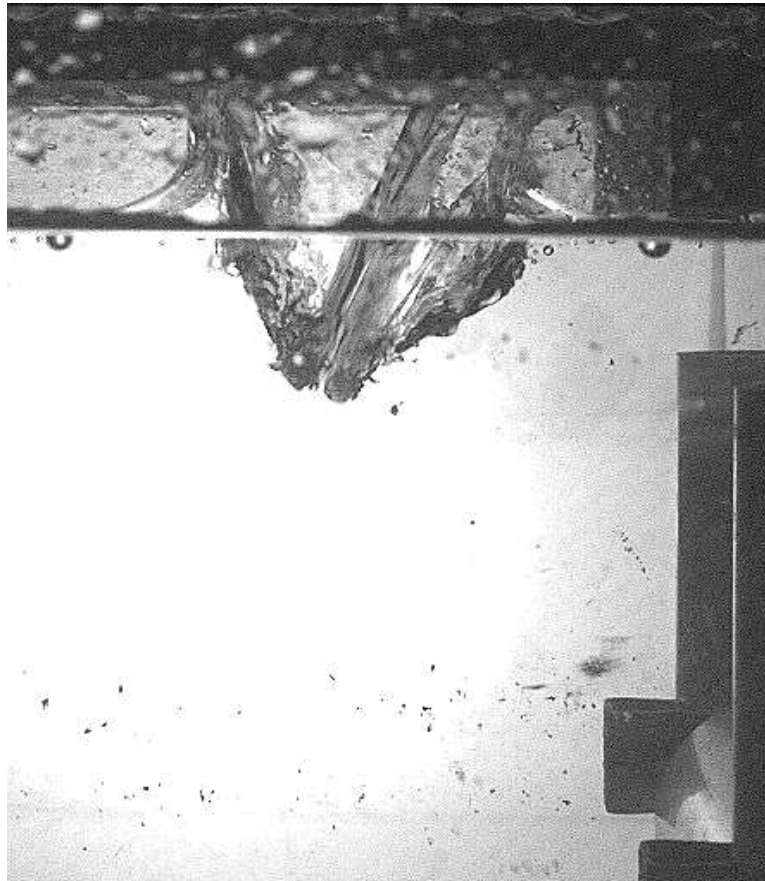


Figure 5.7: Jet condition V, $V_t = 0.00 m/s$, $t/t_{po} = 1/3$ ($t = 39 ms$)

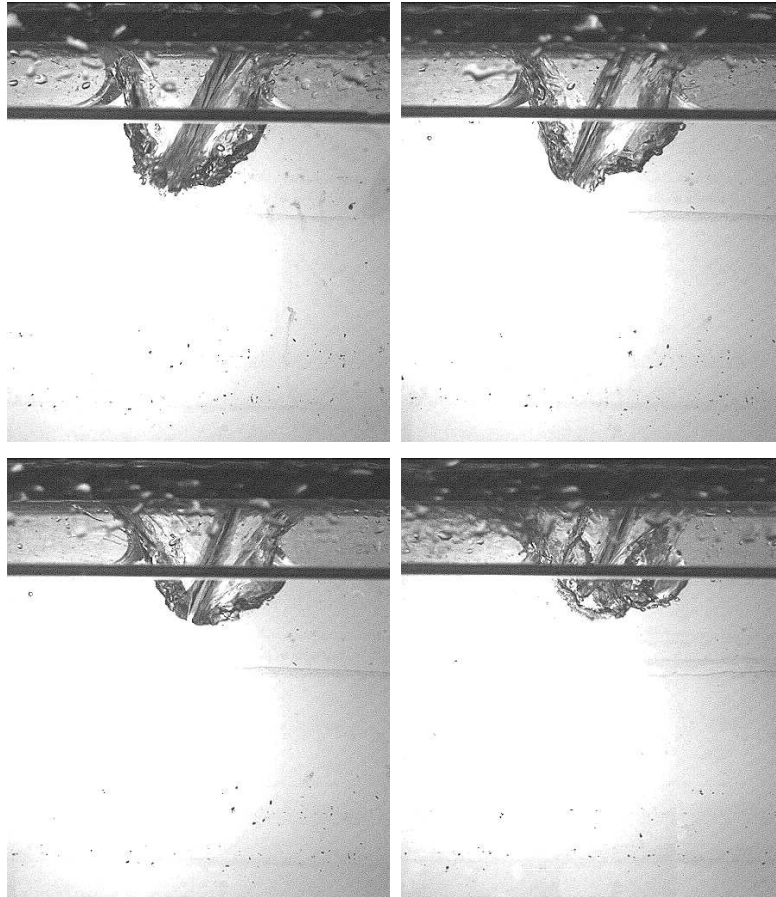


Figure 5.8: Jet condition V, $t/t_{po} = 1/3$: $t = 35 \text{ ms}$, $V_t = 0.15 \text{ m/s}$ (top left); $t = 32 \text{ ms}$, $V_t = 0.30 \text{ m/s}$, (top right); $t = 24 \text{ ms}$, $V_t = 0.45 \text{ m/s}$ (bottom left); $t = 19 \text{ ms}$, $V_t = 0.60 \text{ m/s}$ (bottom right)

For the same set of translating velocities, the photographs of Figures 5.9 and 5.10 show the underwater flow field at two thirds of the pinch-off time. At this point of the crater formation, it can be observed that the jet translation induces a severe asymmetry between the two air craters that form at either side of the jet. For the faster jets, the downstream crater becomes larger when compared with the upstream one. Also, its boundary looks more inclined while the boundary of the upstream crater becomes more vertical.

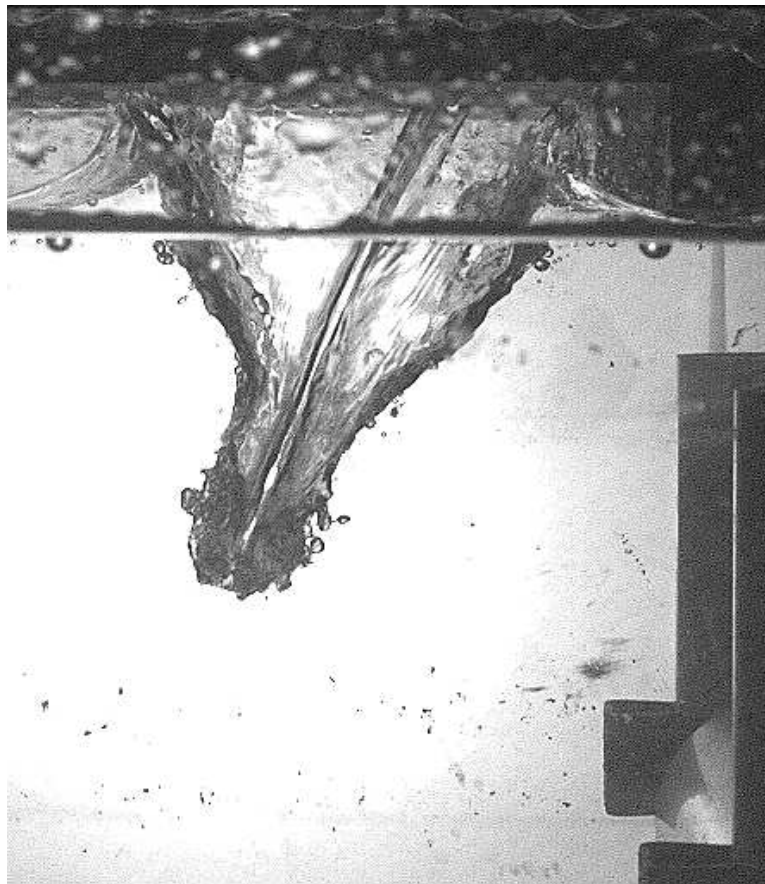


Figure 5.9: Jet condition V, $V_t = 0.00 \text{ m/s}$, $t/t_{po} = 2/3$ ($t = 77 \text{ ms}$)

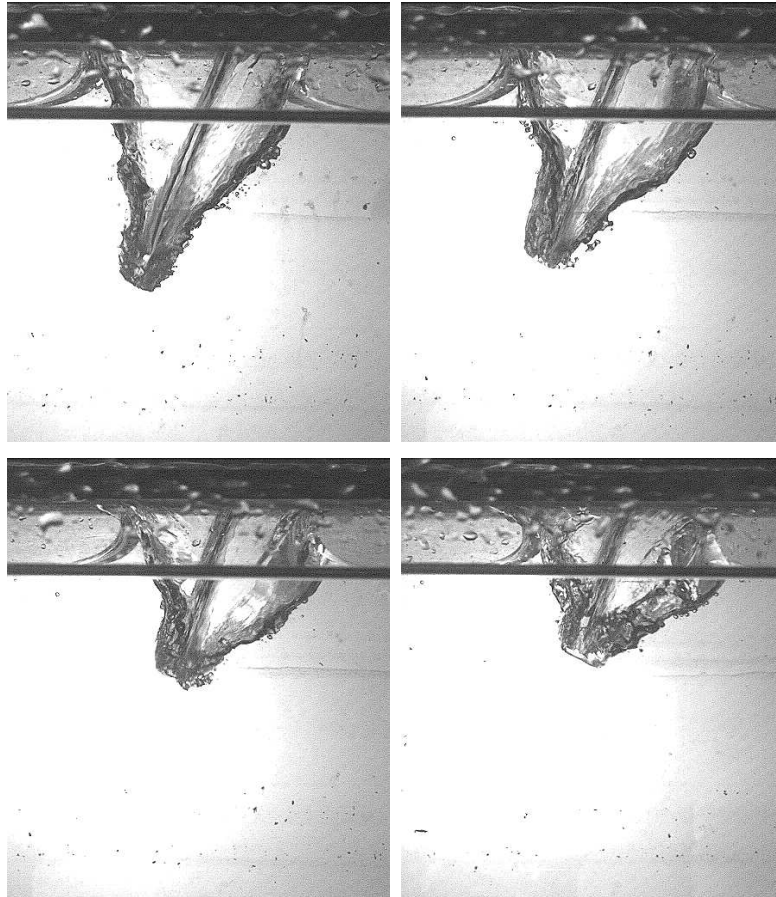


Figure 5.10: Jet condition V, $t/t_{po} = 2/3$. $V_t = 0.15 \text{ m/s}$, ($t = 71 \text{ ms}$) (top left); $V_t = 0.30 \text{ m/s}$, ($t = 63 \text{ ms}$) (top right); $V_t = 0.45 \text{ m/s}$, ($t = 47 \text{ ms}$) (bottom left); $V_t = 0.60 \text{ m/s}$, ($t = 38 \text{ ms}$) (bottom right)

Finally, Figures 5.11 and 5.12 correspond to the five mentioned translating velocities right at the pinch-off time. It can be observed that the pinch-off occurs at earlier times and closer to the free surface for the faster translating jets.

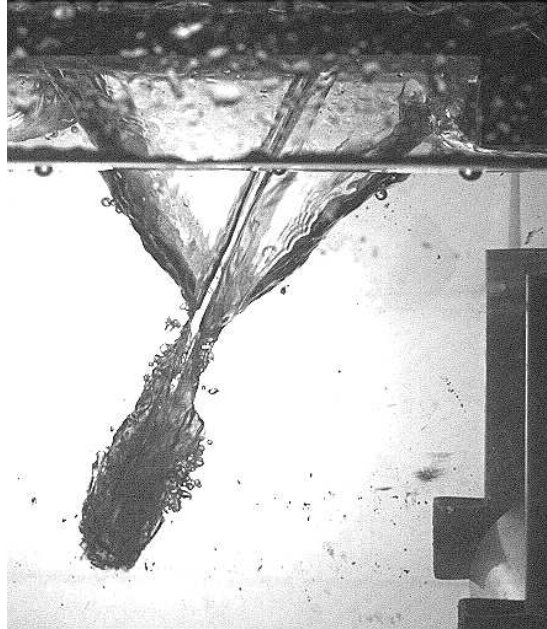


Figure 5.11: Jet condition V, $V_t = 0.00 \text{ m/s}$, $t/t_{po} = 1$ ($t = 116 \text{ ms}$)

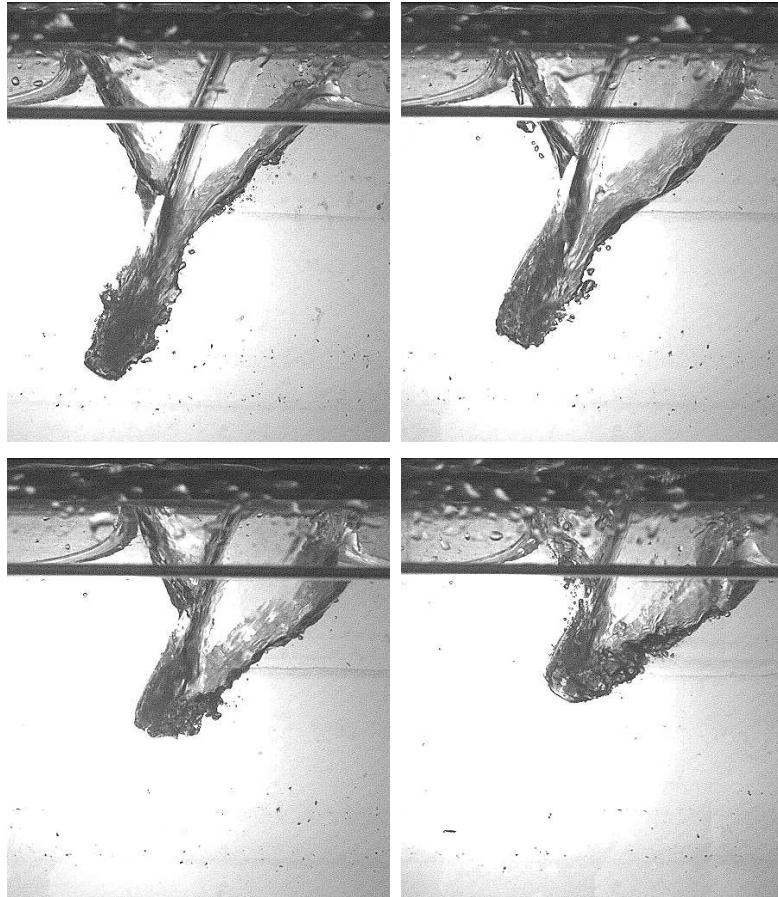


Figure 5.12: Jet condition V, $t/t_{po} = 1$. $V_t = 0.15 \text{ m/s}$, ($t = 106 \text{ ms}$) (top left); $V_t = 0.30 \text{ m/s}$, ($t = 95 \text{ ms}$) (top right); $V_t = 0.45 \text{ m/s}$, ($t = 71 \text{ ms}$) (bottom left); $V_t = 0.60 \text{ m/s}$, ($t = 57 \text{ ms}$) (bottom right)

5.3 Measurements of the Pinch-Off Depths and Pinch-Off Times

The described high-speed movies were used to measure the pinch-off times and the pinch-off depths for all six jet conditions (I thru VI) for five different jet horizontal translating velocities (0.00, 0.15, 0.30, 0.45 and 0.60 m/s). The pinch-off depths were determined visually on the movie frames and the results were translated from pixels into physical dimensions by using the calibration images described in previous sections. The pinch-off times were determined by counting the number of frames between the jet impact on the free surface and the pinch-off event and knowing that the time interval between frames is 0.001 secs. Several movies of each case were taken to get statistical information on these values (performing a larger number of repetitions for the jet conditions where a larger variability in the results was observed). The number of repetitions for each jet condition is shown in Table 5.1. Table 5.3, and 5.4 show the measured mean and standard deviation for the pinch-off times.

Exp	Pinch-Off Times (s) - Mean				
	$V_t = 0.00$	$V_t = 0.15$	$V_t = 0.30$	$V_t = 0.45$	$V_t = 0.60$
Cond	(m/s)	(m/s)	(m/s)	(m/s)	(m/s)
I	0.131	0.113	0.102	0.092	0.077
II	0.116	0.127	0.118	0.107	0.122
III	0.124	0.110	0.083	0.074	0.077
IV	0.117	0.091	0.066	0.050	0.036
V	0.115	0.098	0.089	0.077	0.065
VI	0.137	0.122	0.106	0.090	0.084

Table 5.3: Measurements of the pinch-off times (mean)

Exp	Pinch-Off Times (s) - St Dev				
	$V_t = 0.00$	$V_t = 0.15$	$V_t = 0.30$	$V_t = 0.45$	$V_t = 0.60$
Cond	(m/s)	(m/s)	(m/s)	(m/s)	(m/s)
I	0.002	0.002	0.006	0.010	0.001
II	0.005	0.012	0.010	0.020	0.015
III	0.002	0.004	0.008	0.006	0.007
IV	0.001	0.001	0.003	0.009	0.001
V	0.004	0.007	0.007	0.007	0.007
VI	0.002	0.001	0.003	0.003	0.006

Table 5.4: Measurements of the pinch-off times (standard deviation)

Table 5.5, and 5.6 show the measured mean and standard deviation for the pinch-off depths.

Exp	Pinch-Off Depths (cm) - Mean					
	Cond	$V_t = 0.00$ (m/s)	$V_t = 0.15$ (m/s)	$V_t = 0.30$ (m/s)	$V_t = 0.45$ (m/s)	$V_t = 0.60$ (m/s)
I		4.9	3.8	2.6	1.7	1.0
II		3.7	4.6	4.1	3.7	3.7
III		7.0	5.1	3.0	2.2	1.4
IV		5.1	3.9	2.3	1.3	1.0
V		4.1	3.7	2.7	1.9	1.1
VI		6.3	4.7	3.0	2.4	1.1

Table 5.5: Measurements of the pinch-off depths (mean)

Exp	Pinch-Off Depths (cm) - St Dev					
	Cond	$V_t = 0.00$ (m/s)	$V_t = 0.15$ (m/s)	$V_t = 0.30$ (m/s)	$V_t = 0.45$ (m/s)	$V_t = 0.60$ (m/s)
I		0.3	0.1	0.0	0.5	0.2
II		0.6	0.7	0.7	0.8	0.6
III		0.4	0.3	0.4	0.4	0.8
IV		0.3	0.2	0.2	0.6	0.1
V		0.2	0.8	0.5	0.1	0.3
VI		0.3	0.4	0.4	0.4	0.2

Table 5.6: Measurements of the pinch-off depths (standard deviation)

The t-probability distribution (also called the Student's probability distribution) was used to estimate confidence intervals for the measurements of the pinch-off times and depths. The confidence intervals based on the t-probability are particularly suitable when the sample size is small, as in the case of the current results [33]. The confidence interval associated with the t-probability distribution is calculated according to the formula:

$$CI = \frac{\sigma}{\sqrt{N}} \cdot t_c \quad (5.3)$$

where N is the sample size, σ is the standard deviation and t_c is a tabulated coefficient that depends on the sample size and a given probability level (P). P is the probability with which a measurement is expected to fall within the range of values $[\mu - CI, \mu + CI]$, with μ being the measured mean value. The confidence intervals for the pinch-off times and depths were calculated using a probability value of P=95%. Table 5.7 gives the values of t_c for this probability level and for sample sizes from 2 to 5 [34].

N	2	3	4	5
t_c	12.71	4.30	3.18	2.78

Table 5.7: t_c values for CI computation for a 95% probability level

Table 5.8 and 5.9 gives the CI values for the pinch-off time and depth measurements. The value of t_c was selected, for each condition, according to the number of repetitions given in Table 5.1.

Exp	Pinch-Off Depths (cm) - CI(95%)					
	Cond	$V_t = 0.00$ (m/s)	$V_t = 0.15$ (m/s)	$V_t = 0.30$ (m/s)	$V_t = 0.45$ (m/s)	$V_t = 0.60$ (m/s)
I		0.6	0.3	0.1	1.2	0.6
II		0.7	0.9	0.9	1.0	0.8
III		0.9	0.6	1.1	1.0	1.8
IV		2.5	1.9	1.9	5.2	1.1
V		0.4	1.9	1.3	0.3	0.7
VI		0.7	1.0	1.0	1.0	0.5

Table 5.8: Measurements of the pinch-off depths (CI for 95%)

Exp	Pinch-Off Times (s) - CI(95%)					
	Cond	$V_t = 0.00$ (m/s)	$V_t = 0.15$ (m/s)	$V_t = 0.30$ (m/s)	$V_t = 0.45$ (m/s)	$V_t = 0.60$ (m/s)
I		0.004	0.004	0.015	0.025	0.001
II		0.006	0.015	0.012	0.025	0.019
III		0.005	0.010	0.019	0.014	0.017
IV		0.013	0.013	0.025	0.083	0.013
V		0.010	0.018	0.018	0.018	0.018
VI		0.004	0.001	0.006	0.008	0.015

Table 5.9: Measurements of the pinch-off times (CI for 95%)

5.4 Dimensional Analysis

The pinch-off times (t_{po}), depths (d_{po}) and the resulting flow depends on the characteristics of the impacting jet (V_j , T_j and θ_j), the jet horizontal translating velocity (V_t), the density and viscosity of the liquid (ρ_l and μ_l), the density and viscosity of the ambient gas (ρ_g and μ_g), the surface tension (σ) and the acceleration of gravity (g). These ten variables can be grouped into seven non-dimensional parameters which along with the pinch-off times and depths can be expressed as:

$$\frac{t_{po}V_j}{T_j} = F \left(Fr_j = \frac{V_j}{\sqrt{gT_j}}, \frac{V_t}{V_j}, \theta_j, Re_j = \frac{V_j T_j}{\mu_l / \rho_l}, We_j = \frac{V_j^2 T_j}{\sigma / \rho_l}, \frac{\rho_g}{\rho_l}, \frac{\mu_g}{\mu_l} \right) \quad (5.4)$$

$$\frac{d_{po}}{T_j} = G \left(Fr_j = \frac{V_j}{\sqrt{gT_j}}, \frac{V_t}{V_j}, \theta_j, Re_j = \frac{V_j T_j}{\mu_l / \rho_l}, We_j = \frac{V_j^2 T_j}{\sigma / \rho_l}, \frac{\rho_g}{\rho_l}, \frac{\mu_g}{\mu_l} \right) \quad (5.5)$$

Both liquid and gas were kept constant throughout all the experiments, and thus the last two parameters were also constant. The Reynolds number was large for all cases and also, the free slip surface prevents significant boundary layers. Therefore, it is expected the effects of viscosity can reasonably be neglected to capture first-order effects. The We numbers based on the jet thickness (T_j) shown in Table 5.1 range from 2.1 to 4.6, which are not very large but to get a more accurate estimate of the relative importance between the inertial and surface tension effects at the air-water interface, the We number should be computed using the local radius of curvature of the air-crater interface rather than the jet thickness T_j . During the formation of the underwater craters, the radius of curvature of the air-water interface is relatively large compared to T_j , and hence give much larger We numbers than the ones shown in Table 5.1. The surface tension, however, may be important after the cavity collapse due to the small

radius of curvature of the small bubbles and may have a strong influence in the characteristics of the resulting bubbly plume. Therefore, to study the air cavity formation process up to the point of the pinch-off time, the former expressions can be simplified to the following:

$$\frac{t_{po}V_j}{T_j} = F \left(Fr_j, \frac{V_t}{V_j}, \theta_j \right) \quad (5.6)$$

$$\frac{d_{po}}{T_j} = G \left(Fr_j, \frac{V_t}{V_j}, \theta_j \right) \quad (5.7)$$

Chapter 6

The Flow Field Near the Tip of the Underwater Planar Jet - PIV Experiments

The visualization experiments described in Chapter 5 showed the general features of the flow and the characteristic sequence of events related to the jet impact. Out of all these events, special attention is paid in this thesis to the formation and subsequent pinch-off of the underwater craters.

In order to understand the crater formation process, it is important to achieve a better understanding of the underwater jet dynamics, and thus the flow field in the near region of the underwater jet tip. For this purpose, Chapter 6 presents PIV measurements performed in the region near the jet tip during the crater formation process.

6.1 Experimental Set-Up - PIV

The flow field near the underwater jet tip was measured using a double-frame single-exposure particle image velocimetry technique. In order to take the PIV measurements, the tank and jet water were seeded with $25\ \mu\text{m}$ spherical hollow glass particles and the flow was illuminated with $12\ \text{mJ}$ light pulses generated by a high-speed Nd:YAG laser (Clark MXR, model ORC-1000). The PIV images were recorded with a Phantom V4.0 high-speed digital camera. The laser beam was expanded into a light sheet by using a $225\ \text{mm}$ cylindrical lens while a combination of two additional cylindrical lenses (75 and $100\ \text{mm}$ focal length) were used to focus the beam into a laser sheet approximately $1\ \text{mm}$ thick. A set of mirrors was used to center the vertical light sheet in between the two vertical walls of the jet edge deflector device and parallel to them by sending the laser beam below the water tank and then directed upwards through the glass tank bottom as shown in Figure 6.1. The light sheet was stationary with respect to the tank.

The camera was attached to the jet carriage with an orientation that allowed for an upward viewing angle (about 10°) at the underwater jet tip through the glass vertical side walls. Also, the jet cutter device was timed with the carriage speed such that the jet plunged into the region illuminated by the laser. The region near the underwater jet tip was therefore lighted by the laser from beneath at the center span of the jet as shown in Figure 6.2.

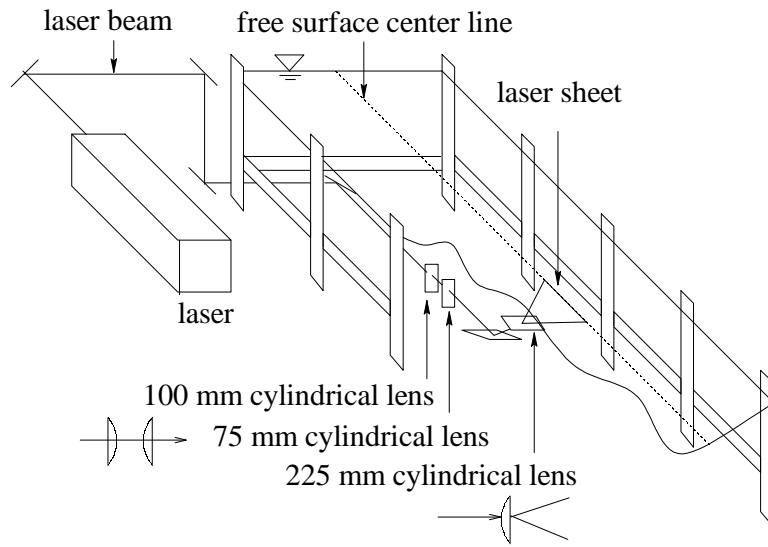


Figure 6.1: Laser beam path and lenses

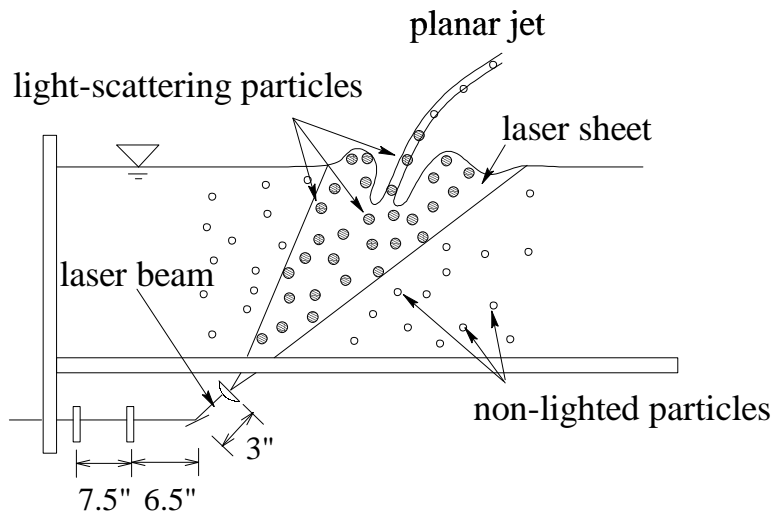


Figure 6.2: Lateral view of the PIV setup

The camera was set to operate at 1000 fps, keeping the shutter open during the entire time of each frame. The background light intensity was insufficient to register on the CCD during this time, rendering the effective exposure time to be given by the duration of the laser pulses ($\approx 500 \text{ ns}$). The camera was also programmed to send a TTL output signal at the beginning of each frame, which was used to synchronize the output of an arbitrary waveform to the framing of the camera. The arbitrary waveform generator was programmed to create two delayed pulses spaced 0.40 ms apart such that they straddle two consecutive camera frames. Thus, the first of the two pulses was created at the end of one camera frame and the second pulse at the beginning of the next (see Figure 6.3). The double pulse signal was used to trigger the laser, thus providing a pair of PIV images spaced 0.40 ms at a rate of 500 Hz .

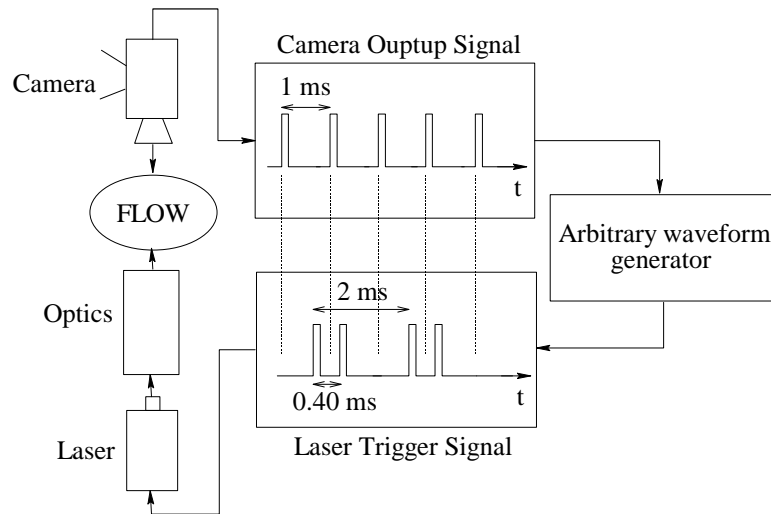


Figure 6.3: Schematic of the PIV set-up and camera-laser synchronization.

Each pair of PIV images was cross-correlated with DaVis 6.0 in four passes with decreasingly smaller window sizes from 32 by 32 pixels to 8 by 8 and an overlap of 50%. The areas of the frames that were contaminated by light reflections coming from the underwater crater walls were masked out from the processed vector fields. Figure 6.4 shows one of the PIV frames and the region where the PIV processing was applied.

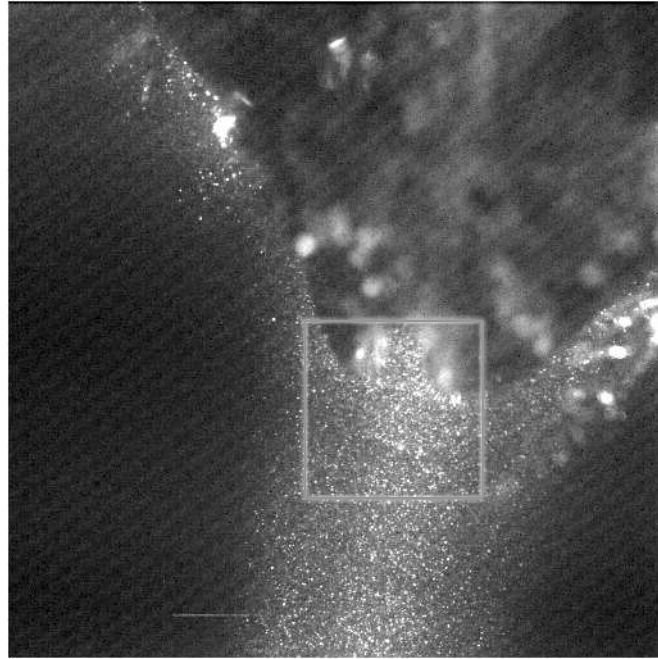


Figure 6.4: PIV picture for condition III. $V_t = 0.3 \text{ m/s}$. The picture shows the PIV particles and the two underwater air craters. The camera is translating with the jet from right to left. The rectangle ($17 \times 17 \text{ mm}$) is the region where the PIV processing was applied.

Finally, a picture of a calibrated grid placed on the plane of the laser sheet was acquired and used to convert the measured velocities from pixels per second to physical dimensions.

6.2 Velocity Field Near the Jet Tip

PIV measurements of the flow near the underwater jet tip were performed for jet condition III at five different jet translation velocities: $V_t=0.0, 0.15, 0.30, 0.45$ and 0.6 m/s . The PIV movies were also used to measure the underwater jet tip velocity and jet angle of penetration with respect to the vertical in a reference frame fixed with the jet carriage by tracking the position of the leading edge of the underwater craters with time. For this purpose, Adobe Photoshop 7.0 was used to measure the relative displacement between the craters in two selected frames of each movie spaced 8 ms apart. The measured velocities and angles could be expressed in a reference frame fixed to the water tank, since the jet carriage velocity V_t was known. The measured jet tip velocities (V_p) and penetration angles (α_p) expressed in a reference frame fixed with respect to the water tank and also with respect to the jet carriage (V_c and α_c) were extracted from these results, and are summarized in Tables 6.1 and 6.2.

Ref Frame	Underwater Jet Tip Velocity (m/s)				
	$V_t = 0.00$ (m/s)	$V_t = 0.15$ (m/s)	$V_t = 0.30$ (m/s)	$V_t = 0.45$ (m/s)	$V_t = 0.60$ (m/s)
Carriage (V_c)	1.59	1.64	1.47	1.58	1.51
Tank (V_p)	1.59	1.69	1.59	1.78	1.78

Table 6.1: Measurements of the underwater jet tip velocity for jet condition III

Ref Frame	Underwater Jet Tip Velocity Inclination Angle (degrees)				
	$V_t = 0.00$ (m/s)	$V_t = 0.15$ (m/s)	$V_t = 0.30$ (m/s)	$V_t = 0.45$ (m/s)	$V_t = 0.60$ (m/s)
Carriage (α_c)	19.1	18.2	17.5	20.2	17.5
Tank (α_p)	19.1	23.0	27.9	33.9	36.2

Table 6.2: Measurements of the underwater jet penetration angle with the vertical for jet condition III

The processed PIV vector field for $V_t=0$ is shown in Figure 6.5.

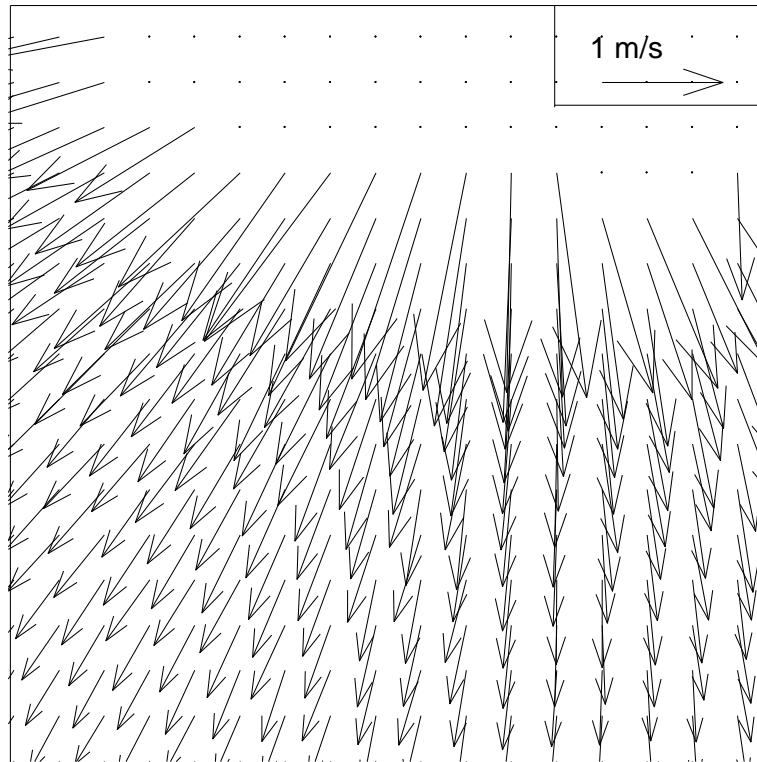


Figure 6.5: PIV vector field for jet condition III and $V_t = 0.0 \text{ m/s}$ in a reference frame moving with the jet carriage. Actual image size $17 \times 17 \text{ mm}$

The flow field of Figure 6.5 can be expressed in a reference frame fixed with respect to the underwater jet tip by subtracting the jet tip velocity measured in a reference frame fixed with the carriage (V_c). The resulting flow is shown in Figure 6.6.

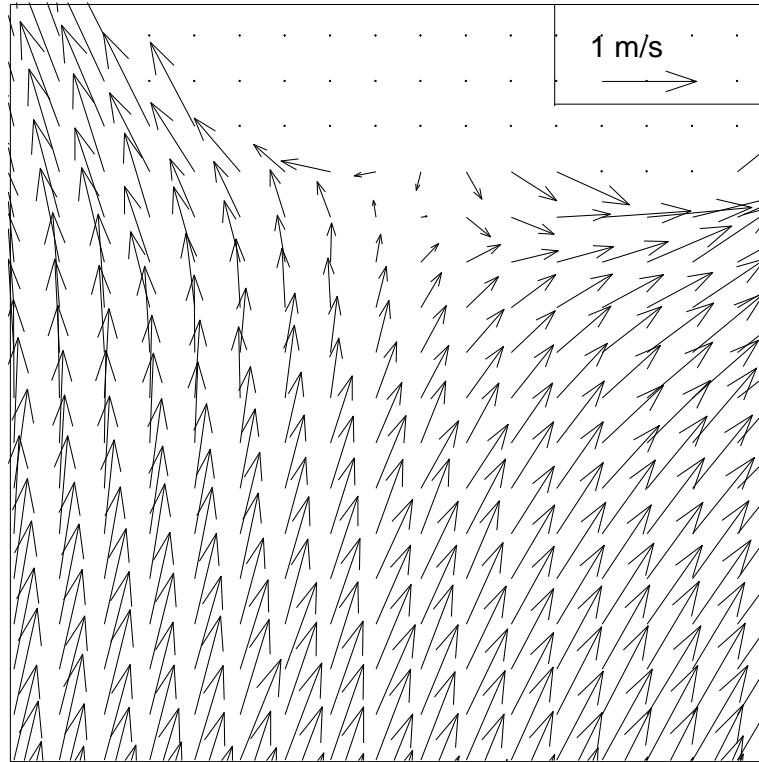


Figure 6.6: PIV vector field for jet condition III and $V_t = 0.0 \text{ m/s}$ in a reference frame moving with the jet tip. Actual image size $17 \times 17 \text{ mm}$

As a final step to aid in qualitative visualization, Matlab 6.0 was used to calculate the streamlines associated with each of the measured vector fields.

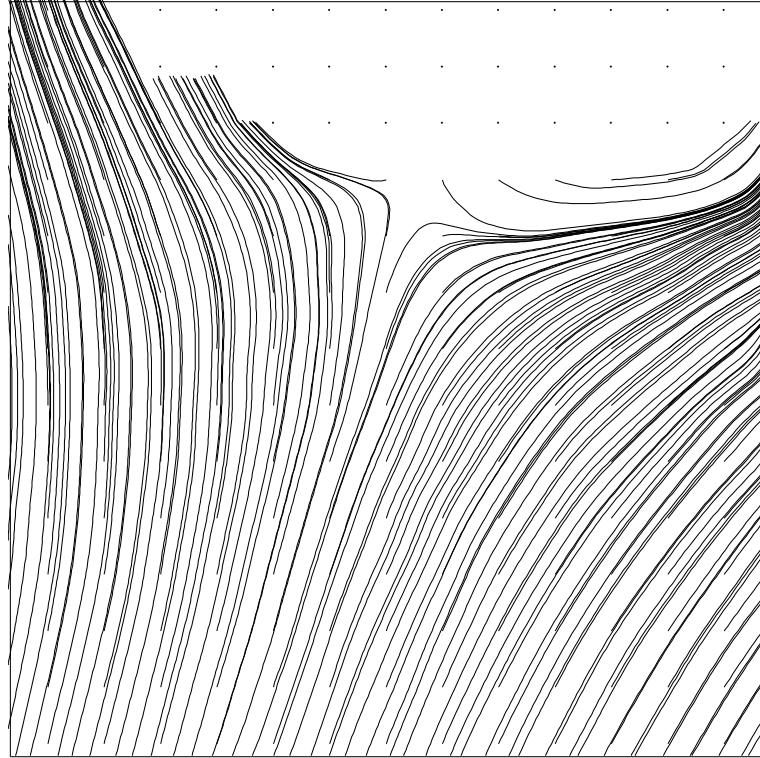


Figure 6.7: PIV streamlines for jet condition III and $V_t = 0.0 \text{ m/s}$ in a reference frame moving with the jet tip. Actual image size $17 \times 17 \text{ mm}$

Figures 6.5 and 6.6 show that in a reference frame moving with the leading edge of the cavity, the underwater jet sees a uniform stream that moves upwards towards the plunging stream. The freestream of fluid from the pool curves closely around the air craters, except for one streamline that finds the jet water at a stagnation point. Two other streamlines branch-off from the stagnation point, which are the dividing lines between the jet water and the incoming tank water stream. As the jet horizontal translating speed is increased, the stagnation point moves upwards and to the left with respect the jet tip as can be seen in the rest of the PIV images (Figures 6.8 thru 6.11). The qualitative information on the flowfield near the underwater jet tip obtained from the PIV measurements is the starting point of the theoretical discussion presented in Chapter 7.

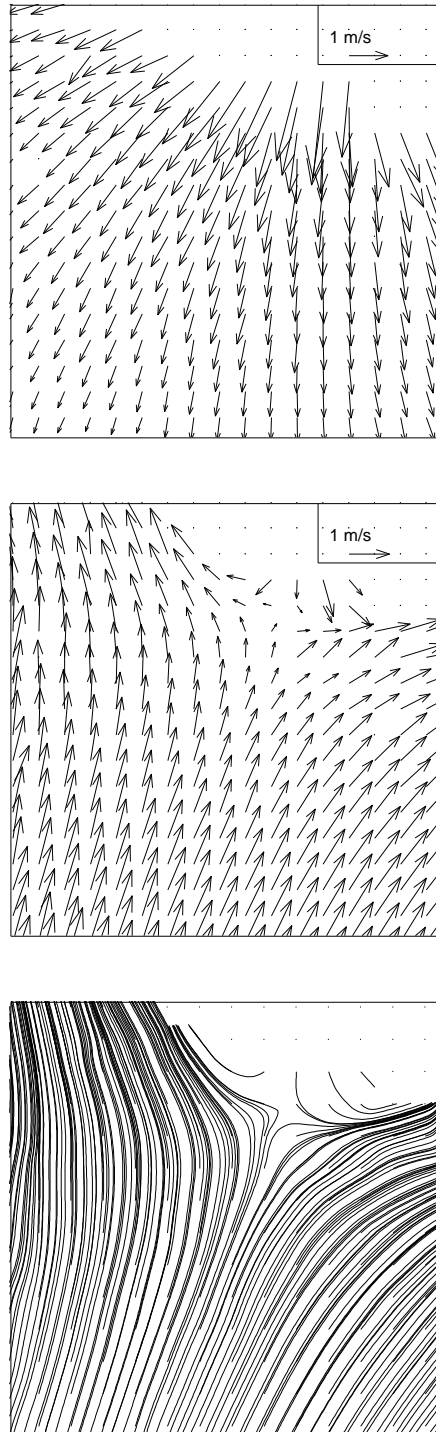


Figure 6.8: PIV vector field for jet condition III and $V_t = 0.15 \text{ m/s}$ in a reference frame moving with the jet carriage (top), moving with the jet tip (middle) and PIV streamlines (bottom). Actual image size $17 \times 17 \text{ mm}$

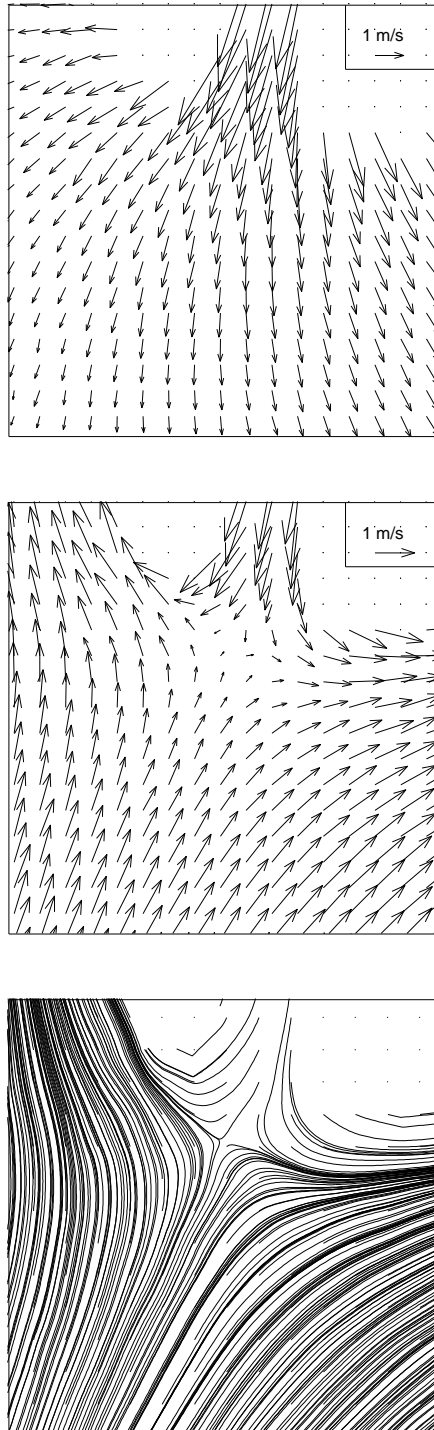


Figure 6.9: PIV vector field for jet condition III and $V_t = 0.30 \text{ m/s}$ in a reference frame moving with the jet carriage (top), moving with the jet tip (middle) and PIV streamlines (bottom). Actual image size $17 \times 17 \text{ mm}$

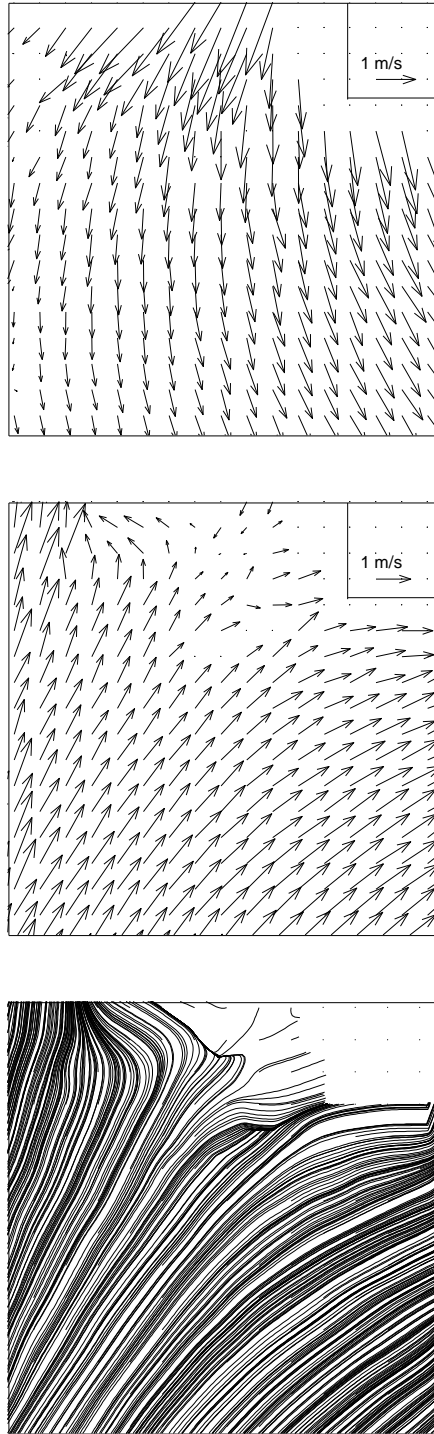


Figure 6.10: PIV vector field for jet condition III and $V_t = 0.45 \text{ m/s}$ in a reference frame moving with the jet carriage (top), moving with the jet tip (middle) and PIV streamlines (bottom). Actual image size $17 \times 17 \text{ mm}$

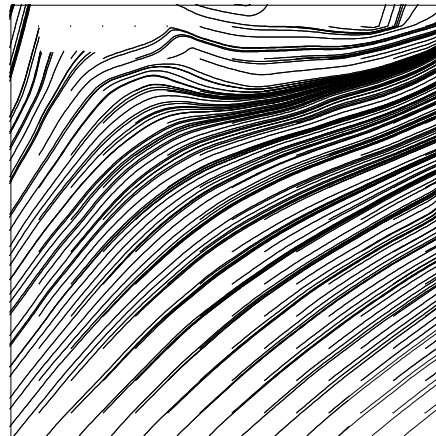
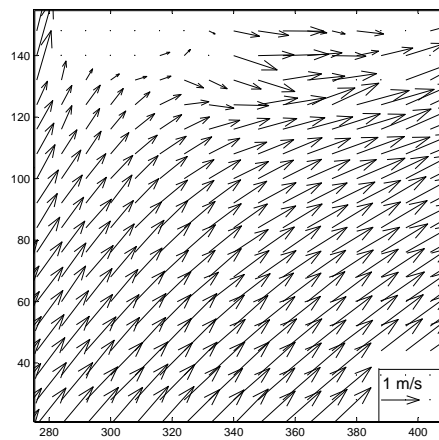
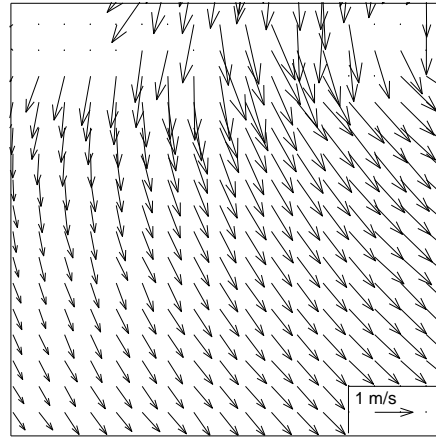


Figure 6.11: PIV vector field for jet condition III and $V_t = 0.60 \text{ m/s}$ in a reference frame moving with the jet carriage (top), moving with the jet tip (middle) and PIV streamlines (bottom). Actual image size $17 \times 17 \text{ mm}$

Chapter 7

Theoretical Model and Discussion

In this chapter, a theoretical model for the crater formation and subsequent collapse of the underwater cavities created by an inclined, horizontally translating planar jet is presented. The model is developed under the assumptions of quasi-steady potential flow and negligible free surface effects. Under these assumptions, Section 7.1 gives the propagation velocity of the cavity's leading edge as a function of the jet impact properties (V_j , T_j and θ_j), Section 7.2 develops relations for the shape of the craters without the influence of gravitational collapse, and Section 7.3 discusses the roles played by gravity and the fluid inertia in the crater dynamics. All these results are combined with simple scaling arguments in Section 7.4 to estimate the shapes of the underwater craters as a function of time and subsequently, the pinch-off times and depths, culminating with a comparison to the experimental data presented in Chapter 5.

7.1 Underwater Jet Tip Velocity

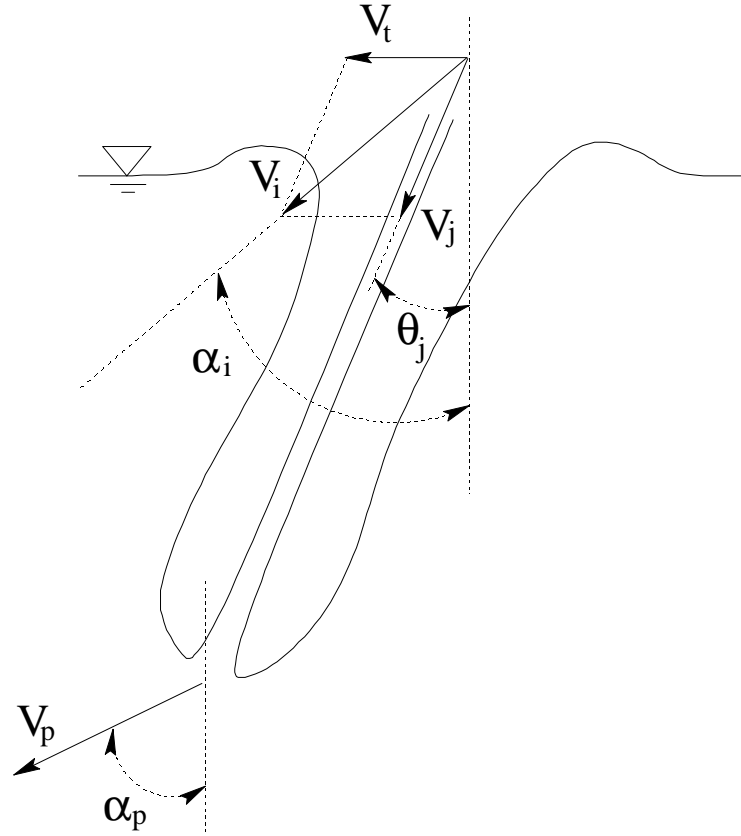


Figure 7.1: Schematic of the underwater jet and velocities in a reference frame fixed with respect to the water tank

Figure 7.1 shows a schematic of the underwater jet that is translating horizontally at a velocity \vec{V}_t from right to left at an arbitrary instant in time between the jet impact on the free surface and the crater pinch-off. In the figure are shown the two air craters formed as a result of the transient jet impact, as well as the velocities of the water particles far upstream in the jet (\vec{V}_i) and at the tip of

the underwater jet (\vec{V}_p) when they are measured in a reference frame fixed with respect to the water tank. \vec{V}_i is the vectorial addition of the jet water velocity in a reference frame fixed to the carriage (\vec{V}_j) and the velocity of the carriage with respect to the tank (\vec{V}_t) and makes an angle α_i with respect to the vertical. Note that V_i and α_i can be determined from the jet characteristics defined in section 5.1.2 (V_j and θ_j) and the jet horizontal translating velocity (V_t):

$$V_i = \sqrt{(V_t + V_j \sin(\theta_j))^2 + (V_j \cos(\theta_j))^2} \quad (7.1)$$

$$\alpha_i = \arctan \left\{ \frac{V_t + V_j \sin(\theta_j)}{V_j \cos(\theta_j)} \right\} \quad (7.2)$$

It is intended in this section to determine the velocity magnitude and direction (V_p and α_p) of the cavity's leading edge as a function of the jet impact properties (V_j and θ_j) and the jet horizontal translation velocity, V_t , which were measured in the experiments.

For this purpose, it is more convenient to formulate the problem in a reference frame fixed with respect to the underwater jet tip as shown in Figure 7.2. In this reference frame, the tank water moves towards the jet tip at a velocity equal to V_p in magnitude, while the jet water particles move with a velocity equal to $\vec{V}_i + \vec{V}_p$ as shown in the figure. The streamlines of the tank water free-stream are straight far from the jet and curve as they get close to the jet tip due to the presence of the air craters. Only one streamline (labelled streamline 'a' in the figure) meets the jet incoming water at the stagnation point. The jet streamline that meets streamline 'a' is labelled streamline 'b' in the figure. As the fluid in the jet approaches the stagnation point, it curves around the tips of the air craters and eventually travels upwards in a direction almost parallel to the air/water

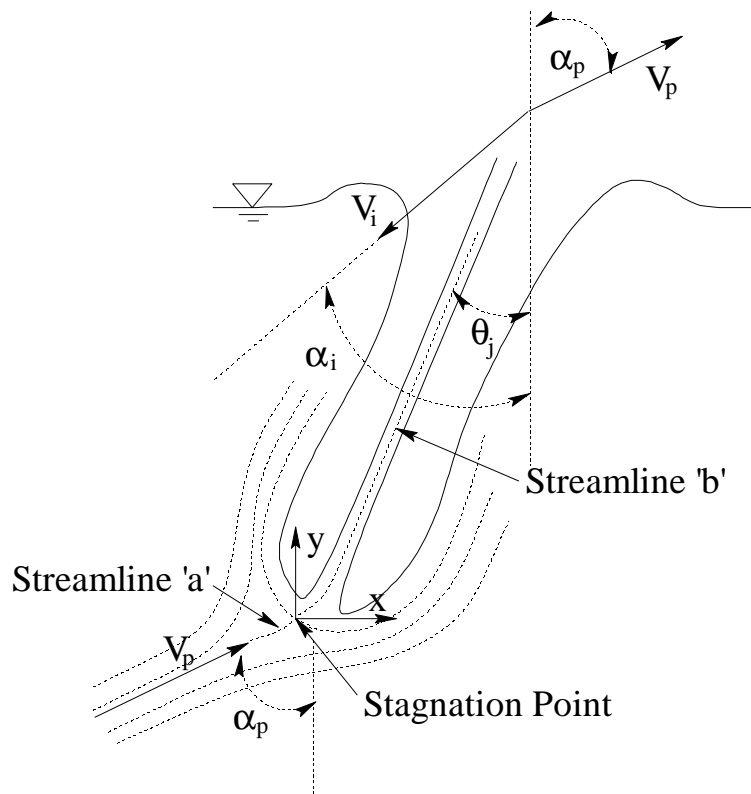


Figure 7.2: Schematic of the underwater jet and velocities in a reference frame fixed with respect to the jet tip

interfaces. Two other streamlines start at the stagnation point which are the dividing lines between the jet water and the water of the receiving pool.

The theory presented in this section is developed under the assumption of quasi-steady flow. This assumption is satisfied as long as the temporal accelerations are much smaller than the spatial accelerations associated to the fluid inertia, which dominates the flow around the jet tip, as it will be seen in section 7.3. Provided that V_j and T_j are the characteristic velocity and length associated to this problem, a rough estimate of orders of magnitude can be given to justify the quasi-steady state assumption,

$$\vec{V} \cdot \nabla \vec{V} \approx \frac{V_j^2}{T_j} \quad (7.3)$$

$$\frac{\partial \vec{V}}{\partial t} \approx \frac{V_j}{\delta t} \quad (7.4)$$

For both accelerations to be of the same order, δt needs to be

$$\delta t \approx \frac{T_j}{V_j} \quad (7.5)$$

That is, for the temporal accelerations to be of the same order of magnitude as the convective accelerations, changes in velocity of the order of V_j would need to take place in times of the order of $\delta t = T_j/V_j$. In a typical case presented herein, $V_j \approx 2 \text{ m/s}$ and $T_j \approx 0.003 \text{ m}$, resulting in a value for $\delta t = 1.5 \text{ ms}$. Or in other words, for the non-steady accelerations to be important, changes in velocity around the jet tip of the order of 2 m/s would need to be observed in about 2 ms . On the contrary, the jet penetration velocity was observed to remain virtually constant until the jet pinch-off times for all conditions (typically about 100 ms). Therefore, with the quasi-steady assumption satisfied and the additional constraint of negligible viscous effects, Bernoulli's principle can be applied, which states that the specific energy of a water particle is conserved as

it travels along a streamline. The specific energy e of a particle can be expressed in terms of the pressure (p), the water density (ρ), the particle speed (V), the acceleration of gravity (g) and the local depth (z) as follows:

$$e = p + \frac{1}{2}\rho V^2 - \rho g z \quad (7.6)$$

where the z -axis is directed downward ($z = 0$ at the free surface), e_a is the specific energy of the particles of streamline 'a' and e_b is the specific energy of the particles of streamline 'b' (see Figure 7.2). In the receiving pool far upstream from the jet tip, a particle in streamline 'a' is subjected only to the hydrostatic pressure $p_{atm} + \rho g z$ and has a velocity magnitude equal to V_p and thus:

$$e_a = p_{atm} + \rho g z_a + \frac{1}{2}\rho V_p^2 - \rho g z_a = p_{atm} + \frac{1}{2}\rho V_p^2 \quad (7.7)$$

For a particle that is in streamline 'b' and at $z = 0$, the velocity equals $\vec{V}_i + \vec{V}_p$ and the pressure is equal to the ambient pressure p_{atm} . The specific energy for such a particle is:

$$e_b = p_{atm} + \frac{1}{2}\rho \left| \vec{V}_i + \vec{V}_p \right|^2 \quad (7.8)$$

Since streamlines 'a' and 'b' have a common point (they meet at the stagnation point), e_a and e_b have to be equal and thus:

$$\frac{1}{2}\rho V_p^2 = \frac{1}{2}\rho \left| \vec{V}_i + \vec{V}_p \right|^2 \quad (7.9)$$

Also, \vec{V}_p and \vec{V}_i can be expressed as:

$$\vec{V}_p = V_p \left(\sin(\alpha_p)\vec{i} + \cos(\alpha_p)\vec{j} \right) \quad (7.10)$$

$$\vec{V}_i = -V_i \left(\sin(\alpha_i)\vec{i} + \cos(\alpha_i)\vec{j} \right) \quad (7.11)$$

Plugging 7.10 and 7.11 into 7.9, an expression for V_p is obtained:

$$V_p = \frac{V_i}{2 \cos(\alpha_p - \alpha_i)} \quad (7.12)$$

In this expression, α_p is unknown and an additional constraint is needed to close the problem. The additional constraint comes from imposing the velocity of the jet water particles to be parallel to the jet surface in a reference frame fixed with respect to the jet tip. In other words, the components of the velocities \vec{V}_i and \vec{V}_p perpendicular to the jet have to have equal magnitudes and opposite directions. Mathematically, this can be expressed as:

$$V_i \sin(\alpha_i - \theta_j) = V_p \sin(\alpha_p - \theta_j) \quad (7.13)$$

or by combining 7.12 with 7.13, it can be shown with some manipulation that this simplifies to:

$$\alpha_p = 2\alpha_i - \theta_j \quad (7.14)$$

which gives α_p as a function of known variables. V_p can be expressed as:

$$V_p = \frac{V_i}{2 \cos(\alpha_i - \theta_j)} \quad (7.15)$$

When the jet is stationary, $\alpha_i = \theta_j$ and $V_p = V_i/2$, as noted by others. Also, for this condition the velocity of the fluid near the free surface on the outer edge is nearly zero in a stationary reference frame. This is also the case for the translating jet.

In summary, expressions 7.12 and 7.14 give the magnitude and the direction of the underwater jet tip (V_p and α_p) as a function of known jet parameters.

Finally, an interesting observation can be made from the fact that a steady-state can only be obtained if the stagnation point moves away from the free surface and deeper into the pool; or stated another way, $\alpha_p < \pi/2$. This condition is equivalent to (see equation 7.14),

$$\alpha_i < \frac{\pi}{4} + \frac{\theta_j}{2} \quad (7.16)$$

or using equation 7.2,

$$\frac{V_t + V_j \sin \theta_j}{V_j \cos \theta_j} < \tan\left(\frac{\pi}{4} + \frac{\theta_j}{2}\right) = \frac{\cos \theta_j}{1 - \sin \theta_j} \quad (7.17)$$

which gives,

$$V_t < V_j \quad (7.18)$$

which is satisfied for all the conditions presented in this work.

If the relative translational velocity of the jet parallel to the impacting free surface exceeded the jet velocity, it would be impossible for the steady state conditions to be established. Unfortunately, it was not possible to force the operational parameters of the experiments to achieve values of V_t larger than V_j , and thus it was not possible to even qualitatively describe what occurs for these conditions. It may,

however, be possible to attain some of these states in natural wave conditions, depending on the wavelength and strength of the breaker. Lastly, note that the current analysis does not predict all the possible sources of non-steadiness and, for instance, it may be possible to force a stationary high-speed jet to bounce off the free surface at very shallow impact angles.

The underwater jet tip velocity (V_p) and angle (α_p) were measured by tracking the position of the underwater jet leading edge in the high-speed movies. The jet tip position was determined visually with the computer mouse for 5 frames equally spaced in time intervals of 15 *ms*. The results were fitted by least squares to obtain V_c and α_c , the magnitude and direction of the cavity's leading edge relative to the moving carriage frame of reference. These quantities were translated into a stationary reference frame, thus obtaining V_p and α_p . This process was repeated on three different repetitions of the movies for each condition in order to get statistical information. Figures 7.3 through 7.14 show α_p and V_p as a function of the carriage speed for all jet conditions. The solid lines are the theoretical prediction and the dots represent the averaged measured values. The error bars are the 95% confidence intervals based on a t-distribution (calculated as described in 5.3). It can be seen in the figures that the model represents well the trends of the functional dependency of these values with the translation speed. The model presents the largest deviations from the measured values for conditions V and VI. This fact may be associated with the fact that these two conditions have the smallest values of Fr_j and it is possible that the underwater jet trajectory may be more affected by the gravitational effects associated with the motion of the free surface than in the other cases.

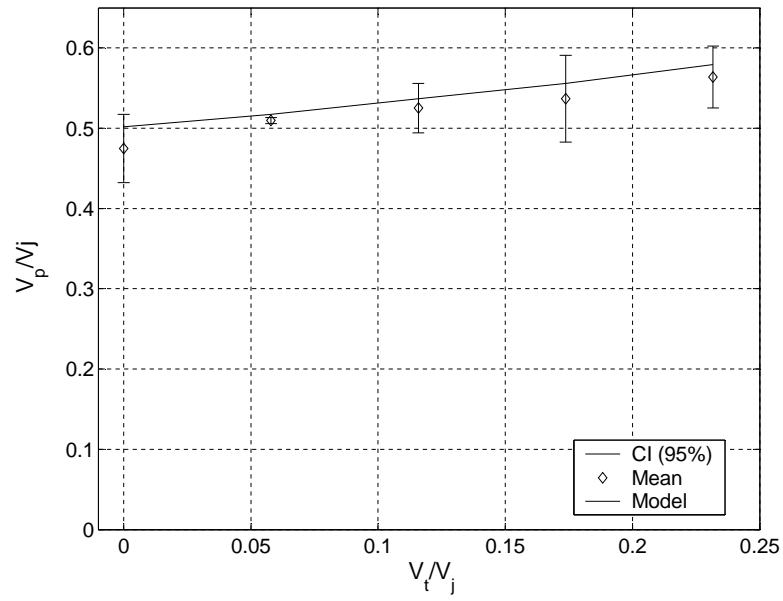


Figure 7.3: Underwater jet tip velocity (V_p) as a function of V_t/V_j in a stationary reference frame. Jet condition I

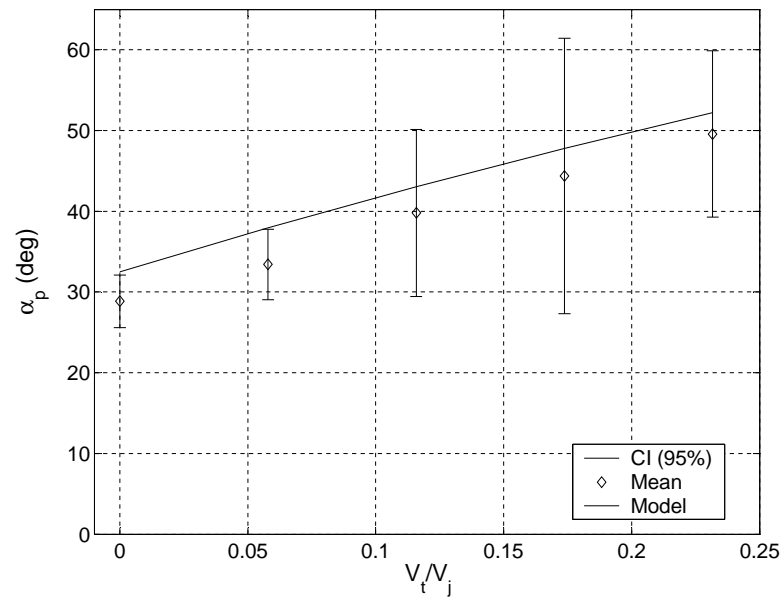


Figure 7.4: Underwater jet tip trajectory angle with respect to the vertical (α_p) as a function of V_t/V_j in a stationary reference frame. Jet condition I

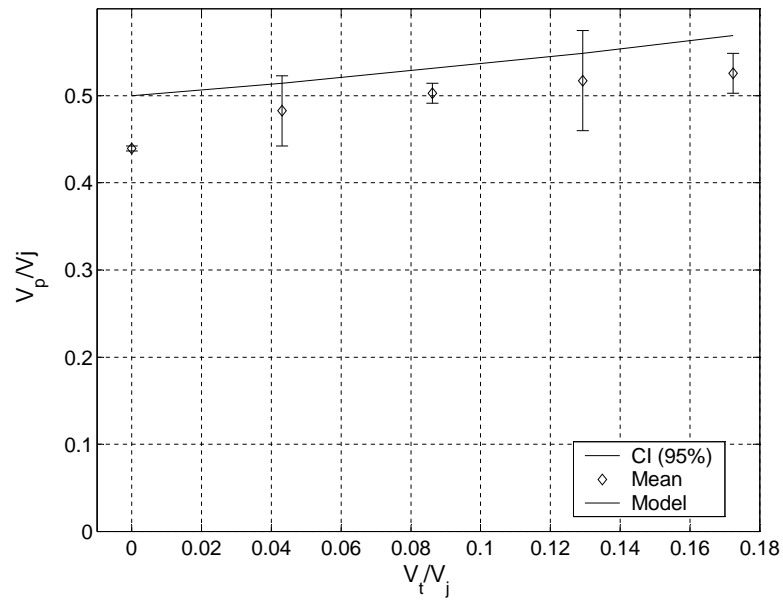


Figure 7.5: Underwater jet tip velocity (V_p) as a function of V_t/V_j in a stationary reference frame. Jet condition II

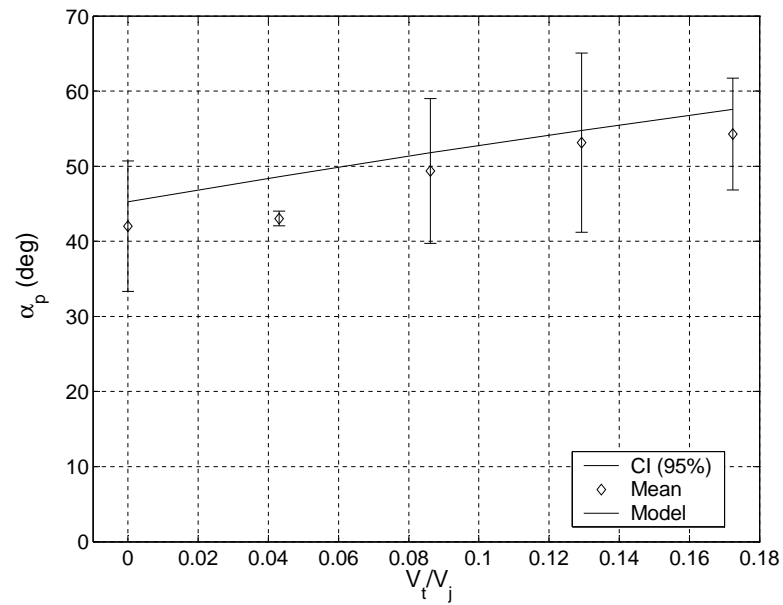


Figure 7.6: Underwater jet tip trajectory angle with respect to the vertical (α_p) as a function of V_t/V_j in a stationary reference frame. Jet condition II

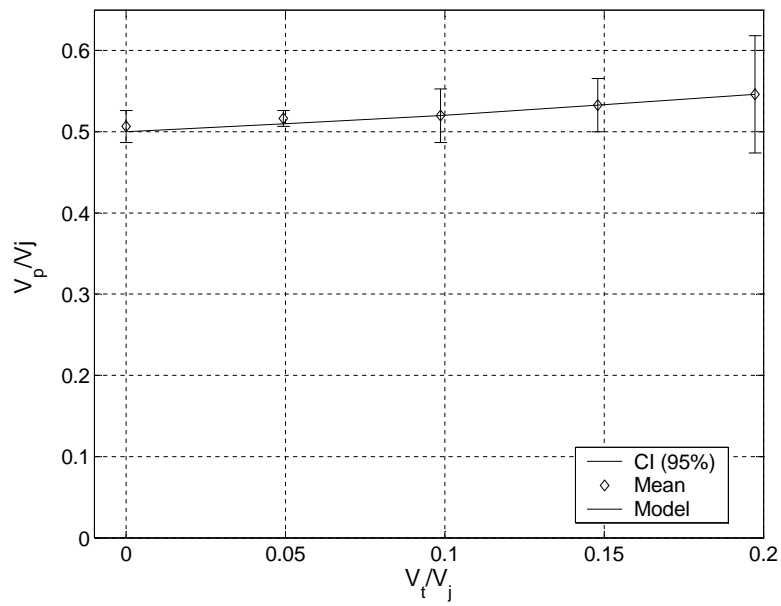


Figure 7.7: Underwater jet tip velocity (V_p) as a function of V_t/V_j in a stationary reference frame. Jet condition III

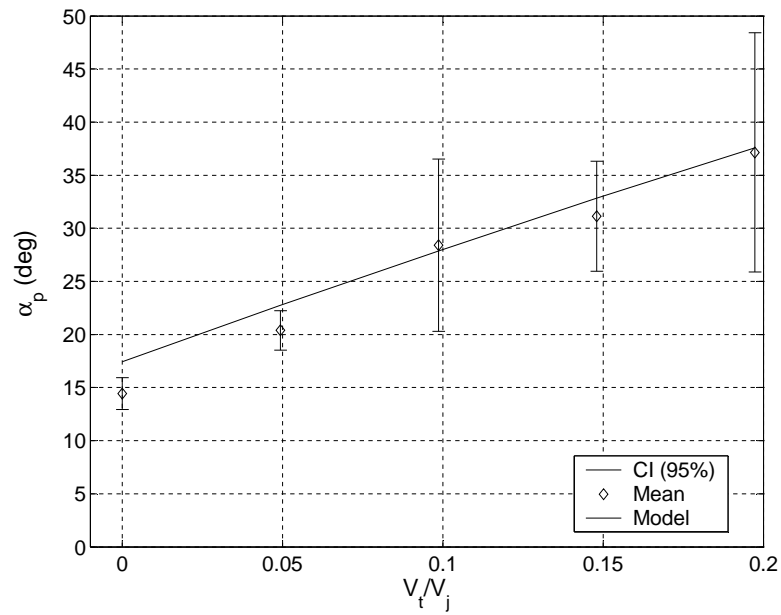


Figure 7.8: Underwater jet tip trajectory angle with respect to the vertical (α_p) as a function of V_t/V_j in a stationary reference frame. Jet condition III

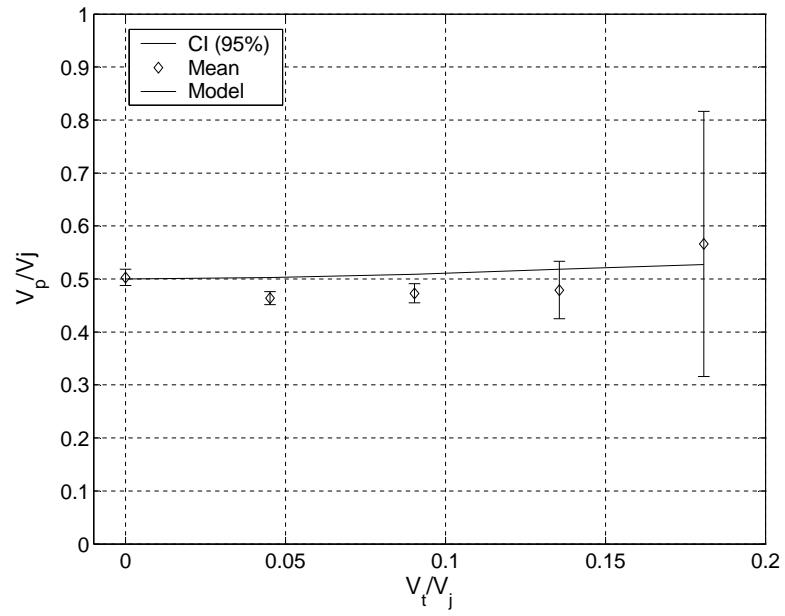


Figure 7.9: Underwater jet tip velocity (V_p) as a function of V_t/V_j in a stationary reference frame. Jet condition IV

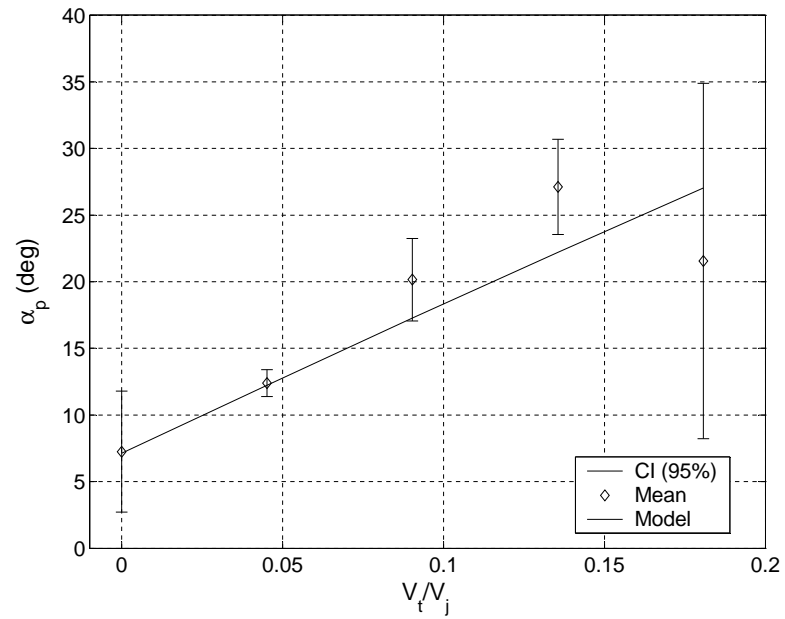


Figure 7.10: Underwater jet tip trajectory angle with respect to the vertical (α_p) as a function of V_t/V_j in a stationary reference frame. Jet condition IV

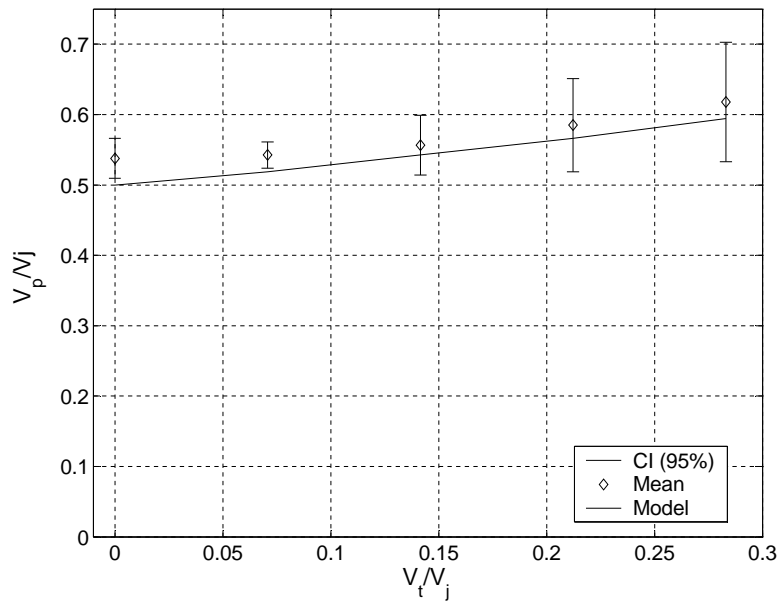


Figure 7.11: Underwater jet tip velocity (V_p) as a function of V_t/V_j in a stationary reference frame. Jet condition V

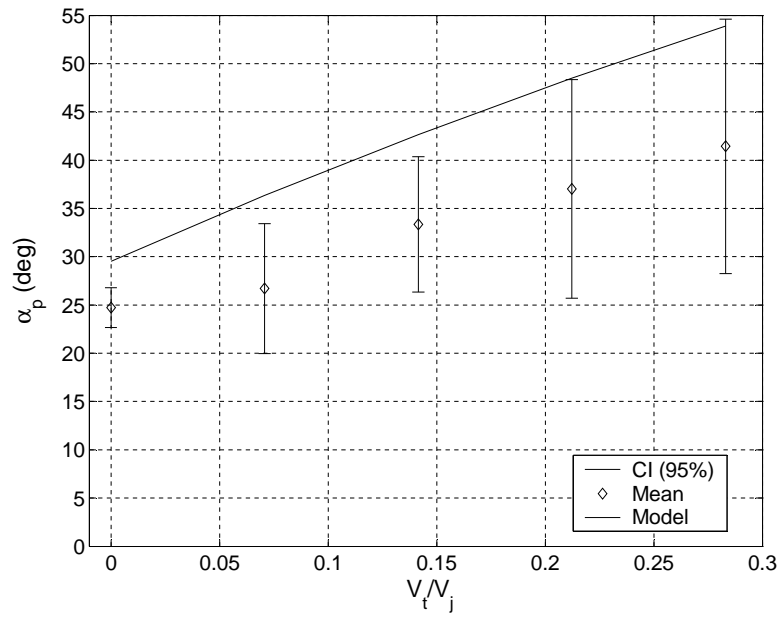


Figure 7.12: Underwater jet tip trajectory angle with respect to the vertical (α_p) as a function of V_t/V_j in a stationary reference frame. Jet condition V

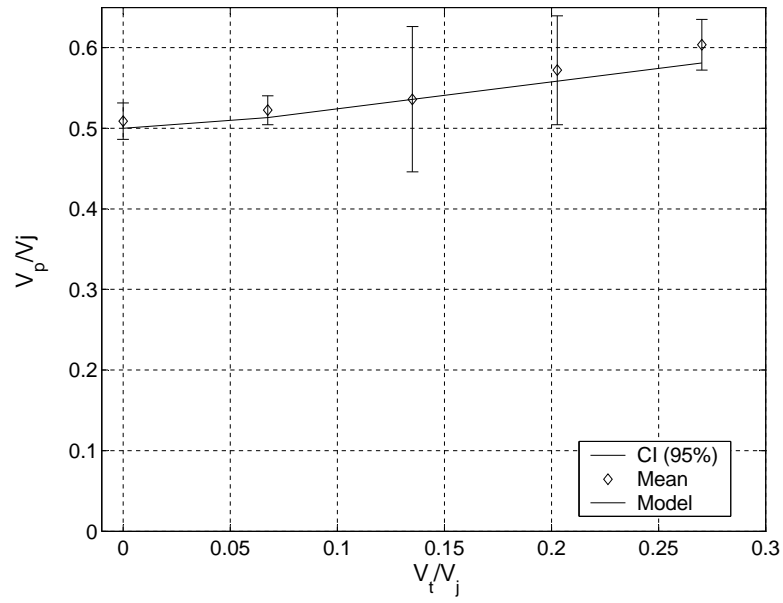


Figure 7.13: Underwater jet tip velocity (V_p) as a function of V_t/V_j in a stationary reference frame. Jet condition VI

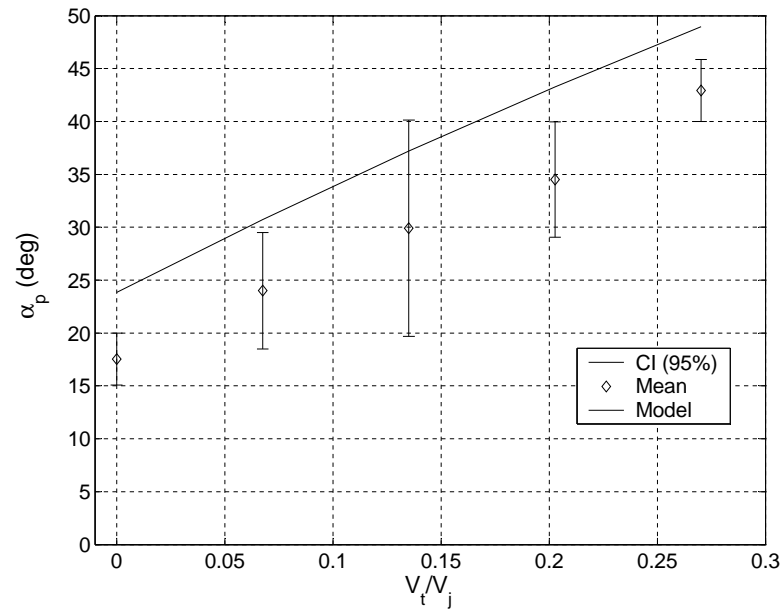


Figure 7.14: Underwater jet tip trajectory angle with respect to the vertical (α_p) as a function of V_t/V_j in a stationary reference frame. Jet condition VI

7.2 Solution Without Gravity - Shape of the Free Streamlines

In this section, the free surface shape produced by an inclined, translating, planar plunging jet in the absence of gravity under the assumption of quasi-steady potential flow is calculated. This solution will be used as a starting point to understand the problem of crater formation and subsequent collapse which was observed in the experiments.

The solution obtained for the magnitude and direction of the underwater jet tip velocity given by equations 7.12 and 7.14 is also valid for the non-gravitational problem. Thus, in a reference frame fixed to the jet tip, the plunging jet problem can be regarded as a free jet of velocity V_p that meets an incoming uniform stream also at velocity V_p , with the jet and the stream crossing at a relative angle $\alpha_{rel} = \alpha_p - \theta_j = 2(\alpha_i - \theta_j)$. The solution to this problem is found by solving the case of two impacting planar jets of finite breadth and then extrapolating the solution to the asymptotic case where one of the breadths tends to infinity (see Figure 7.15). The solution to the problem of two streams of finite breadth mentioned above can be solved by using the formula of Schwarz applied to the holomorphic function $-i\omega$ (where ω is the complex potential $\phi + i\psi$, U is the oncoming velocity magnitude, and ν is the complex velocity $Ue^{-i\theta}$) [36](pp 299).

$$-i\omega = \frac{1}{2\pi} \int_0^{2\pi} \psi(\theta) \frac{Ue^{i\theta} + \nu}{Ue^{i\theta} - \nu} d\theta \quad (7.19)$$

In particular, for two incoming jets A_1 and A_2 , (of breadths h_1 and h_2 re-

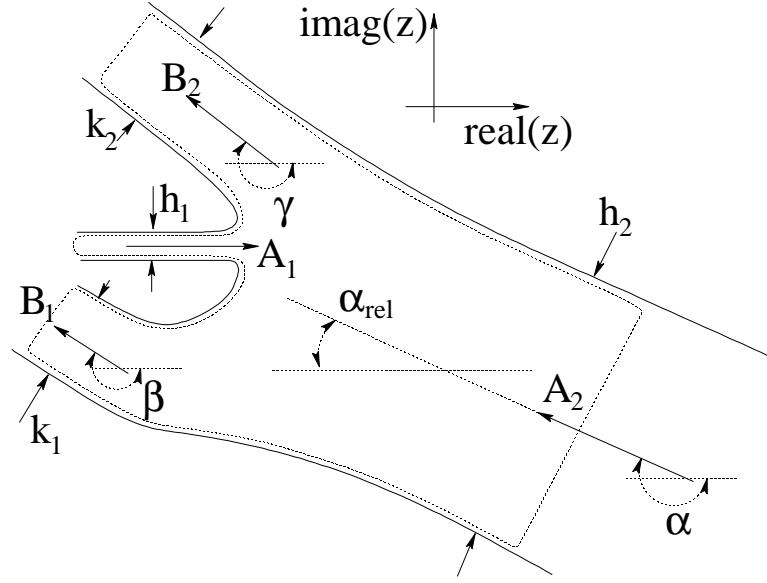


Figure 7.15: Two jets of finite breath plunging into each other

spectively) that impact into each other and subsequently produce two outgoing streams B_1 and B_2 (with breaths k_1 and k_2), the formula of Schwarz gives the following parametric equations in θ for the shape of the free streamlines,

$$\begin{aligned}
 x(\theta) + iy(\theta) = & \frac{U}{\pi} \left\{ \frac{h_1}{a_1} \log \left(1 - \frac{\nu}{a_1} \right) + \frac{h_2}{a_2} \log \left(1 - \frac{\nu}{a_2} \right) \right\} \\
 & - \frac{U}{\pi} \left\{ \frac{k_1}{b_1} \log \left(1 - \frac{\nu}{b_1} \right) + \frac{k_2}{b_2} \log \left(1 - \frac{\nu}{b_2} \right) \right\} \quad (7.20)
 \end{aligned}$$

where $a_1 = U$, $a_2 = Ue^{i\alpha}$, $b_1 = Ue^{i\beta}$, $b_2 = Ue^{i\gamma}$ and $-\alpha$, $-\beta$ and $-\gamma$ are the asymptotic directions of A_2 , B_1 and B_2 (A_1 is parallel to the real axis). $\log()$ is the natural logarithm, and θ is taken to range from 0 to 2π .

Also, by applying conservation of momentum to the control volume confined

by the dashed line in Figure 7.15, one obtains,

$$h_1 + h_2 \cos \alpha - k_1 \cos \beta - k_2 \cos \gamma = 0 \quad (7.21)$$

$$h_2 \sin \alpha - k_1 \sin \beta - k_2 \sin \gamma = 0 \quad (7.22)$$

These expressions were calculated knowing that the outgoing velocity is also U since all the free streamlines are subjected to the ambient pressure, which forces the velocity magnitude to be constant regardless of the local shape or orientation in the absence of gravity.

Lastly, applying conservation of mass gives the constraint,

$$h_1 + h_2 = k_1 + k_2 \quad (7.23)$$

The four unknowns k_1 , k_2 , β and γ are only conditioned by three algebraic equations (Equations 7.21 thru 7.23), thus making the general problem of two impinging jets of arbitrary angle undetermined. In the case of the plunging jet problem, there is an additional constraint that needs to be fulfilled, since far from the jet the receiving liquid of the pool is at rest in an absolute reference frame. This implies that B_1 and B_2 should be parallel to the incoming stream A_2 in a reference frame fixed with the jet tip,

$$\beta = \gamma = \alpha = \alpha_{rel} + \pi \quad (7.24)$$

as h_2 tends to infinity.

With this additional constraint, the momentum equations reduce to,

$$h_1 + h_2 \cos \alpha_{rel} - (k_1 + k_2) \cos \alpha_{rel} = 0 \quad (7.25)$$

$$h_2 \sin \alpha_{rel} - (k_1 + k_2) \sin \alpha_{rel} = 0 \quad (7.26)$$

where it can be seen that the final result of the problem is unchanged if k_1 is replaced by k_2 and vice versa. This equivalence implies that

$$k_1 = k_2 = k = \frac{h_1 + h_2}{2} \quad (7.27)$$

based on the conservation of mass (Equation 7.23), and also satisfies the conservation of momentum (Equations 7.25 and 7.26) in the limit $h_1/h_2 \rightarrow 0$.

The shapes of the free streamlines were computed numerically for fixed values of $h_1 = T_j$ and increasing values of h_2 until enough convergence to the asymptotic solution was achieved. The specific procedure used to check for the convergence of the solution is described in the following.

As mentioned above, the value of h_1 was fixed to T_j , while the value of h_2 was increased until convergence was achieved. For a given finite h_2 , a non-linear optimizer was prompted to calculate values for β and γ which satisfy the momentum equations (expressions 7.25 and 7.26), the continuity equation (expression 7.23) and condition 7.27. In order to satisfy these conditions, the optimizer was programmed to calculate these angles using an iterative process in which the values of β and γ were varied around the asymptotic value $\alpha_{rel} + \pi$ until the continuity equation and condition 7.27 were satisfied. To verify these conditions, the values of k_1 and k_2 were calculated from Equations 7.25 and 7.26, therefore satisfying conservation of momentum. As it was shown, the resulting values of β and γ given by the optimizer satisfy all the required conditions of the asymptotic solution except for $\beta = \gamma = \alpha_{rel} + \pi$, which is in general not true if h_2/h_1 is not large

enough. The values of β and γ given by the optimizer were observed to converge to $\alpha_{rel} + \pi$ as h_2 was increased. For $h_2/h_1 = 10^6$, the resulting β and γ given by the optimizer are nearly identical to $\alpha_{rel} + \pi$ for all the jet conditions presented in this thesis, and therefore it was used to perform the calculations shown in the following sections. Figure 7.16 illustrates with one example, the convergence of β and γ as h_2/h_1 is increased.

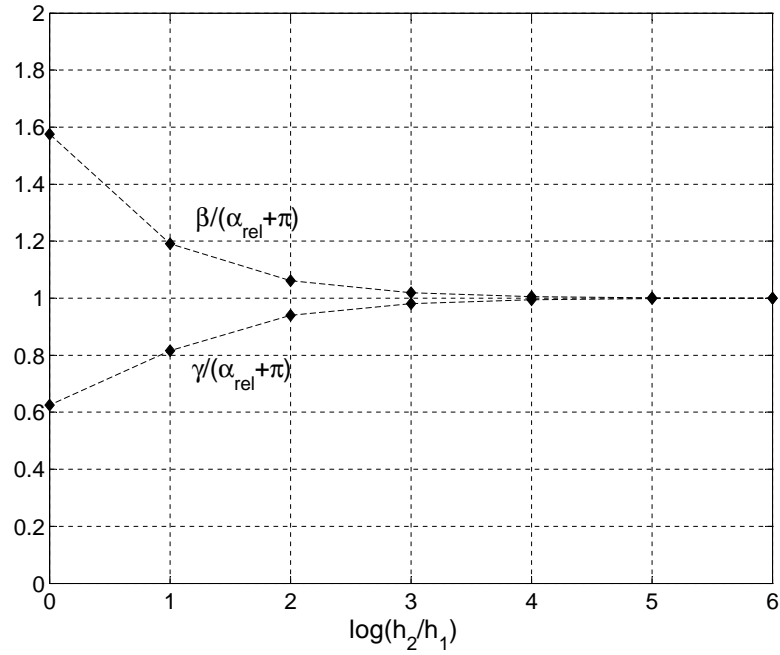


Figure 7.16: Convergence of β and γ for increasing values of h_2/h_1 . $\theta_j = 29.5^\circ$, $V_t/V_j = 0.07$.

Figure 7.17 shows the computed shapes of the underwater craters for a jet with $\theta_j = 20^\circ$ and two translating velocities: $V_t/V_j = 0.0$ and $V_t/V_j = 0.1$.

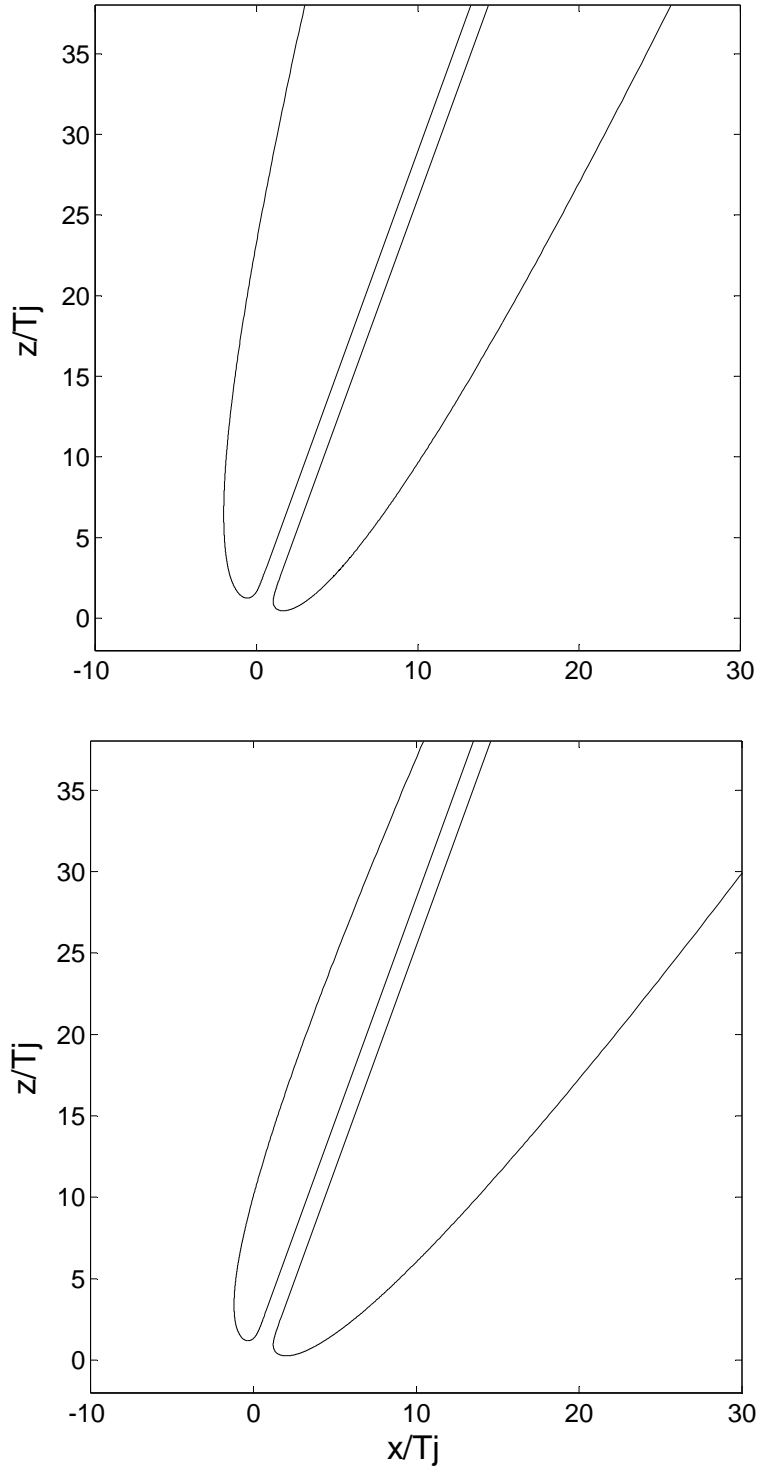


Figure 7.17: Shape of the underwater craters computed using the formula of Schwarz without gravity. $\theta_j = 20^\circ$, $V_t/V_j = 0.0$ (top). $V_t/V_j = 0.1$ (bottom). Jet translating from right to left.

7.3 The Roles of Gravity and Inertia - Velocity of Collapse

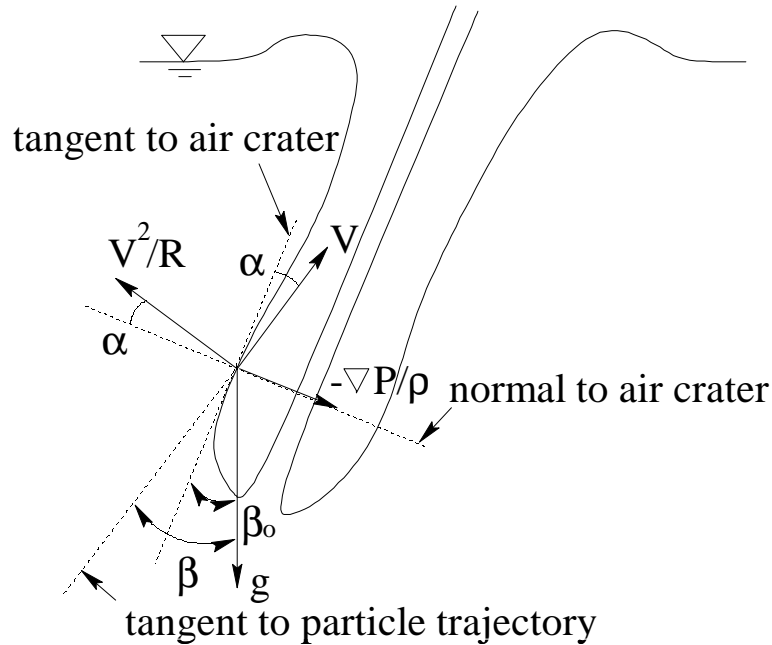


Figure 7.18: Free-body diagram of the accelerations acting on a particle situated at the air-water interface viewed from the steady reference frame fixed to the jet tip

In this section, the roles of the water inertia and the acceleration of gravity in the dynamics of the crater collapse are discussed. The accelerations acting on a fluid particle situated at one of the crater walls can be expressed in terms of the pressure gradient acting normal to the air-water interface, the centrifugal acceleration acting normal to the particle trajectory and the gravitational acceleration in the vertical direction. A schematic of these accelerations in a reference frame

fixed to the underwater jet tip, is shown in Figure 7.18 where V is the particle velocity, ∇P the local pressure gradient, ρ the water density, R the radius of curvature of the particle trajectory, α the angle between the particle trajectory and the local tangent to the crater wall, β the angle between the particle trajectory and the vertical and β_o the angle between the local tangent to the crater wall and the vertical. For a differential displacement of the particle ds , the positive work of all the forces that act in the direction of the particle trajectory translates into an increase of the kinetic energy of the particle. Mathematically, this can be expressed as:

$$d\left(\frac{V^2}{2}\right) = -\left(\frac{\nabla P}{\rho} \sin(\alpha) + g \cos(\beta)\right) ds \quad (7.28)$$

The pressure gradient term of this equation can be expressed as a function of V , R , β , α and g by using the momentum equation applied to the fluid particle in the normal direction to the crater.

$$-\frac{\nabla P}{\rho} = \frac{1}{\cos(\alpha)} \left(\frac{V^2}{R} - g \sin(\beta)\right) \quad (7.29)$$

Plugging 7.29 into 7.28,

$$\frac{d}{ds} \left(\frac{V^2}{2}\right) = -\left[\tan(\alpha) \left(g \sin(\beta) - \frac{V^2}{R}\right) + g \cos(\beta)\right] \quad (7.30)$$

Equation 7.30 gives the change in kinetic energy of the particle in terms of the particle velocity and direction (V and β), the radius of curvature of the particle trajectory (R), gravity (g) and the angle between the particle trajectory and

the crater wall (α). It is interesting to note that in the absence of gravity, Equation 7.30 reduces to,

$$\frac{d}{ds} \left(\frac{V^2}{2} \right) = -\tan(\alpha) \left(\frac{V^2}{R} \right) \quad (7.31)$$

which shows that when $\alpha = 0$ (i.e. the particle velocity is tangent to the crater wall) then $dV^2/ds = 0$, which is also true in the non-gravitational solution presented in section 7.2, where the particles at the air water interface have constant velocity and the crater maintains the steady state shape.

In order to obtain qualitative information on the physics of the crater collapse under the effect of gravity, the right-hand side of Equation 7.30 can be linearized assuming that the particle velocity at the air-water interface is composed of a constant component tangent to the crater wall V_o (the same as in the non-gravitational case) plus a small gravity-induced perturbation with two components: v' perpendicular to the crater and δV_o parallel to V_o . The small velocity perturbation requirement can be used to help linearize this term by expanding the following expressions in a Taylor series up to first order.

$$\tan(\alpha) = \tan\left(\frac{v'}{V_o + \delta V_o}\right) \approx \frac{v'}{V_o} \approx \alpha \quad (7.32)$$

$$\sin(\beta) = \sin(\beta_o + \alpha) \approx \sin(\beta_o) + \alpha \cos(\beta_o) \quad (7.33)$$

$$\cos(\beta) = \cos(\beta_o + \alpha) \approx \cos(\beta_o) - \alpha \sin(\beta_o) \quad (7.34)$$

$$\frac{d}{ds} = \frac{d}{ds_o} \frac{ds_o}{ds} = \frac{d}{ds_o} \cos(\alpha) \approx \frac{d}{ds_o} \quad (7.35)$$

where ds_o is the arc-length along the crater wall. Also, the radius of curvature of

the particle trajectory R is expected to be close to the radius of curvature of the crater wall since α is small and therefore, R can be expressed as the local radius of curvature of the crater wall R_o plus a small amount R' obtaining the following first order expression for the centrifugal acceleration,

$$\frac{V^2}{R} \approx \frac{V_o^2}{R_o} \left[\frac{1 + 2(\delta V_o/V_o)}{1 + (R'/R_o)} \right] \approx \frac{V_o^2}{R_o} \left(1 - \frac{R'}{R_o} + 2\frac{\delta V_o}{V_o} \right) \quad (7.36)$$

Expressions 7.32 to 7.36 can be plugged into Equation 7.30 to obtain a new expression of the energy equation where the right-hand side is linear.

$$\frac{d}{ds_o} \left(\frac{V^2}{2} \right) = \frac{V_o^2}{R_o} \left(\frac{v'}{V_o} \right) - g \cos(\beta_o) \quad (7.37)$$

This form of the energy equation is conveniently expressed in terms of geometrical parameters of the crater instead of the properties of the particle trajectory. Also, by realizing that $dz = -ds_o \cos(\beta_o)$, where z is the local depth at the particle location, it is obtained,

$$\frac{d}{dz} \left(\frac{V^2}{2} \right) + \frac{V_o^2}{\cos(\beta_o)R_o} \left(\frac{v'}{V_o} \right) - g = 0 \quad (7.38)$$

that gives a first order approximation of the kinetic energy changes seen by the particle as a function of V_o , the local depth z , g and geometrical parameters of the crater wall (β_o and R), or in non-dimensional terms:

$$\frac{d\bar{V}^2}{d\bar{z}} + \frac{Fr_o^2}{\cos(\beta_o)} \bar{v} - 1 = 0 \quad (7.39)$$

where $Fr_o = V_o/\sqrt{gR_o}$, $\bar{v} = v'/V_o$, $\bar{V} = V/V_o$ and $\bar{z} = 2zg/V_o^2$. Expression 7.39 is used in the following to discuss the different roles played by the inertia and the acceleration of gravity during the crater collapse process at different locations along the crater wall.

In particular, if $Fr_o^2/\cos(\beta_o)$ is of the order of one or less, that is in the moderate curvature regions far from the jet tip and where the crater walls are approximately vertical, the term $Fr_o^2/\cos(\beta_o)\bar{v}$ becomes very small and equation 7.39 reduces to,

$$\frac{d\bar{V}^2}{d\bar{z}} - 1 = 0 \quad (7.40)$$

with solution

$$V(z) = \sqrt{V^2(0) + 2gz} \quad (7.41)$$

Or in other words, in the regions away from the jet tip, gravity induces a perturbation on the particle velocity which is responsible for the crater collapse, giving an overall particle velocity that increases with depth like $\sqrt{2gz}$.

Contrarily, close to the jet tip, the craters show large radius of curvature and the tangent line to the craters is almost horizontal ($\beta \approx 90^\circ$). In other words, the non-dimensional parameter $Fr_o^2/\cos(\beta_o)$ is large. In the limiting case where $Fr_o^2/\cos(\beta_o)$ is so large that $Fr_o^2/\cos(\beta_o)\bar{v}$ tends to infinity, expression 7.39 can be simplified to the following homogeneous equation,

$$-\frac{d\bar{V}^2}{d\bar{z}} \approx \frac{Fr_o^2}{\cos(\beta_o)}\bar{v} \gg 1 \quad (7.42)$$

These regions see a strong gradient in V which decreases rapidly with depth. Therefore, the portion of the particle velocity that is allowed to vary as the particle translates (the gravity-induced perturbation) is expected to be much smaller in the region near the jet tip than in other regions of the crater. The observations of the high-speed movies shown in Chapter 5 agree with these findings and the region of the craters close to the jet tip was observed to remain virtually unchanged during the entire collapse process and seems to be unaffected by the presence of gravity.

7.4 Temporal Evolution of the Underwater Craters

- Pinch-off Time and Depth

The results of Sections 7.1 thru 7.3 are combined here to obtain simple scaling arguments to estimate the shape of the underwater craters as a function of time and ultimately, the time and location where the crater wall first touches the underwater jet (pinch-off).

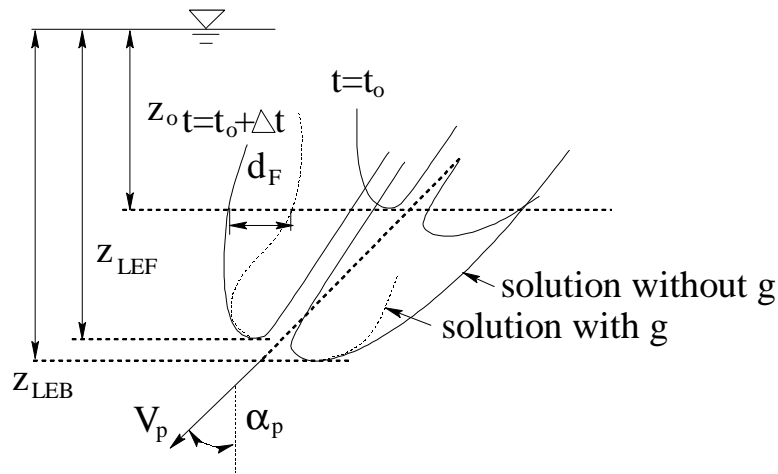


Figure 7.19: Schematic of the gravitational and non-gravitational shapes of the underwater craters.

Figure 7.19 shows a schematic of the underwater plunging jet translating from right to left whose velocity and direction of penetration in a reference frame fixed with respect to the receiving pool (V_p and α_p) are given by expressions 7.12 and 7.14. The solid line represents the shape of the underwater craters as predicted by the non-gravitational theory described in section 7.2, while the dashed line depicts the solution under the influence of a gravitational acceleration. Ex-

pressions 7.12 and 7.14 are valid for the gravitational and non-gravitational solutions and therefore, for both solutions the jet leading edge is expected to be at the same location. As time progresses, the crater shapes given by these solutions diverge due to the gravity-induced deformations taking place on the submerged interface for the gravitational case. As it was seen in section 7.3, the important gravity-induced deformations experienced by the crater take place in the moderate curvature regions. Due to the moderate values of curvature of these regions, the gravity-induced perturbation parallel to the crater (δV_o) plays a secondary role in determining the shape of the gravity-deformed crater (note that in the limiting case of zero curvature, δV_o would produce no deformation) . Therefore, a good first approximation to the deformation of the crater under the effects of gravity can be achieved by accounting only for the effects of the gravity-induced deformation velocity perpendicular to the crater wall (v').

Let $d_F(z_o, t)$ be the difference in horizontal position of the front crater predicted by the gravitational and non-gravitational theories at a given depth z_o , as shown in the figure. Let also z_{LEF} be the depth of the leading edge of the front crater at time equal t , and t_o the time at which the front leading edge was at $z_o < z_{LEF}$. d_F can be estimated by integrating the horizontal projections of all the infinitesimal deformations seen by the particle of the front leading edge crater situated at z_o between the times t_o and t .

$$d_F(z_o, t) = \int_{t_o}^t v'(z_o, t) \cos \beta_o^F(z_o, t) dt \quad (7.43)$$

where v' is the gravity-induced velocity of deformation of the particles perpendicular to the front crater, and β_o^F is the angle between the tangent line to the

front crater and the vertical at z_o (see section 7.3).

Equation 7.41 gives an expression for the magnitude of the particle velocity in the limiting case where the inertial effects are unimportant. In this limiting case, if the velocity changes in the direction parallel to the crater wall were identically equal to zero ($\delta V_o = 0$), Equation 7.41 would predict a scaling for v' equal to $\sqrt{2gz}$. In other words, v' should scale like $\sqrt{2gz}$ in absence of any dominant inertial effects (for example in the small radius of curvature region near the leading edge of the crater), and if the gravity-induced variations in kinetic energy of the particles at the crater were directed exclusively in the direction perpendicular to the crater. On the contrary, inertia is not exactly zero (in fact, is dominant in the regions near the jet tip) and a portion of the kinetic energy changes of the particles may be translated, as well, into velocity changes along the crater wall. These two effects contribute simultaneously to reduce the magnitude of v' from what it would be expected under the former hypothesis. Therefore, $\sqrt{2gz}$ should be an upper bound for v' in the real problem. For the purpose of this model, a scaling for v' equal to $\lambda\sqrt{gz}$ is proposed, where λ is a non-dimensional number of order one that is to be found by correlations with the experimental data. For the reasons explained above, the best match with the experimental data is expected to be found for a value of λ smaller than $\sqrt{2}$.

Using $v' = \lambda\sqrt{gz}$, expression 7.43 can be written as follows,

$$d_F(z_o, t) \approx \lambda\sqrt{gz_o} \int_{t_o}^t \cos \beta_o^F(z_o, t) dt \quad (7.44)$$

If β_o^F is approximated by the values of the non-gravitational solution at each

time and realizing that $dt = -dz/(V_p \cos \alpha_p)$, this expression can be translated into an integral in space,

$$d_F(z_o, t) \approx \frac{\lambda \sqrt{gz_o}}{V_p \cos \alpha_p} \int_{z_o}^{z_{FLE}(t)} \cos \beta_o^F(z) dz \quad (7.45)$$

Similarly, for the back crater,

$$d_B(z_o, t) \approx \frac{\lambda \sqrt{gz_o}}{V_p \cos \alpha_p} \int_{z_o}^{z_{BLE}(t)} \cos \beta_o^B(z) dz \quad (7.46)$$

In conclusion, the resulting shape for the craters at a given time t can be estimated by using the non-gravitational shape of the craters (section 7.2) corrected by Equations 7.45 and 7.46. For the results presented herein, the integrations were performed numerically using the trapezoidal rule.

For each jet condition and translating velocity, the shape of the underwater craters was computed in time increments of 4 *ms* until the minimum distance between the air craters and the jet center line was less than or equal to $0.5T_j$ thus giving a theoretical prediction of the pinch-off time and the pinch-off depth. The experimental pinch-off times and depths for conditions I, III, IV, V and VI were best fitted for $\lambda_{opt} = 0.56$. This value was found by minimizing the following function,

$$R(\lambda) = \sqrt{\frac{\sum [1 - \tau_{po,i}^{theo}(\lambda)/\tau_{po,i}^{exp}]^2 + \sum [1 - \delta_{po,i}^{theo}(\lambda)/\delta_{po,i}^{exp}]^2}{n}} \quad (7.47)$$

where $\tau_{po,i}^{exp}$ and $\delta_{po,i}^{exp}$ are the non-dimensional pinch-off time and depth for a given jet condition and translation velocity, and $\tau_{po,i}^{theo}(\lambda)$ and $\delta_{po,i}^{theo}(\lambda)$ are their equiv-

alent theoretical predictions for a given value of λ . The sums go over all the translation velocities and jet conditions except for condition II (which is out of the range of validity of this model as explained later). The number n is the total number of combinations of jet translation velocities and jet conditions. In this case, $n = 25$. Figure 7.20 shows R as a function of λ around the optimum to illustrate the sensitivity of the model to λ .

The comparison of the experimental and theoretical values is shown in Figures 7.21 thru 7.25.

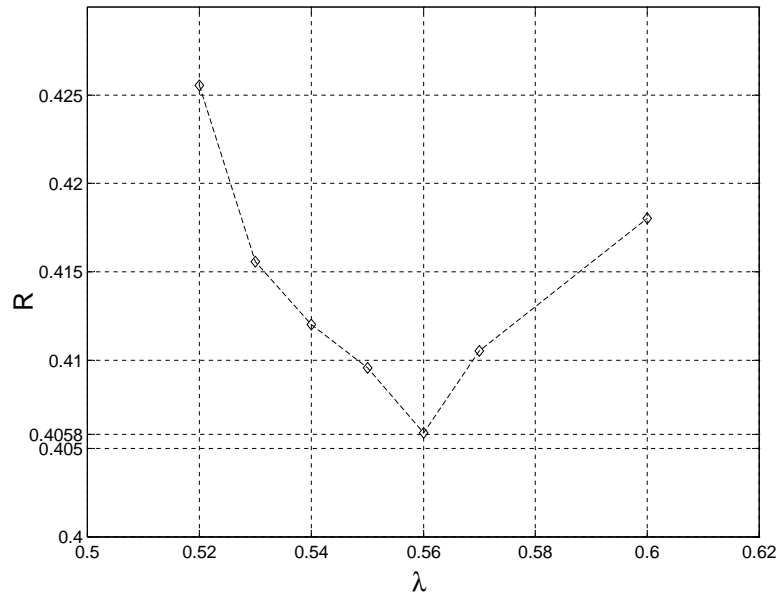


Figure 7.20: R as a function of λ around λ_{opt}

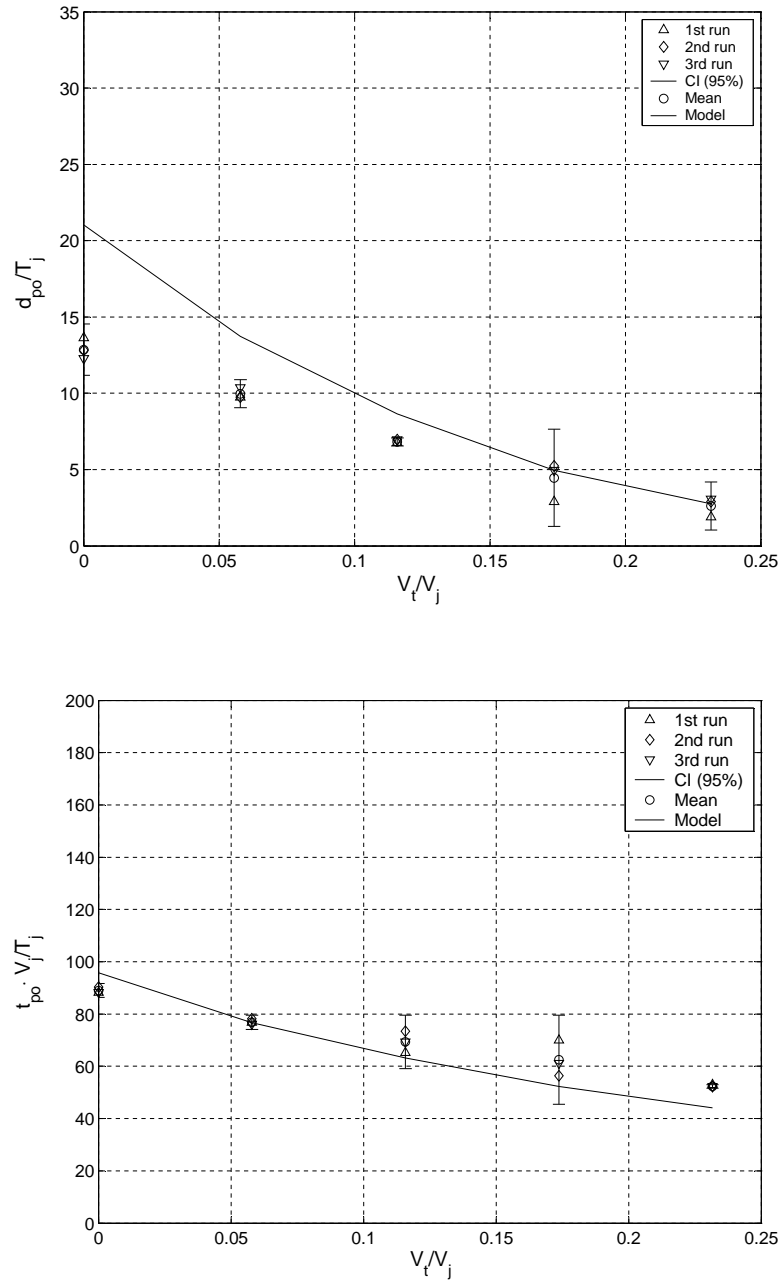


Figure 7.21: Pinch-off depths (top) and times (bottom) for jet condition I as a function of translating speed. The solid line is the theoretical prediction, and the dots are the experimental values

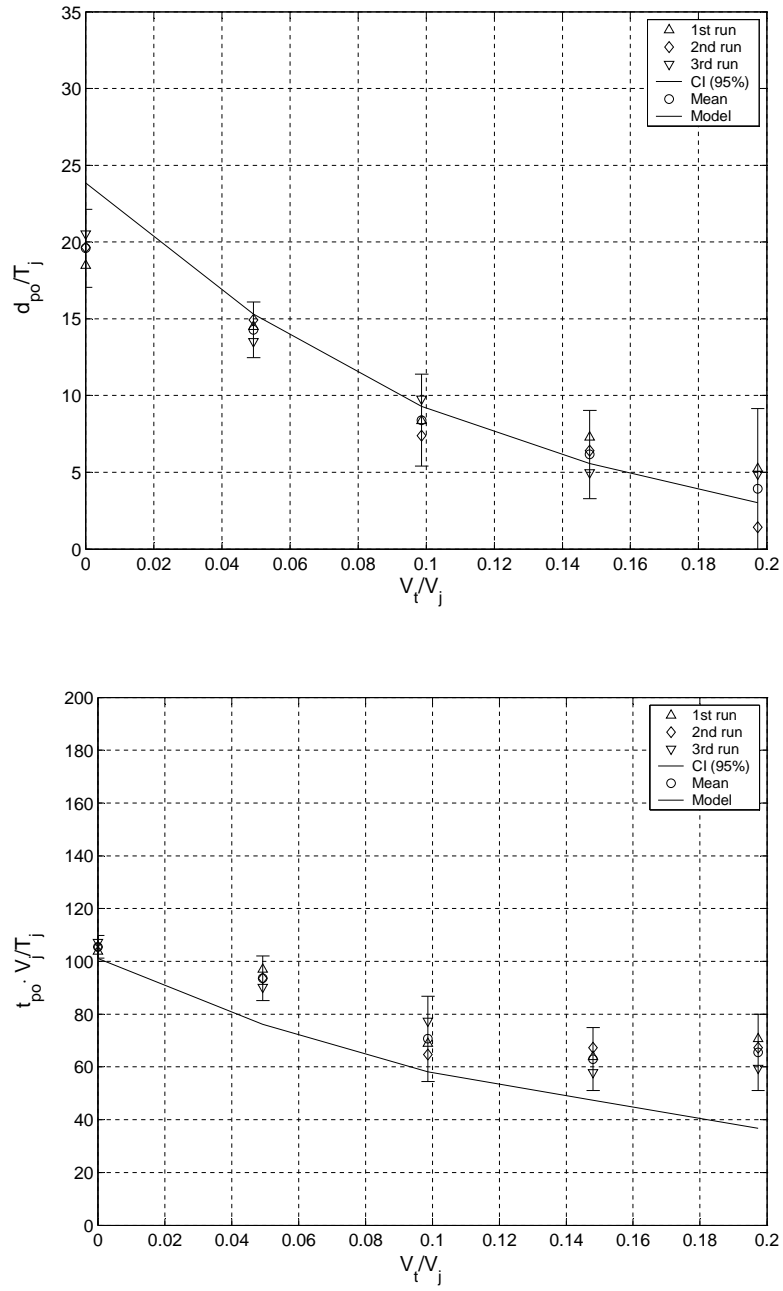


Figure 7.22: Pinch-off depths (top) and times (bottom) for jet condition III as a function of translating speed. The solid line is the theoretical prediction, and the dots are the experimental values

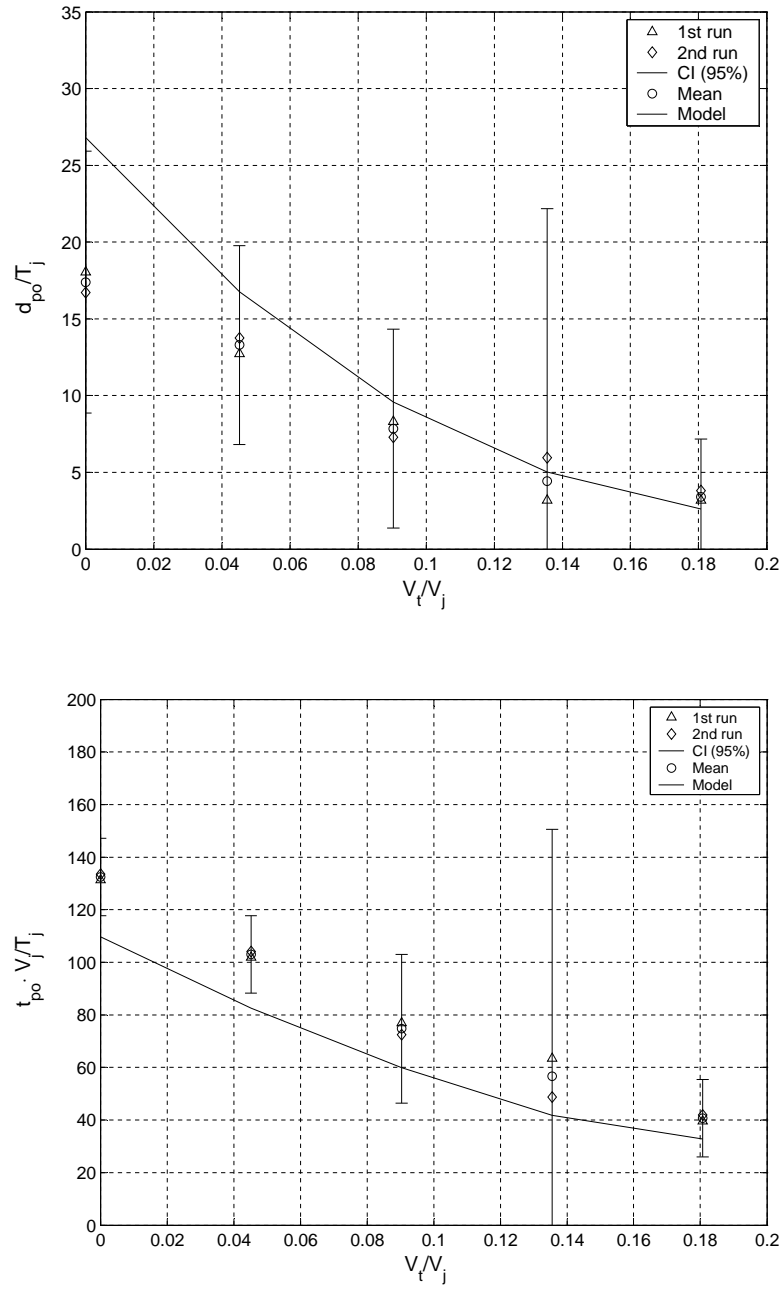


Figure 7.23: Pinch-off depths (top) and times (bottom) for jet condition IV as a function of translating speed. The solid line is the theoretical prediction, and the dots are the experimental values

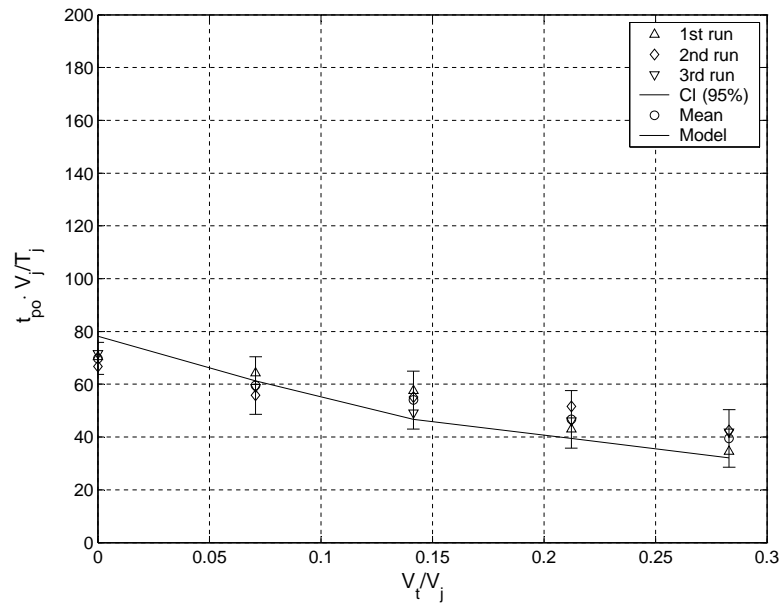
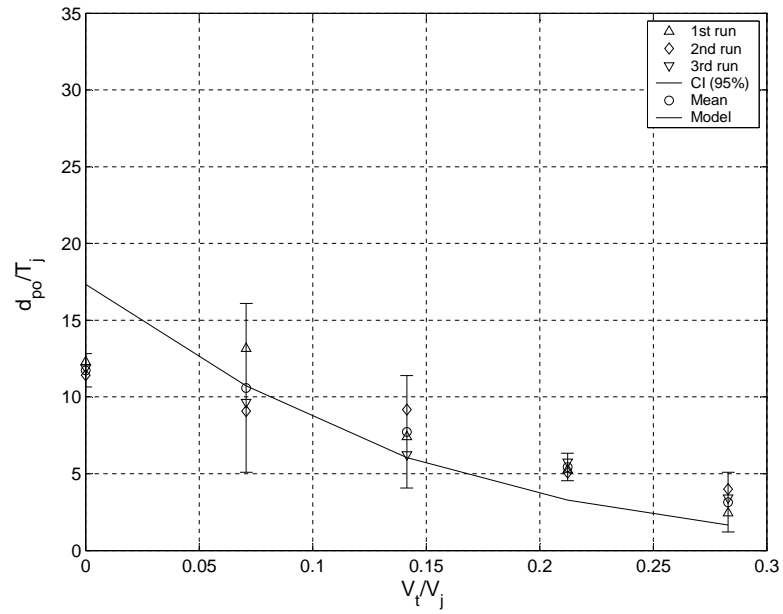


Figure 7.24: Pinch-off depths (top) and times (bottom) for jet condition V as a function of translating speed. The solid line is the theoretical prediction, and the dots are the experimental values

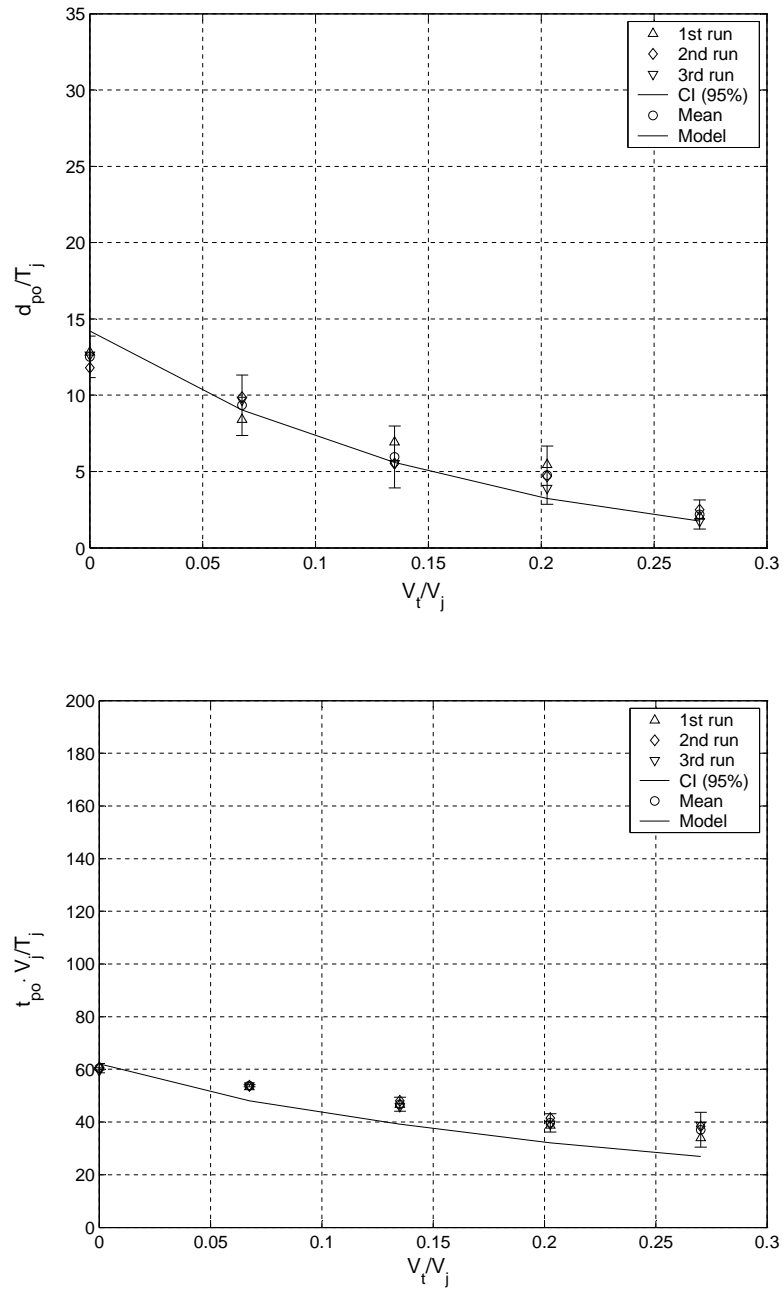


Figure 7.25: Pinch-off depths (top) and times (bottom) for jet condition VI as a function of translating speed. The solid line is the theoretical prediction, and the dots are the experimental values

The model predicts well the trends of the pinch-off times and depths as a function of translating speed for conditions I, III, IV, V and VI. However, the model slightly overpredicts the dependency of these quantities with the translation speed. The high-speed movies reveal that for the longest pinch-off times (slowest translating jets), the upstream splash has enough time to complete roughly half a wave period in which it forms and then accelerates downwards onto the water free surface, presumably resulting into a slight acceleration of the collapse process. On the other hand, for the cases where the pinch-off times are shorter, (faster translating jets), the pinch-off was observed to occur while the upstream splash is forming. At these early stages of the flow development, the splash experiences strong vertical accelerations which may have some effect on the front crater wall leading to a slight delay in the pinch-off event.

For condition II, the model is not in good agreement with the observations as can be seen in Figure 7.27. The jet inclination θ_j for conditions I, III, IV, V and VI, ranges from 7.1 to 32.5 degrees while the jet inclination for condition II is $\theta_j = 45.2$ degrees, this being the largest value. It is speculated that for large angles of inclination, the collapse process may be dominated by the dynamics of the free surface voiding the basic assumptions of this model.

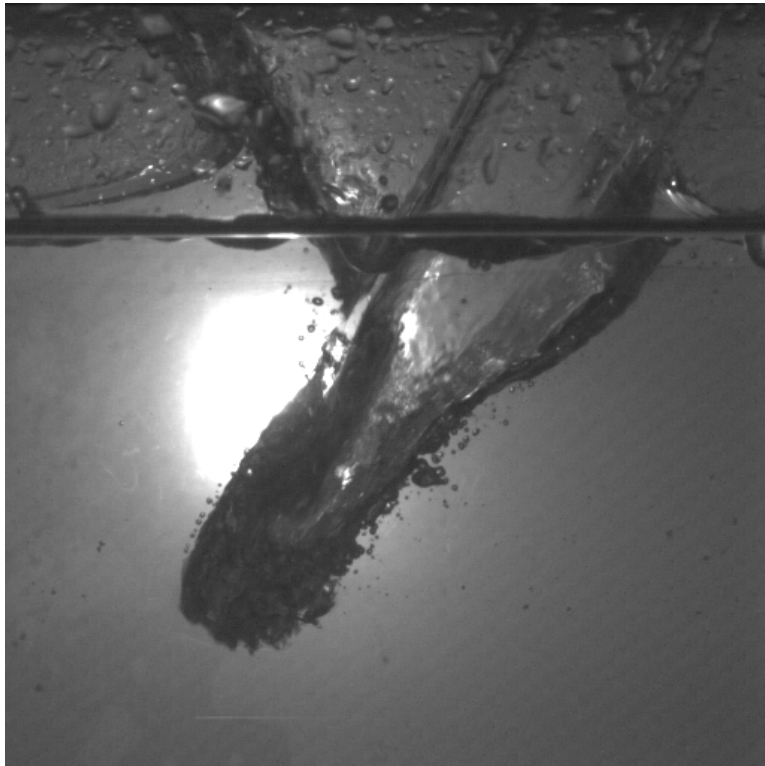


Figure 7.26: Jet condition II, $V_t = 0.30 \text{ m/s}$ and $t = \text{pinch-off}$

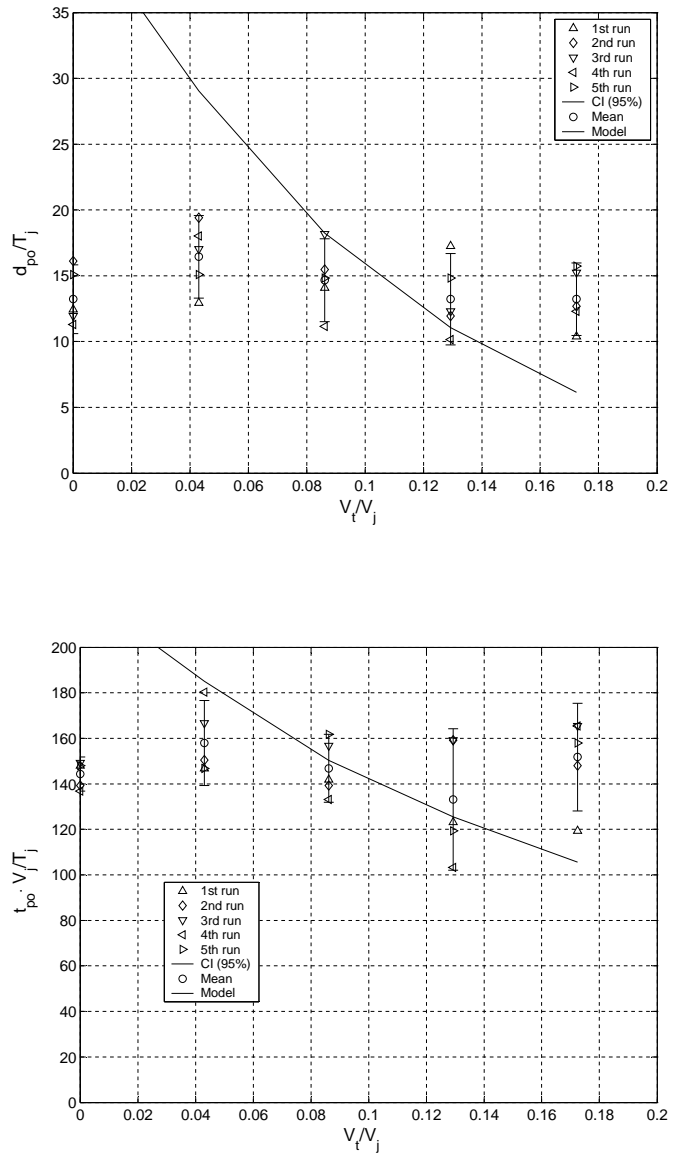


Figure 7.27: Pinch-off depths (top) and times (bottom) for jet condition II as a function of translating speed. The solid line is the theoretical prediction, and the dots are the experimental values. It is speculated that the model is not in good agreement with the experiments for this condition due to the free surface effects that appear for large jet inclination angles θ_j .

It is interesting to note that for this condition, the pinch-off time is approximately independent of translation speed. In the movies of condition II, it appears that the pinch-off event is accelerated by the weight of water of the front splash when it falls back onto the free surface, and therefore, it may be that this constant pinch-off time has some relation with some characteristic time associated with the splash formation. In order to explore this hypothesis, the period of the waves produced by a stationary local impulse on the water free surface is calculated in the following. Linear potential wave theory gives an expression for the local elevation of the free surface due to a concentrated impulse [37] and valid for large $gt^2/2x$,

$$\eta = \frac{g^{1/2}t^2}{2^{5/2}\pi^{1/2}\rho x^{5/2}}(\cos\frac{gt^2}{4x} - \sin\frac{gt^2}{4x}) \quad (7.48)$$

where g is gravity, t is time, x is distance from the impulse location and ρ is the water density. The water elevation is zero initially, and it will be zero again at x after a time T which has to satisfy,

$$\frac{gT^2}{4x} = \frac{\pi}{4} \quad (7.49)$$

In other words, the characteristic time T associated to the splash formation and splash fall back is of the order of,

$$T = \sqrt{\frac{\pi x}{g}} \quad (7.50)$$

Or in non-dimensional terms,

$$\frac{TV_j}{T_j} = Fr_j \sqrt{\frac{\pi x}{T_j}} \quad (7.51)$$

Figure 7.28 shows T as a function of x for condition II (Fr_j equal to 21). It can be seen that TV_j/T_j is of the order of the non-dimensional pinch-off time (≈ 140) in the neighboring areas of the jet impact site which supports the idea

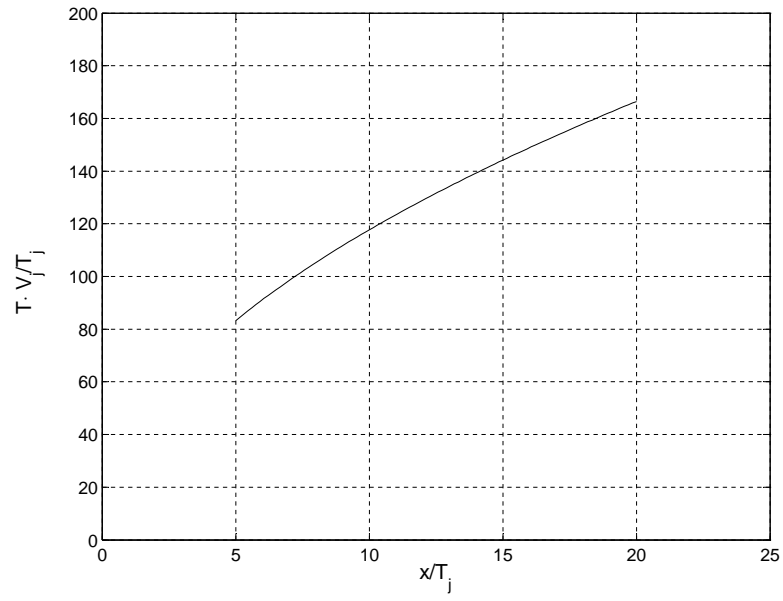


Figure 7.28: Non-dimensional period associated to the splashes for condition II

that for large inclination angles, the collapse time may be associated with the characteristic time of the resulting splashes.

7.5 Underwater Crater Contours

For all the jet conditions except for condition II, the shapes of the underwater craters computed with the model resemble the actual crater shapes measured in the experiments. In order to qualitatively show this resemblance, the crater walls seen in the movies were digitized by obtaining with the computer mouse the coordinates of collections of points along the crater walls (about 50 points per frame). The underwater jet edges were also digitized, when visible, and are presented along with the digitized shapes of the crater walls. The positions of the digitized jet edges, however, should be regarded as qualitative since it is typically hard to accurately identify the exact position of the jet edges on the movie frames.

Figures 7.29 through 7.34 show sequences of the digitized shapes along with their equivalent model predicted contours. The results are presented in a reference frame that is translating with the jet carriage. Each individual figure shows four contours for the same jet condition and translation velocity at four different instants in time ($1/4t_{po}$, $1/2t_{po}$, $3/4t_{po}$ and t_{po}) where t_{po} is the measured pinch-off time.

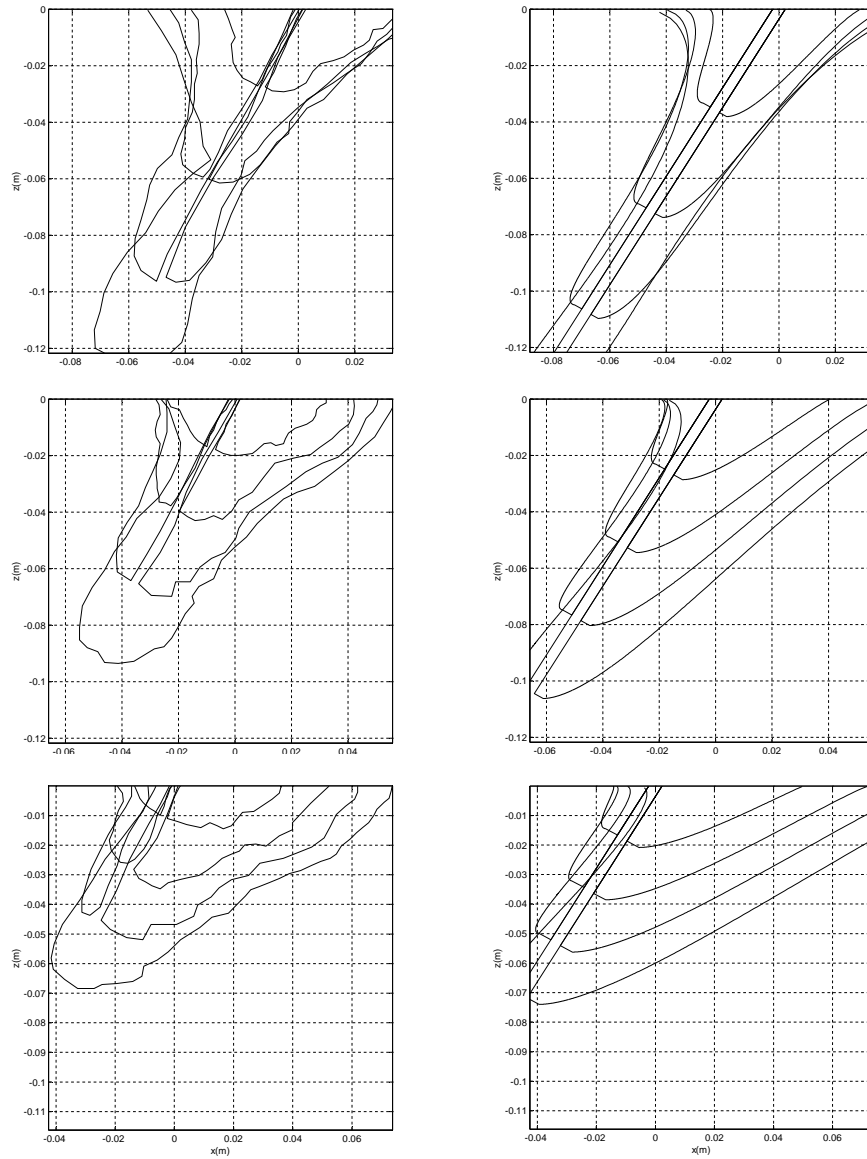


Figure 7.29: Crater temporal evolution for jet condition I ($Fr_j = 13.6, \theta_j = 32.5^\circ$). Measured values on left column for jet translating from right to left at $V_t = 0.00$ m/s (top), $V_t = 0.30$ m/s (middle) and $V_t = 0.60$ m/s (bottom). The contours are given in a reference frame moving with the jet carriage, and correspond to four equally spaced times between the jet impact and t_{po} . The contours on the right column were computed with the theoretical model for the same jet conditions and times as the experimental data.

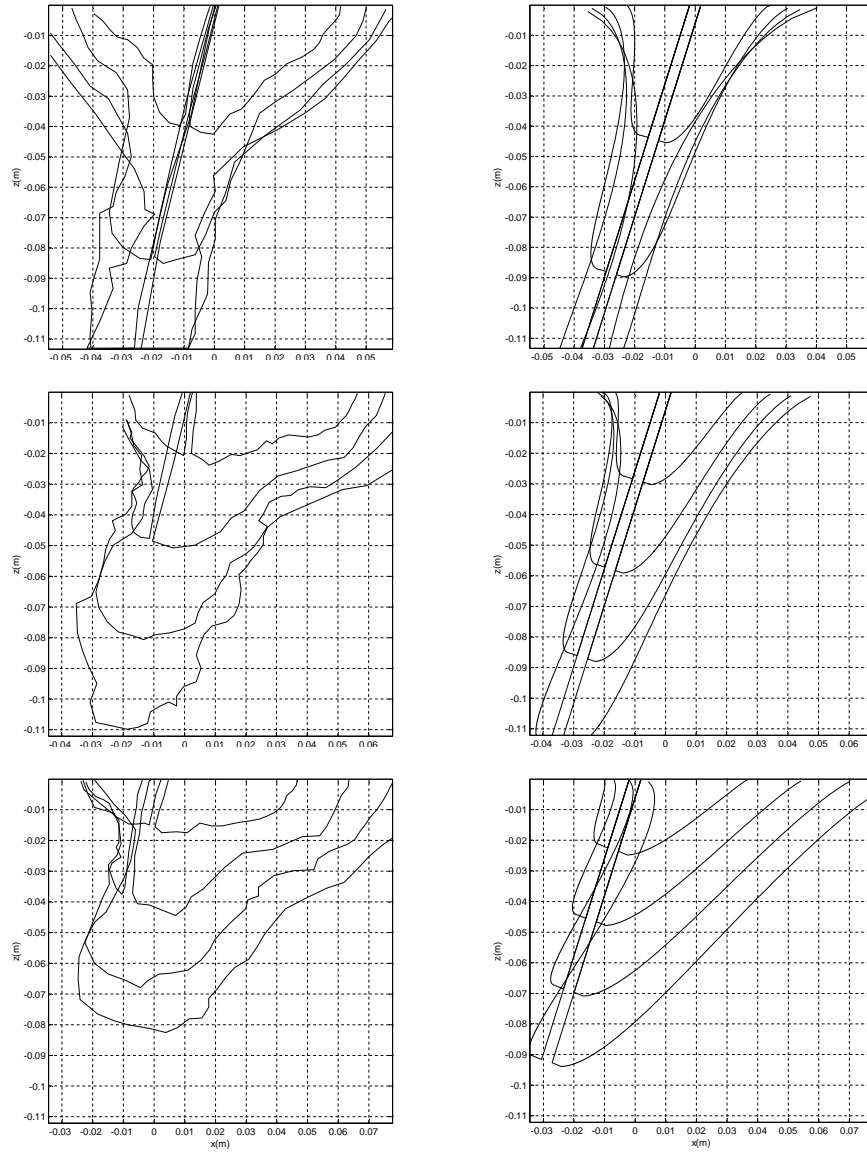


Figure 7.30: Crater temporal evolution for jet condition III ($Fr_j = 16.2, \theta_j = 17.4^\circ$). Measured values on left column for jet translating from right to left at $V_t = 0.00\text{m/s}$ (top), $V_t = 0.30\text{ m/s}$ (middle) and $V_t = 0.60\text{ m/s}$ (bottom). The contours are given in a reference frame moving with the jet carriage, and correspond to four equally spaced times between the jet impact and t_{po} . The contours on the right column were computed with the theoretical model for the same jet conditions and times as the experimental data.

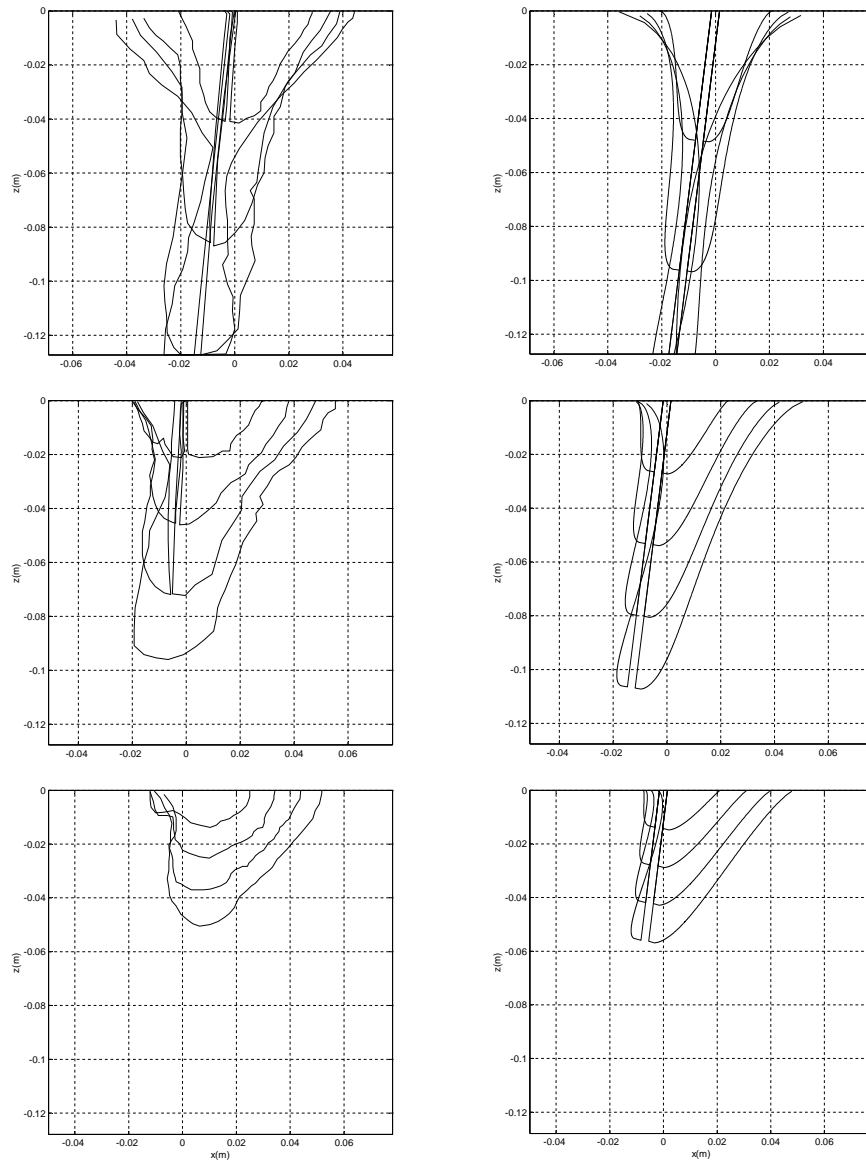


Figure 7.31: Crater temporal evolution for jet condition IV ($Fr_j = 19.7, \theta_j = 7.1^\circ$). Measured values on left column for jet translating from right to left at $V_t = 0.00 \text{ m/s}$ (top), $V_t = 0.30 \text{ m/s}$ (middle) and $V_t = 0.60 \text{ m/s}$ (bottom). The contours are given in a reference frame moving with the jet carriage, and correspond to four equally spaced times between the jet impact and t_{po} . The contours on the right column were computed with the theoretical model for the same jet conditions and times as the experimental data.

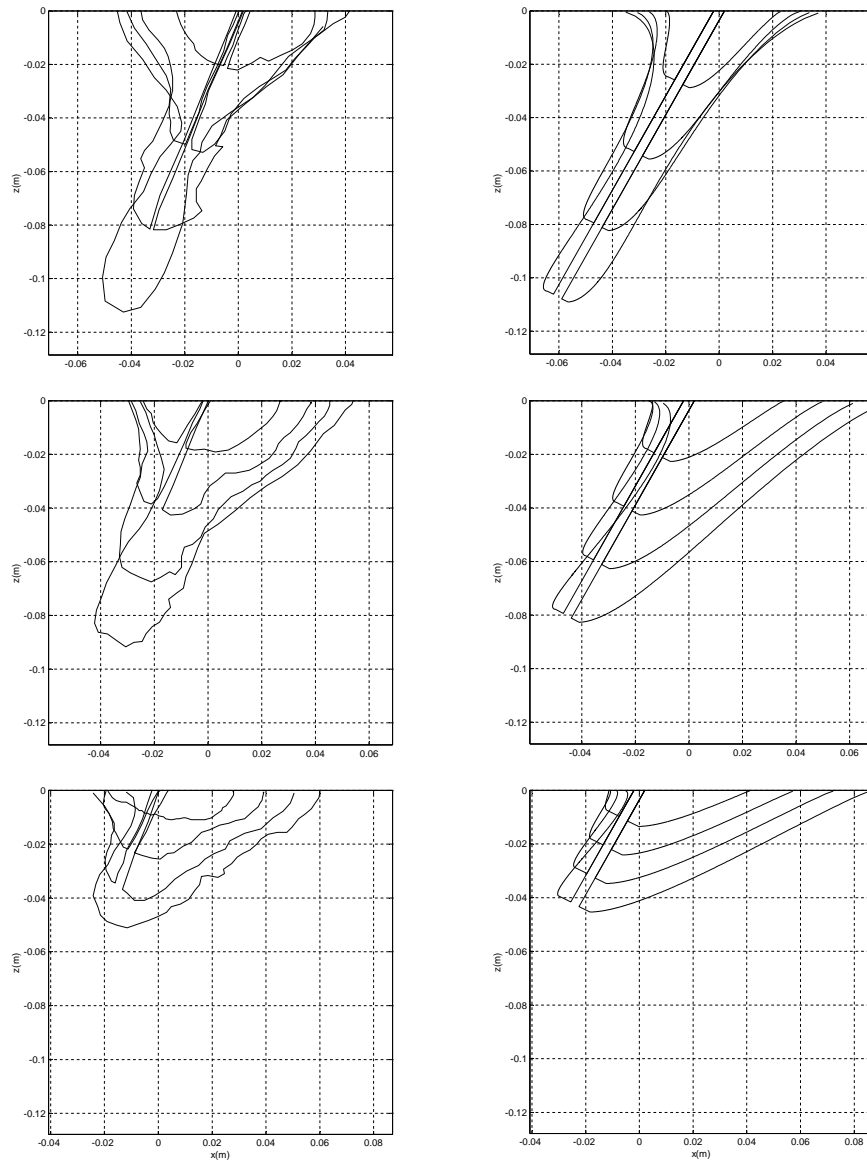


Figure 7.32: Crater temporal evolution for jet condition V ($Fr_j = 11.4, \theta_j = 29.5^\circ$). Measured values on left column for jet translating from right to left at $V_t = 0.00 \text{ m/s}$ (top), $V_t = 0.30 \text{ m/s}$ (middle) and $V_t = 0.60 \text{ m/s}$ (bottom). The contours are given in a reference frame moving with the jet carriage, and correspond to four equally spaced times between the jet impact and t_{po} . The contours on the right column were computed with the theoretical model for the same jet conditions and times as the experimental data.

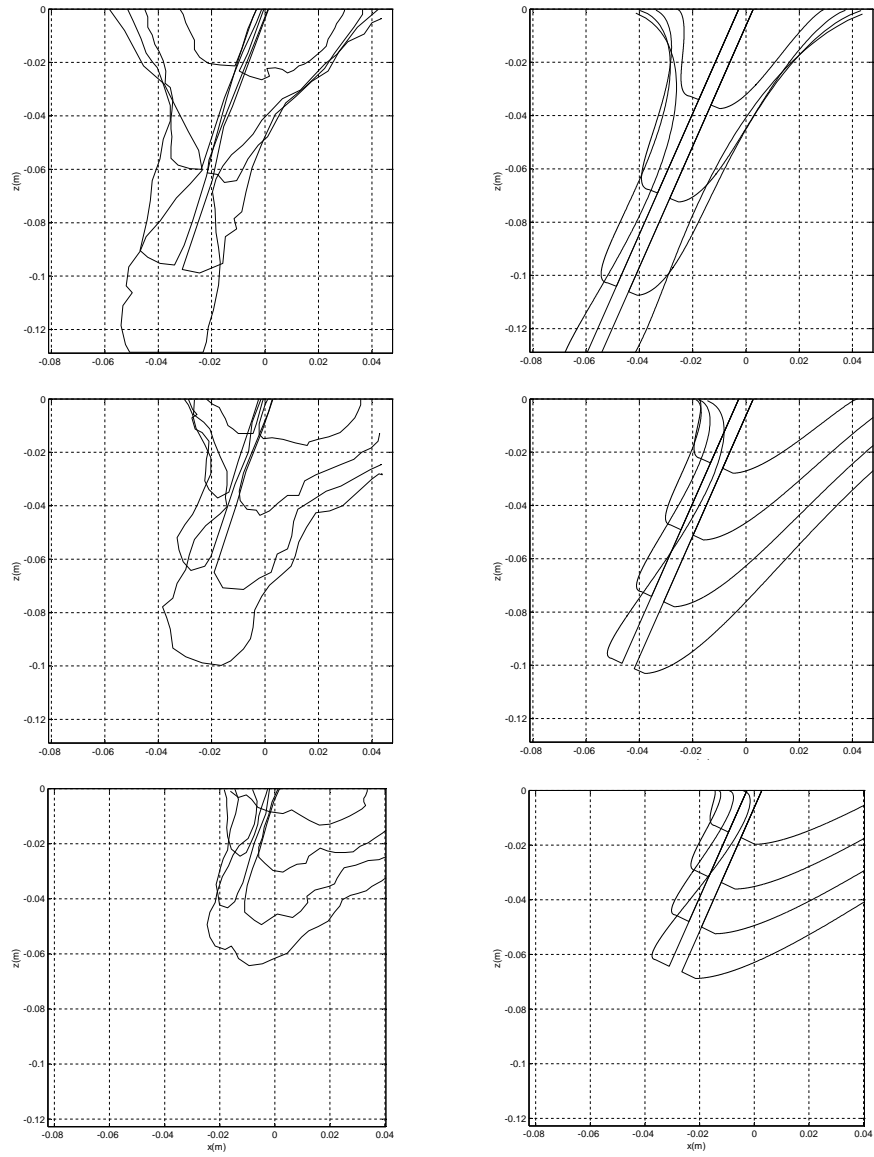


Figure 7.33: Crater temporal evolution for jet condition VI ($Fr_j = 10.0, \theta_j = 23.8^\circ$). Measured values on left column for jet translating from right to left at $V_t = 0.00 \text{ m/s}$ (top), $V_t = 0.30 \text{ m/s}$ (middle) and $V_t = 0.60 \text{ m/s}$ (bottom). The contours are given in a reference frame moving with the jet carriage, and correspond to four equally spaced times between the jet impact and t_{po} . The contours on the right column were computed with the theoretical model for the same jet conditions and times as the experimental data.

As mentioned, the predicted contour shapes qualitatively resemble the measured profiles, which supports the idea that the theoretical model retains the relevant basic physical principles associated to the crater formation for the given parameter space. Some differences, however, can be observed between the model and the digitized profiles that deserve additional discussion. For instance, it can be observed that the model predicts a somewhat uniform collapse along the crater walls leading to a continuous reduction with time of the crater's width. This reduction is noticeable at any distance from the jet tip. Contrarily, in the digitized profiles, it can be seen that the gravity induced deformations are accentuated around the region where the pinch-off takes place, while the area near the jet tip seems to be less affected by gravity than what it is in the model. In order to understand the reason for this difference, some of the model assumptions are repeated in the following. If the effects of the inertia were not important, the crater velocity of deformation (v') should scale like \sqrt{gz} under the assumptions explained in section 7.3. Inertia is important, however, in the regions near the jet tip due to their large radius of curvature as was also explained in section 7.3. One of the assumptions taken to construct the model was that the curvatures were reasonably moderate along most of the length of the crater, therefore allowing the inertial effects near the cavity leading edge to be neglected in a first approximation. As explained in section 7.4, the model considers that the collapse is driven entirely by gravitational effects, with the velocity of deformation of the crater given by $v' = \lambda\sqrt{gz}$, which is applied uniformly all along the length of the craters. It appears that those inertial effects near the jet tip, which are not accounted for by the model, have a noticeable effect, leading to very small deformations in these regions.

Another interesting point is that the distance traveled by the underwater jet tip seems to have the tendency to be slightly larger in the model than in the movies for equal times, although in both cases, the jet tip follows a steady trajectory with approximately the same penetration velocity and penetration angle (see section 7.1). As the jet impacts the receiving pool in the experiments, some energy is transferred from the jet to the pool water resulting in the formation of splashes around the jet impact site. It is possible, therefore, that there exists a very small accommodation time before the underwater jet tip reaches steady conditions. In the model, however, the underwater jet velocity is constant at all times and the described effects are not accounted for. The accommodation time can be defined as the time interval between the jet impact and the instant in which the leading edge of the underwater crater becomes visible. Those times were measured in the movies and the results are summarized in Table 7.1. As it can be seen, the accommodation time has the tendency to grow slightly with the translation velocity for all conditions.

In order to get a more accurate theoretical prediction of the distance traveled by jet leading edge during the accommodation time, the accommodation time measurements can be used. This prediction can be calculated according to the formula,

$$td(t) = V_p \cdot (t - t_a) \quad (7.52)$$

where td is the distance traveled by the jet leading edge, V_p is the theoretical underwater jet tip velocity in an absolute reference frame, t_a is the accommodation time and t is time. Equation 7.52 was used to calculate td for all conditions at three different translation velocities for $t = t_{po}/2$, and the results are shown

Exp. Cond.	$V_t = 0.00m/s$	$V_t = 0.30m/s$	$V_t = 0.60m/s$
I (mean)	6.0	9.0	10.7
II (mean)	8.3	11.0	15.0
III(mean)	9.0	9.0	9.7
IV (mean)	5.5	5.5	5.0
V (mean)	7.3	8.7	9.0
VI (mean)	13.3	14.7	16.3
I (st dev)	1.0	1.7	1.5
II (st dev)	0.6	2.6	1.7
III(st dev)	0.0	1.0	0.6
IV (st dev)	0.7	0.7	0.0
V (st dev)	3.0	1.5	1.0
VI (st dev)	0.6	1.1	0.6

Table 7.1: Accommodation times (ms)

in Figure 7.5 together with the corresponding experimental measurements extracted from the movies. As can be seen from the figure, Equation 7.52 gives a more accurate prediction of the underwater jet leading edge position than what it is obtained if t_a is neglected.

Finally, it should be noted the model does not predict well the slope of the craters at the free surface. In the digitized craters, the slope is more vertical than in the model due to the coupled motion between the craters and the wavy motion of the free surface.

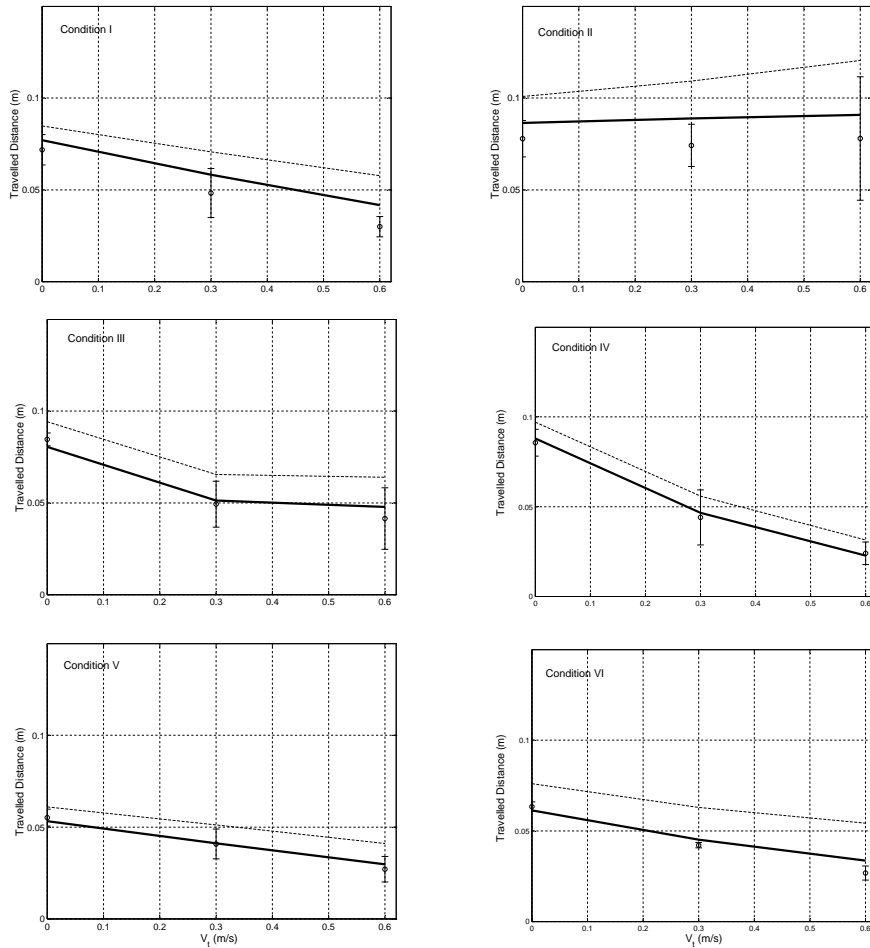


Figure 7.34: Distant traveled by leading edge from impact to $t = t_{po}/2$. Dots are averaged measurements, error bars are 95% confidence intervals, thick line is theoretical prediction using Equation 7.52, and thin line is theoretical prediction neglecting t_a .

7.6 Detachment of the Crater at Small Translation Velocities

After the pinch-off event, the front crater no longer appears as a smooth air-water interface and starts to deform violently as a result of its contact with the jet. The deforming front crater, however, can still be approximately identified in the movies and is observed to continue to approach the back crater driven by the hydrostatic pressure. At this point of development in the underwater crater's history, the flow presents additional complications that present a fundamentally different evolution from what was observed at earlier times. For instance, the pinch-off event leads to the generation of vortices and entrained bubbles in the region confined between the two approaching crater walls. This complicated flow results in particular when the translation velocities are small or zero (typically for $V_t \leq 0.30 \text{ m/s}$), in the formation of an enclosed volume that detaches from the open crater and continues to travel downwards into the pool water. In some cases, the detachment of the large bubble was observed to occur before the crater walls had enough time to meet. This fact suggests that, at least in some cases, the mechanism of detachment may be associated with the complex flow between the two crater walls rather than with the fact that the crater walls touch each other. Figure 7.35 shows a sequence of images where a large bubble forms and detaches from the open crater. The center image corresponds to the moment where the bubble seems to detach ($t = 1.10t_{po}$), although due to the complexity of the flow, the detachment time is hard to identify with accuracy.

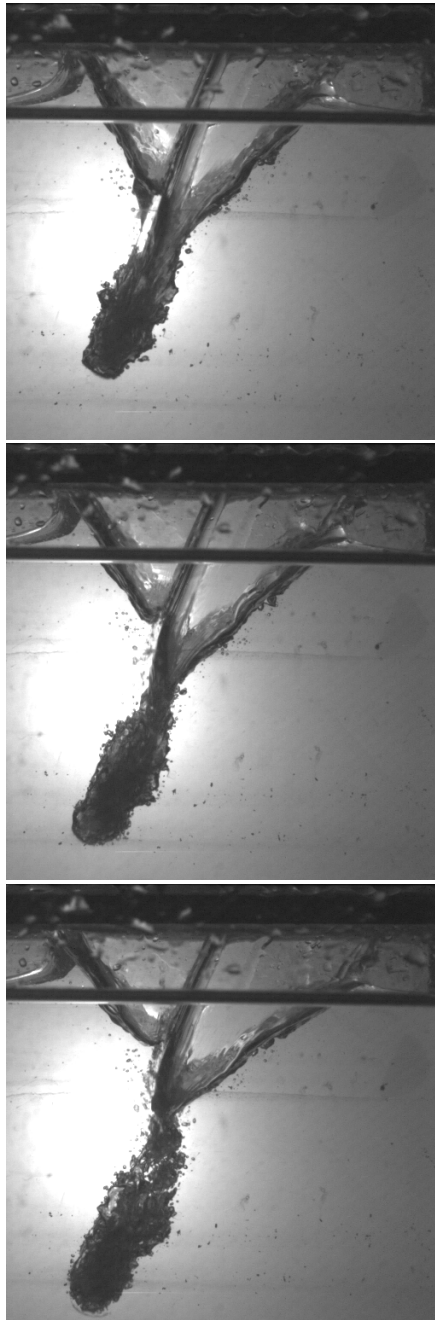


Figure 7.35: Jet condition V, $V_t = 0.15 \text{ m/s}$. Sequence of large bubble formation and detachment. Times are $t = t_{po}$ (top), $t = 1.10t_{po}$ (middle), $t = 1.21t_{po}$.

For jet condition V, the above described bubble was observed to form for jet translation velocities equal to 0.00, 0.15 and 0.30 m/s . For the faster speeds, the back crater wall never reached by the front crater wall and the enclosed volume was not observed to form. For the translation velocities where the bubble does form, the shapes of the craters were digitized as described in section 7.5 at the times where the bubble detaches from the open crater (approximate number of points in each contour equal to 100). The left column of Figure 7.36 shows these contours for the three different translation velocities (0.00, 0.15 and 0.30 m/s).

In order to emphasize the fact that in the cases presented, the detachment does not occur when the two crater walls meet, on the right column of the same figure are shown the contours of the craters when the two crater walls meet as predicted by the theoretical model. It can be seen that this occurrence takes place at much later times. This supports the idea that the mechanism associated to the bubble detachment has to do, in the cases shown, with the complex flow resulting from the jet pinch-off which is not accounted for by the model.

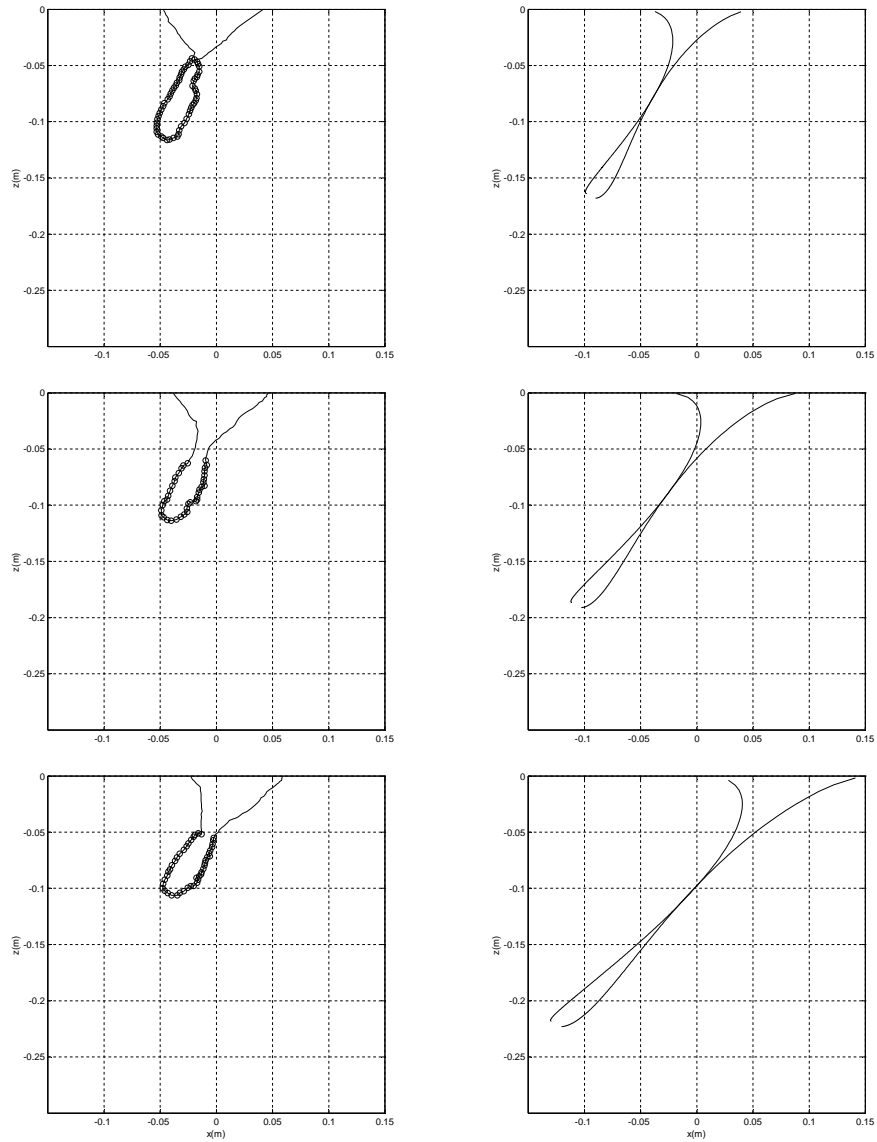


Figure 7.36: Jet condition V. Underwater crater contours from the high-speed movies (left column) at the bubble detachment time. $V_t = 0.00\text{m/s}, t = 1.03t_{po}$ (top), $V_t = 0.15\text{m/s}, t = 1.10t_{po}$ (middle) and $V_t = 0.30\text{m/s}, t = 1.18t_{po}$ (bottom). On the right column, theoretically predicted contours for corresponding values of V_t at the instant when the two crater walls meet. Times are $t = 1.55t_{po}$ (top), $t = 2.01t_{po}$ (middle) and $t = 2.75t_{po}$ (bottom) (t_{po} is the measured pinch of time for each translation speed). The lack of resemblance suggests that the detachment mechanism is associated to effects not considered in the model.

The dots on the experimentally measured contours in Figure 7.36 represent the points that are estimated to form the bubble. For each translation velocity, the area confined by these dots was calculated giving the volume of the entrained bubble (B_v) per unit length into the paper. The digitization of the enclosed volume was performed for the three repetitions of each movie in order to get statistical uncertainty on the measured values. Figure 7.37 shows the averaged values of the entrapped volume (dots) as a function of the translation speed. The error bars are the confidence intervals based on a t-distribution as described in section 5.3 (95% confidence). It is interesting to note that B_v does not seem to be largely affected by variations in the translation speed, at least for the jet conditions measured herein.

This volume was also calculated theoretically by computing the area confined by the theoretical crater between the jet leading edge and the pinch-off depth right at the pinch-off time. The results are the solid line in Figure 7.37. For the stationary jet, experiments and theory are in agreement with a slight under prediction of the theoretical volume probably due to the fact that the gravitational effects near the jet tip were neglected in the model. As V_t is increased, there is a larger deviation between the theory and the experiments which is probably enforced by the complications associated to the bubble detachment in the real experiment. It can be observed in the movies that the detachment mechanism seems to be associated with the presence of a large vortex situated between the two approaching crater walls which grows in strength with V_t .

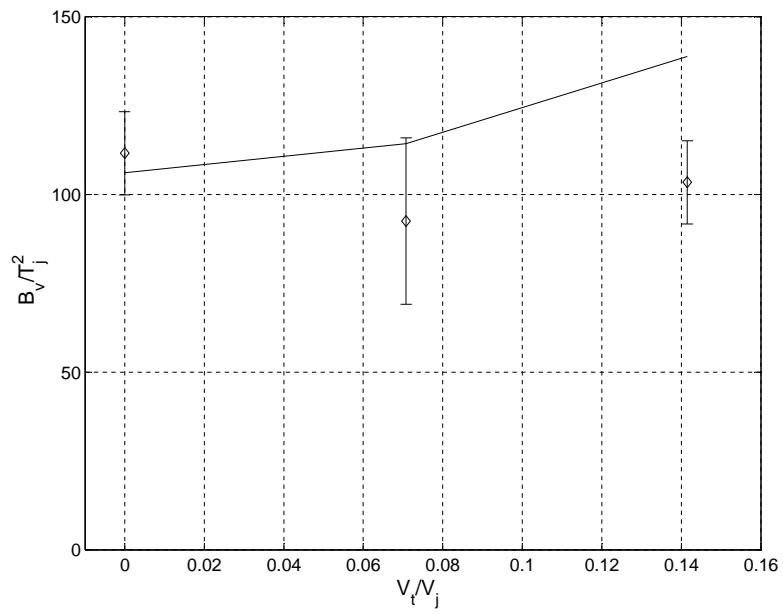


Figure 7.37: Volume per unit length confined by the the large bubble that forms typically at slow jet translation speeds (Jet condition V). Dots are experimental measurements and solid line, theoretical prediction.

Chapter 8

Conclusions for the Impacting Planar Jet

This chapter presents the conclusions relative to the impacting planar jet. In Section 8.1, a summary of the theoretical and experimental results for the crater formation is given and in Section 8.2, a discussion on how the present study can be utilized to help understand the process of aeration of the oceans by breaking waves. Conclusions for the study of incipient entrainment of the translating axisymmetric jet are given in Section 3.5.

8.1 Conclusions on the Physics of the Crater Formation of the Impacting Planar Jet

The inertia of the impacting jet was observed to create two open air craters at either side of the impact site. In the early stages of the crater formation, the open craters spread horizontally and deepen vertically as the jet penetrates further into

the pool water. For the parameter space studied herein, the underwater jet tip moves vertically and horizontally with a steady velocity that can be predicted with quasi-steady potential flow theory.

The dynamics of the different regions of the crater walls are dominated by either inertial or gravitational effects depending on the local radius of curvature (R_o), the local inclination of the crater wall (β_o) and the velocity of the particles parallel to the wall (V_o) given in a reference frame fixed with the jet tip. Inertial effects are dominant in the regions near the jet tip (large values of $Fr_o^2/\cos\beta_o$, where Fr_o is the Froude number based on R_o and V_o). In this region, where gravity plays a secondary role, the craters remain unchanged with time and their shapes can be calculated with quasi-steady potential flow theory. Far from the jet tip, the non-dimensional number $Fr_o^2/\cos\beta_o$ is moderate or small in magnitude and the hydrostatic pressure forces the crater walls to move towards the jet with a deformation velocity that increases with the square root of depth. As time progresses, the crater walls touch the jet at a given depth (pinch-off depth, d_{po}) and at a given time (pinch-off time, t_{po}).

The evolving shapes of the two underwater craters are largely affected by the horizontal translation of the jet, leading to values of (d_{po}) and (t_{po}) which decrease with the jet translation velocity. Simple scaling arguments based on an energy balance applied to the particles situated at the crater walls can be used to estimate the shapes of the underwater crater contours and ultimately, d_{po} and t_{po} .

Lastly, for small jet translation velocities, the underwater craters were observed to detach from the open crater soon after the pinch-off event leading to the formation of a large entrained air bubble. For one of the jet experimental conditions, the volume of air entrapped by this bubble was not observed to vary substantially with the translation speed.

8.2 The Present Study in Relation with the Aeration of the Oceans as a Result of the Simulated Impact of Jets Ejected by Plunging Breakers

Air entrainment and bubble production by waves is a complicated process. Ideally, to quantify the influence of wave breaking on the gas exchange rate, quantitative information on the resulting distribution of bubble sizes and trajectories is needed, in addition to many other factors. This information on bubbles, if it were available, could be introduced into the gas exchange models presented in Chapter 1 and used to help quantify the overall gas exchange rate and its effects, for instance, on climate modeling.

This investigation was not performed to provide quantitative data related to wave breaking, but rather with the aim to understand just some of the aspects of the physics of this complicated process. In particular, experimental and theoretical data were presented on the dynamics of the crater which forms as a result of the impact of a planar jet which is meant to mimic the plunging jet of breaking waves. It is obvious that future studies which attempt to quantify the actual

behaviour of the jets ejected by braking waves using these results, should limit their conclusions to the parameter space of jet inclination angles, thickness as well as impact and horizontal translation velocities typical of the jets ejected by the breakers.

It was found in this study that the dynamics of the resulting crater depends only on three non-dimensional numbers (V_t/V_j , Fr_j and θ_j) and examples of these dependencies are given in Figures 8.1 and 8.2. It was shown that the craters evolve with time and eventually break-up into a cloud of bubbles which are responsible for enhancing the ocean-atmosphere gas exchange rate from what it would be predicted by a simple diffusive process. No quantitative data has been reported on the resulting bubbly plume, however, the crater dynamics that leads to the formation of the bubbles can be used to discuss qualitatively some of the features of the gas exchange. In particular, since the crater break-up takes place shortly after the crater pinches off on the jet, the maximum depth of the crater at the pinch-off time gives an idea (in fact, a conservative estimate) of the maximum depth reached by the plume. The gas exchange is likely to increase for the larger depths since the bubbles have to travel longer distances before they reach the free surface, thus allowing more time for the gas exchange. Since the underwater jet penetration velocity is constant before pinch-off, the plume maximum depth is then in direct relation with the pinch-off time (t_{po}).

As it was shown, t_{po} decreases rapidly with the jet translation velocity and also, as shown in Figure 8.1, increases with the Fr_j , particularly for the slower jet translation velocities. Larger gas exchange rates are expected, therefore, for the slower jets with higher Fr_j values. The jet inclination angle θ_j does not have such a large influence on t_{po} , at least for the parameter space where the model

was validated with experiments (small θ_j). It was also shown, however, that for large values of θ_j (where the model is no longer valid), the free surface effects could have a dramatic impact on the crater dynamics and in particular, played an important role in balancing the effects of the jet translation. That is, for the faster translating jets, a larger gas exchange rate is expected for larger θ_j since the effects of the free surface delay the pinch-off and allow the crater to penetrate deeper into the water. Contrarily, for slow jets with large inclination angles, the free surface effects accelerate the pinch-off process likely leading to a smaller gas exchange rate when compared to the same jet with moderate values of θ_j . The former discussion needs, however, to be compared with experimental data since effects like the bubble production rate, the turbulence levels in the two-phase flow or the total volume of entrained air may have, in addition to the maximum depth of the plume, large implications in the overall gas exchange rate.

Lastly, it was also shown that if V_t is greater than V_j , the jet may bounce off on the water free surface and no crater may be formed whatsoever. For those cases, it is likely that the gas exchange is brought to a minimum.

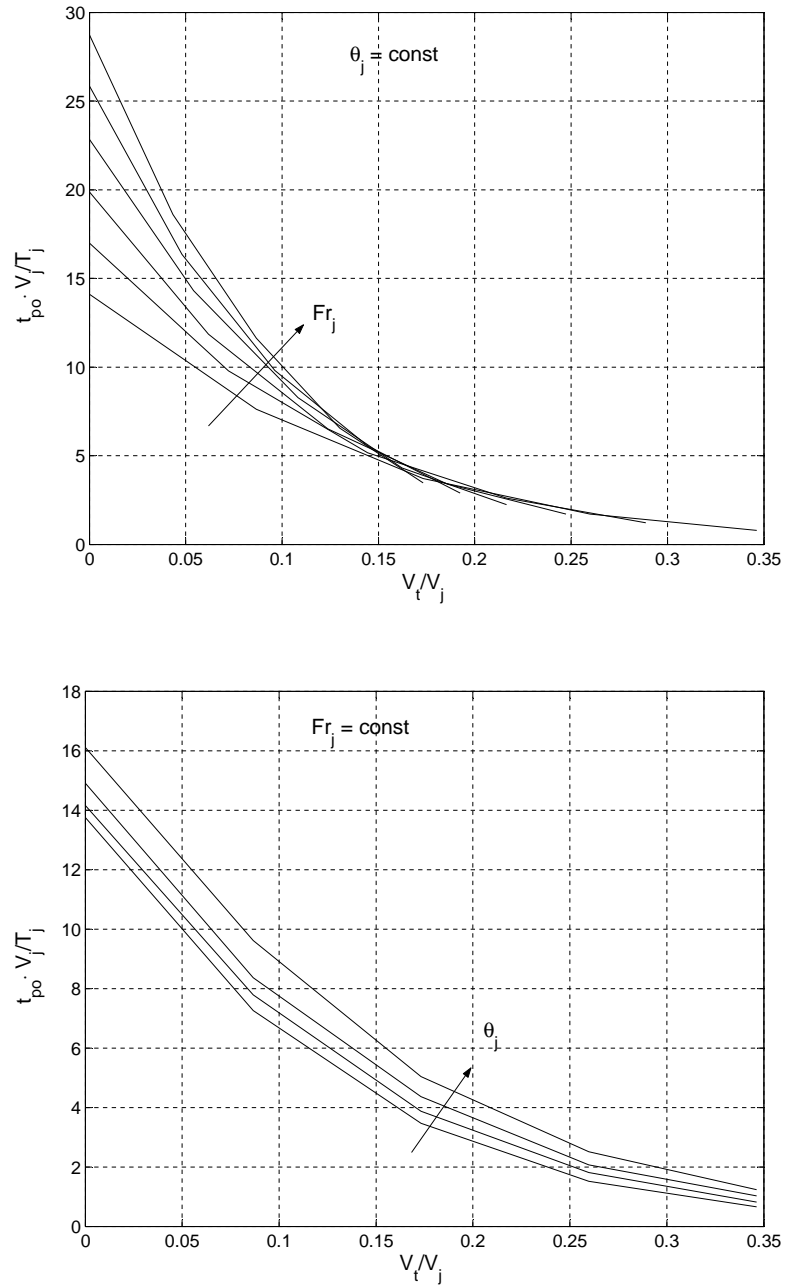


Figure 8.1: Theoretically predicted pinch-off times as a function of V_t for various Fr_j (from 10 to 20) and constant $\theta_j = 20 \text{ deg}$ (top); pinch-off times for various θ_j angles (from 7 to 35 deg) and constant $Fr = 10$ (bottom)

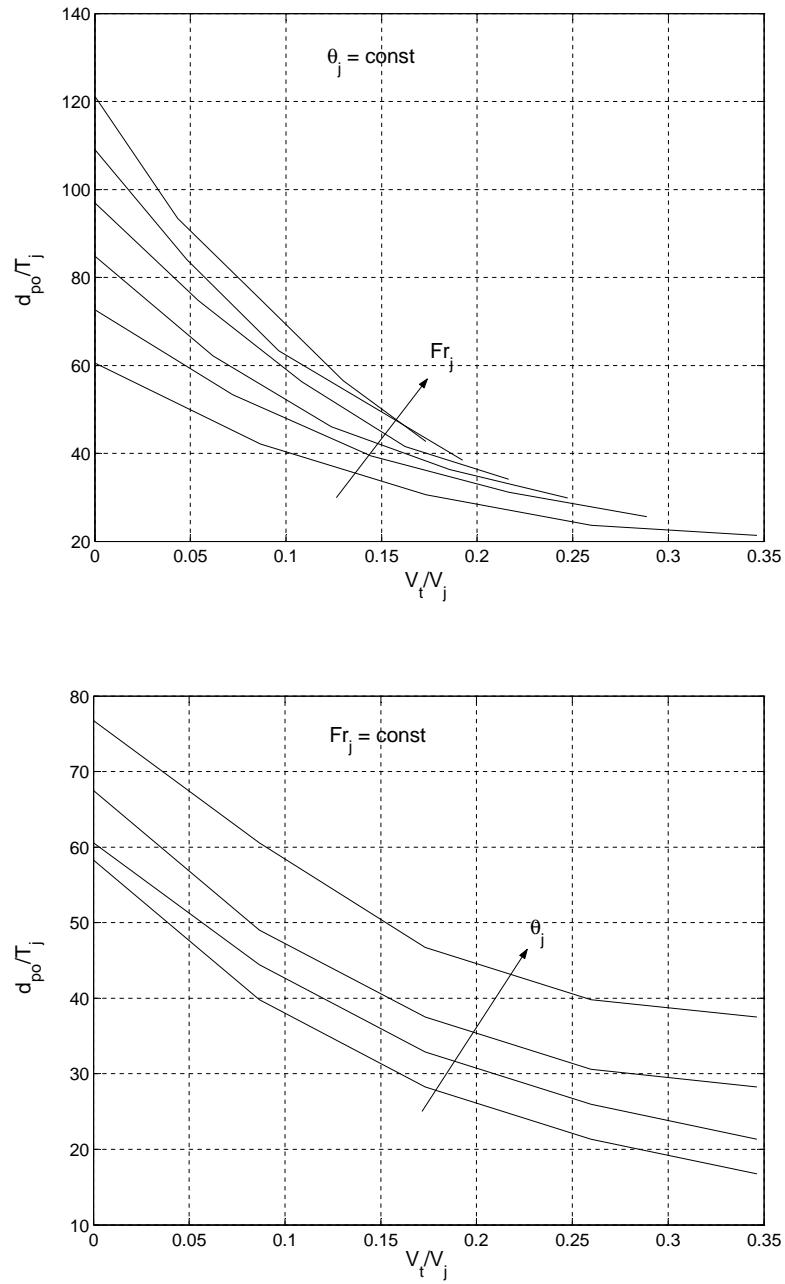


Figure 8.2: Theoretically predicted pinch-off depths as a function of V_t for various Fr_j (from 10 to 20) and constant $\theta_j = 20 \text{ deg}$ (top); pinch-off depths for various θ_j angles (from 7 to 35 deg) and constant $Fr = 10$ (bottom)

BIBLIOGRAPHY

- [1] Kevin E. Trenberth, 1992, *Climate System Modeling.*, *Cambridge University Press.*
- [2] William Asher and Rik Wanninkhof, 1998, Transient tracers and air-sea gas transfer, *J. Geophysical Research*, **103/C8**: 15939-15958.
- [3] Levich, V. G., 1962, *Physicochemical Hydrodynamics*, *Prentice-Hall, Englewood Cliffs, N.J.*
- [4] On gas absorption into a turbulent liquid, *Chem. Eng. Sci.*, 1967 **22**: 1163-1180.
- [5] Tennekes, H., and J.L. Lumley, 1972, *A First Course in Turbulence*, *MIT Press, Cambridge, Mass.*,
- [6] Davies, J.T., 1972, *Turbulence Phenomena*, *Academic, San Diego, Calif.*
- [7] Wanninkhof, R., 1992, Relationship between wind speed and gas exchange over the ocean, *J. Geophysical Research*, **92**: 7373-7382.
- [8] Memerly, L., and L. Merlivat, 1985, Modelling of the gas flux through bubbles at the air-water interface, *Tellus, Ser. B*, **37**: 7373-7382.

- [9] Merlivat, L., L. Memery, and J. Boutin, 1993, Gas exchange at the air-sea interface, Present status: The case of CO₂, Merlivat, L., L. Memery, and J. Boutin, paper presented at The Fourth International Conference on CO₂ in the Oceans, Inst. Natl. des Sci.: de l'Univers. Cent. Natl. de Rech. Sci., Carqueiranne, France.
- [10] Wallace, D.W.R. and C.D. Wirick, 1992, Large air-sea gas fluxes associated with breaking waves, *Nature*, **356**: 694-696.
- [11] D.M. Farmer, C.L. McNeil and B.D. Johnson, 1993, Evidence for the importance of bubbles in increasing air-sea gas flux, *Nature*, **361**: 620-623.
- [12] T.J. Lin and H.G. Donnelly, 1965, Gas bubble entrainment by plunging laminar liquid jets, *A.I.Ch.E. J.* , **12**: 563-571.
- [13] A.K.Bin, 1988, Minimum air entrainment velocity of vertical plunging liquid jets, *Chemical Engineering Science*, **43-2**: 379-389.
- [14] A.K.Bin, 1988, Minimum air entrainment velocity of vertical plunging liquid jets, *Chemical Engineering Science*, **43-2**: 379-389.
- [15] A.T. Sheridan, 1966, Surface entrainment of air by a water jet, *Nature*, **209**: 799-800.
- [16] Y. Zhu, H.N.Oguz and Andrea Prosperetti, 2000, On the mechanism of air entrainment by liquid jets at a free surface, *J. Fluid Mech.*, **404**: 151-177.
- [17] Cumming, I. W., 1975, The impact of falling liquids with liquid surfaces, *Ph.D. Thesis, Loughborough University of Technology, Loughborough*.

- [18] Air retained in a pool by plunging water jet, 1980, *J. Hydraul. Div., Am. Soc. Civ. Eng.*, **106**: 1577.
- [19] Effect of turbulence intensity on the rate of air entrainment by plunging water jets, 1980, *Proc. Inst. Civ. Eng., Struct. Build.*, **69**: 425.
- [20] R. M. Detsch and R.N.Sharma., 1990, The critical angle for gas bubble entrainment by plunging liquid jets, *The Chemical Engineering Journal*, **44**: 157-166.
- [21] E. Van de Sande and J.M. Smith, 1976, Jet break-up and air entrainment by low velocity turbulent water jets, *Chemical Engineering Science*, **31**: 219-224.
- [22] E. Van de Sande and J.M. Smith, 1973, Surface entrainment of air by high velocity water jets, *Chemical Engineering Science*, **28**: 1161-1168.
- [23] E.J. McKeogh and D.A. Ervine, 1981, Air entrainment rate and diffusion pattern of plunging liquid jets, *Chemical Engineering Science*, **36**: 1161-1172.
- [24] K.J. Sene, 1988, Air entrainment by plunging jets, *Chemical Engineering Science*, **43-10**: 2615-2623.
- [25] H.N. Oguz, A. Prosperetti and A.R.Kolaini, 1995, Air entrainment by a falling water mass, *J. Fluid Mech.*, **294**: 181-207.
- [26] Ed. R.E.A. Arndt and A. Prosperetti, Mechanics of air entrainment by a falling liquid, *New York: American Society of Mechanical Engineers*, 13-20.
- [27] A. Prosperetti and H.N. Oguz, 1997, Air entrainment upon liquid impact, *Phil. Trans. R. Soc. Lond. A*, **355**: 491-506.

- [28] J.H. Duncan, H. Qiao, V. Philomin, and A. Wenz, 1999, Gentle spilling breakers: Crest profile evolution, *J. Fluid Mech.*, **379**: 191.
- [29] Control of free-stream turbulence by means of honeycombs: A balance between suppression and generation, 1976 *J. Fluid Eng.*, 342-353.
- [30] Lumley, J. L., and McMahon, J. F., 1976, Reducing water tunnel turbulence by means of a honeycomb, *Journal of Basic Engineering, Trans. ASME, Series D*, **89**: 764.
- [31] J.Scheiman and J.D. Brooks, Comparison of experimental and theoretical turbulence reduction from screens, honeycomb, and honeycomb-screen combinations, 1976 *J. Aircraft*, **18**: 638.
- [32] Rae Pope, Low-speed wind tunnel testing, *Wiley-Interscience 2nd edition*.
- [33] W.S. Gosset, 1908, The probable error of a mean, *Biometrika*, **6(1)**: 1:25.
- [34] M. Abramowitz and I. A. Stegun, eds, 1972, Handbook of Mathematical Functions with Formulas, Graphs, and Mathematical Tables, *New York: Dover*, section 26.7.
- [35] Ronald L. Panton, 1996, Incompressible flow - 2nd Ed., *A Wiley-Interscience publication*.
- [36] Milne-Thomson, 1891, Theoretical hydrodynamics - 5th Ed., *Dover Publications*.
- [37] Sir Horace Lamb, 1945, Hydrodynamics - 6th Ed., *Dover Publications*.